UNITED TECHNOLOGIES RESEARCH CENTER
East Hartford, Connecticut 06108

R90-927764

Tunable Blue–Green LIDAR Transmitter Demonstration: Injection Laser Technology

Sponsored by the Office of Naval Research
Contact N00014-87-C-0371

UNITED
TECHNOLOGIES
RESEARCH
CENTER
East Hartford, Connecticut 06108

R90-927764

Tunable Blue-Green LIDAR Transmitter Demonstration: Injection Laser Technology

Final Report

August 30, 1990

Prepared by:

W. L. Nighan
R. A. Rubino
A. J. Cantor
W. H. Glenn

Sponsored by the Office of Naval Research
Contact N00014-87-C-0371

Unclassified

SECURITY CLASSIFICATION OF THIS PAGE

REPORT DOCUMENTATION PAGE

Form Approved OMB No. 0704-0188

1a. REPORT SECURITY CLASSIFICATION: Unclassfied	1b. RESTRICTIVE MARKINGS
2a. SECURITY CLASSIFICATION AUTHORITY	3. DISTRIBUTION/AVAILABILITY OF REPORT: Approved for public release; distribution unlimited.
2b. DECLASSIFICATION/DOWNGRADING SCHEDULE	
4. PERFORMING ORGANIZATION REPORT NUMBER(S)	5. MONITORING ORGANIZATION REPORT NUMBER(S)
6a. NAME OF PERFORMING ORGANIZATION: United Technologies Research Center; 6b. OFFICE SYMBOL (If applicable)	7a. NAME OF MONITORING ORGANIZATION: Office of Naval Research
6c. ADDRESS (City, State, and ZIP Code): 400 Main Street, East Hartford, Connecticut 06108	7b. ADDRESS (City, State, and ZIP Code): Physics Division (Code 1112LO), 800 North Quincy St, Arlington, VA 22217-5000
8a. NAME OF FUNDING/SPONSORING ORGANIZATION; 8b. OFFICE SYMBOL (If applicable)	9. PROCUREMENT INSTRUMENT IDENTIFICATION NUMBER: N000014-87-C-0371
8c. ADDRESS (City, State, and ZIP Code)	10. SOURCE OF FUNDING NUMBERS: PROGRAM ELEMENT NO. / PROJECT NO. / TASK NO. / WORK UNIT ACCESSION NO

11. TITLE (Include Security Classification)
Tunable Blue-Green LiDAR Transmitter Demonstration: Injection Laser Technology

12. PERSONAL AUTHOR(S) W. L. Nighan, R. A. Rubino, A. J. Cantor, W. H. Glenn

13a. TYPE OF REPORT	13b. TIME COVERED	14. DATE OF REPORT (Year, Month, Day)	15. PAGE COUNT
Final Report	FROM 5/15/87 TO 8/30/90	90/8/30	165

16. SUPPLEMENTARY NOTATION
The work reported under this contract is complementary to research carried out under a companion program at Rice University supported under Contract N00014-86-K-0698

17. COSATI CODES		
FIELD	GROUP	SUB-GROUP

18. SUBJECT TERMS (Continue on reverse if necessary and identify by block number)
XeF(C-A) laser, scalable blue-green laser, wavelength-agile laser, injecton controlled XeF(C-A) laser, injection laser technology, wavelength-agile dye laser, optical parametric oscillator

19. ABSTRACT (Continue on reverse if necessary and identify by block number)

Rice University and United Technologies Research Center have collaborated on a scaling demonstration of the tunable, blue-green XeF(C-A) excimer laser focusing on the general requirements of a sensor for optical discrimination applications. Under separate contract Rice developed a scaled, repetitively pulsed XeF(C-A) laser amplifier, while under the present contract UTRC developed a wavelength-agile dye laser as a source of injection control for the Rice amplifier. In late 1989 the UTRC injection laser was successfully integrated with the Rice XeF(C-A) amplifier, resulting in wavelength-agile XeF(C-A) laser operation at the 1 J/pulse level, combined with an intrinsic efficiency > 1% and a pulse repetition rate of 1 Hz. Random sequence wavelength agility on a pulse-to-pulse basis was demonstrated over a 20 nm band, and an over-all efficient tuning range approach 50 nm was demonstrated. This final report covers the UTRC portion of the program, wavelength-agile injection laser technology in particular.

20. DISTRIBUTION/AVAILABILITY OF ABSTRACT	21. ABSTRACT SECURITY CLASSIFICATION
☐ UNCLASSIFIED/UNLIMITED ☒ SAME AS RPT. ☐ DTIC USERS	UNCLASSIFIED
22a. NAME OF RESPONSIBLE INDIVIDUAL: DR. F. W. QUELLE	22b. TELEPHONE (Include Area Code): 617-451-3171; 22c. OFFICE SYMBOL: 1112LO

DD Form 1473, JUN 86 Previous editions are obsolete. SECURITY CLASSIFICATION OF THIS PAGE

Unclassified

FOREWORD

Rice University and United Technologies Research Center have collaborated on a scaling demonstration of the tunable, blue–green XeF(C–A) excimer laser focusing on the general requirements of a sensor for optical discrimination applications. Under separate contract Rice developed a scaled, repetitively pulsed XeF(C–A) laser amplifier, while under the present contract UTRC developed a wavelength–agile dye laser as a source of injection control for the Rice amplifier. In late 1989 the UTRC injection laser was successfully integrated with the Rice XeF(C–A) amplifier, resulting in wavelength–agile XeF(C–A) laser operation at the 1 J/pulse level, combined with an intrinsic efficiency > 1% and a pulse repetition rate of 1 Hz. Random sequence wavelength agility on a pulse–to–pulse basis was demonstrated over a 20 nm band, and an over–all efficient tuning range approach 50 nm was demonstrated. This final report covers the UTRC portion of the program, wavelength–agile injection laser technology in particular.

R90-927764

Tunable Blue–Green LIDAR Transmitter Demonstration: Injection Laser Technology

TABLE OF CONTENTS

TABLE OF CONTENTS
(continued)

LIST OF FIGURES

LIST OF FIGURES (continued)

LIST OF FIGURES (continued)

LIST OF TABLES

R90-927764

Tunable Blue-Green LIDAR Transmitter Demonstration: Injection Laser Technology

1.0 BACKGROUND AND INTRODUCTION

1.1 Historical Overview: The XeF(C-A) Excimer Laser

The XeF excimer laser operating on the C-A transition in the blue-green spectral region is a cousin of the well known UV rare gas halide lasers such as KrF (248 nm), XeCl (308 nm) and XeF (351 nm). In addition to the fact that the wavelength of the XeF(C-A) laser is in the visible region, this laser is *continuously tunable* throughout the blue-green region, a unique feature having importance for many applications.

Although laser oscillation on the C-A transition was demonstrated in the late 1970s shortly after the UV rare gas halide lasers were discovered, the operating efficiency of the XeF(C-A) laser was much too low for practical applications. This problem was the result of very low gain due to the combination of a simulated emission cross section more than an order-of-magnitude smaller than that of the UV rare gas halide lasers, and a high level of transient absorption. Many thought that these characteristics represented fundamental limitations to successful exploitation of the special properties of the XeF(C-A) laser.

1.2 Rice University - United Technologies Collaboration

In the early 1980s Rice University and United Technologies Research Center joined forces in an effort to improve the performance of the 'C-A' laser. With support from the **Office of Naval Research**, this university-industry team identified the primary transient species in the laser gas mixture that were absorbing radiation at the laser wavelength. Based on the insight gained from this work, the team devised and patented special gas mixtures containing up to five constituents. Use of these mixtures significantly reduced the transient absorption resulting in a large increase in the net gain on the XeF(C-A) laser transition.

The laser performance improvement resulting from the higher gain was found to be dramatic. With excitation provided by a high current density electron beam having a temporal duration of 10 ns, XeF(C-A) laser energy density and intrinsic efficiency in excess of 1 Joule/liter and 1% were demonstrated, values that for the first time were comparable to those typical of UV rare gas halide lasers (Ref. 1). Subsequently, efficient injection-controlled tuning was demonstrated, resulting in laser wavelengths with a spectral width less than 0.01 nm tuned over a 30 nm range centered at 485 nm (Ref. 2). These early results and developments are summarized in Fig. 1.

1.3 SDI/DoD Applications

Because of its *broadband tunabilty* and *scaling potential*, as revealed by the Rice-UTRC results, the XeF(C-A) laser was identified immediately as a candidate for possible development as a *beam-agile* sensor for optical discrimination. The basic concept envisioned was based on combining the tunable 'C-A' laser with a grating, with beam scanning in one direction provided by mechanical means and in the other by wavelength tuning, i.e., one-dimensional wavelength-agility. The ~50 nm continuous tuning range of the 'C-A' laser, combined with its very large number of resolvable wavelengths, are consistent with complete coverage of the 10-20 degree field-of-view required for an optical discrimination sensor system.

Additionally, an unconventional approach to optical discrimination, multiple aperture speckle imaging appears to have promise for optical discrimination applications (Ref. 3). This technique requires processing of decorrelated speckle patterns from an illuminated object in space. Obtaining decorrelated speckle patterns from non-rotating targets requires coherent illumination at different wavelengths, i.e., wavelength-agile illumination, a requirement consistent with 'C-A' laser capabilities.

Additional features of the XeF(C-A) laser and their relationship to various SDI/DoD applications are summarized in Fig. 2.

1.4 XeF(C-A) Laser Scaling Demonstration

Although the initial Rice-UTRC XeF(C-A) laser results were exceptionally encouraging, they were demonstrated using a *small-scale, single-shot laboratory experiment*. In order to establish the real

Principal results - 1982-1987

- **Identification of primary transient absorbers**
- **Devised and *patented* unique five component gas mixture to control absorption**
- **Laser energy density increased by ~ three orders-of-magnitude to ~ 1.5 J/liter**
- **Intrinsic efficiency increased to ~ 1.5%**
- ***Performance comparable to UV rare gas-halide B-X lasers***
- **Demonstrated *efficient, continuous tuning* between 465 nm and 515 nm**
- **Motivated research programs worldwide**

Figure 1. Principal results of the Rice-UTRC collaboration for the period 1982-1987.

90-8-38-1

XeF(C-A) LASER

Continuously tunable throughout the 450 - 530 nm spectral region

Feature	Benefit
• **Broad band tunability, 450-530nm**	• **Beam agility,** *speckle averaging*
• **Precise wavelength selection**	• **Object signature analysis, access to many atomic resonance filters**
• **Intrinsic efficiency ~1.5%, energy density ~1.5 J/liter**	• **Meets performance requirements for most DoD applications**
• **Blue-green wavelength**	• **Good balance among conflicting demands on energy, optics, detectors,** *atmospheric transmission*
• **Gaseous medium**	• *Scaling is relatively straightforward*
• **Rare gas halide excimer**	• **Well established 15 year technology base**

Figure 2. Features and benefits of the XeF (C - A) laser.

90-8-38-2

potential of the 'C-A' laser for applications requiring high pulse energy/power, it was essential that the initial small scale results be verified using a scaled device. Accordingly, in 1987 UTRC and Rice joined forces in the present SDIO/IST-supported program directed toward a scaling demonstration of the XeF(C-A) laser. The general features of the initial small-scale laser and the design targets for the scaled 'C-A' laser system are compared in Fig. 3

Of particular significance is the fact that meaningful demonstration of wavelength agility on a pulse-to-pulse basis requires a repetitively pulsed scaled laser system. Under separate contract Rice University undertook development of a scaled, repetitively pulsed XeF(C-A) laser amplifier, while under the present contract UTRC developed a wavelength-agile dye laser as an injection source of wavelength control for the Rice amplifier. The ultimate objective of the overall program was integration of the UTRC injection control system with the Rice amplifier in order to demonstrate scaled, wavelength-agile performance of an XeF(C-A) laser system.

This report presents the results, findings and conclusions of the UTRC injection laser technology program, along with a summary of the performance of the integrated Rice-UTRC systems.

It is worth mentioning that the Rice-UTRC XeF(C-A) laser scaling experiment represents the most ambitious *initial* scaling demonstration of an excimer laser ever undertaken, in that **energy scaling to the Joule-per-pulse level, 1% efficiency, broadband tuning and repetitive pulse operation were to be demonstrated,** *all in one step* (Fig. 3).

All the initial program objectives were met or exceeded.

RICE / UTRC XeF (C - A) LASER SCALING SUMMARY

	Pulserad		*Pocobeam*
Size:			
• **Length**	**10 cm**	→	**50 cm**
• **Volume**	**0.02 liters**	→	**0.5 liters**
Optics			
• **Unstable resonator**			
- **Magnification**	**1.1**	→	**1.7**
- **Configuration**	**internal**	→	**internal and** *external*
PRF	**single shot**	→	**1 Hz**
Energy	**20 mJ**	→	**~1 J**
Tuning			
• **Bandwidth**	**40 nm**	→	**70 nm**
• **Rate / strategy**	**one λ at a time**	→	**1 Hz,** *random sequence wavelength agility*

Figure 3. Comparison of the general features/specifications of the Rice "small-scale" XeF (C - A) laser (pulse rad) with the design objectives for the scaled (C - A) laser (pocobeam).

90-8-38-3

2.0 WAVELENGTH AGILE DYE LASER DEVELOPMENT

2.1 Background

In 1987 UTRC and Rice University joined forces in an SDIO/IST - supported program directed toward a scaling demonstration of the XeF(C-A) excimer laser (Refs. 4, 5). Because of its broadband tunability and scaling potential, at the time the 'C-A' laser was considered a prime candidate for development of a beam-agile sensor for optical discrimination. The basic concept envisioned was based on combining the tunable C-A laser with a grating, with beam scanning in one direction provided by mechanical means and in the other by wavelength variation. Reflecting the $> 10^3$ km range of the application and a required 10-20° field of view, ensuring complete coverage at the target scene results in a requirement for a very large number of resolvable wavelengths, e.g., 10^5-10^6. For that reason, defining XeF(C-A) laser wavelength control concepts consistent with the requirement for a large number of resolvable wavelengths and rapid tuning was the primary focus of the *initial* UTRC research, resulting in the laser system described in this section.

2.1.1 Injection Control

The only effective means for controlling the wavelength of a scaled XeF(C-A) laser is injection control (Refs. 6, 7). **The UTRC responsibility in the Rice-UTRC program was development of a wavelength-agile injection laser source to drive the scaled XeF(C-A) laser amplifier under development at Rice.** The basic requirements for the injection laser are that it be rapidly tunable over the 460-520 nm band, that it provide a large number of resolvable frequencies (i.e. have a narrow bandwidth), and that its pulse length and energy be appropriate for use as an injection source for the 'C-A' excimer laser. The 460-520 nm band corresponds to a frequency bandwidth of 75 THz (7.5×10^{13} Hz). For a ~ 20 ns pulse duration, typical of the UTRC-Rice 'C-A' laser, the transform-limited bandwidth is about 50 MHz. This allows the possibility of as many as 1.5×10^6 resolvable frequency elements. The injection laser system developed by UTRC and described herein has far fewer resolvable elements, but can be viewed as a first step toward an extremely high resolution frequency agile laser system.

2.1.2 Laser Sources

Several possible sources for injection control of the Rice 'C-A' amplifier were considered originally, including, tunable solid state lasers, frequency mixing schemes, optical parametric oscillators, and organic dye lasers. Tunable solid state lasers such as Ti: sapphire operate in the infrared and would have to be frequency doubled to produce radiation in the desired blue-green band. This would require tuning of both the fundamental source and the doubling system. The same is true of frequency mixing schemes. *Optical parametric oscillators* (OPOs) are attractive because of their extremely wide potential tuning range (UV to IR). At the time when the UTRC-Rice program began, most work reported on optical parametric oscillators made use of lithium niobate. This crystal is suitable for use in the infrared. When exposed to radiation in the blue-green region or at shorter wavelengths, however, it is subject to optical damage even at very modest power levels. For this reason, it was not considered a viable candidate. Since then a new nonlinear crystal has become available, beta barium borate (BBO). Optical parametric oscillators using this crystal have been operated quite successfully by several research groups. Further development would be required to achieve narrow linewidth oscillation in an OPO; however, it may become an attractive source for future systems, as described in Section 5.0 of this report. **Nonetheless, it was concluded that the wavelength agility required for the initial phase of research could best be met using an organic dye laser,** although a single dye can only access a portion of the 'C-A' laser tuning range, i.e., ~ 50%.

2.1.3 Basic Design Strategy

Commercially available excimer pumped dye lasers, such as the Lambda-Physik Model FL3002 have spectral properties, pulse duration and energy output that are well suited for 'C-A' the injection laser application, and have in fact been used in previous experiments, albeit on a single shot basis (Refs. 2, 7, 8). This dye laser can be operated at rates up to several hundred Hz depending on the excimer pump source used. However, the wavelength *cannot* be tuned on a pulse-to pulse basis. The Lambda Physik design is based on wavelength tuning by manual means. **Thus, for the purposes of the XeF(C-A) laser experiments at Rice, it was concluded that the most expedient approach was to retain as much as possible of the basic Lambda Physik dye laser design, and to redesign the oscillator section to allow rapid tuning.** A number of possible tuning schemes were considered for the oscillator,

including, acousto-optic tunable filters, electrooptical filters, etalons and gratings. A grating is the most attractive because it provides, by far, the largest number of resolvable wavelengths. However, the Littrow arrangement used in the Lambda Physik laser is not suitable for rapid tuning since it would require tilting the large and relatively heavy grating at high rates. If a mirror were used for the scanning, it would have to be as large as the grating and would be equally difficult to adjust rapidly.

An arrangement that has been used successfully with dye lasers is the *grazing* incidence configuration illustrated in Fig. 4. In this scheme the input beam impinges on the grating at *grazing* incidence, and the first-order diffracted beam emerges nearly normal to the grating. A mirror is placed to reflect the output beam back on itself. The beam diffracts again and returns counterpropagating with respect to the input beam. Tuning is accomplished by tilting the mirror. This arrangement has several important advantages:

1. Because of the grazing incidence it allows a large area on the grating to be illuminated by a relatively small diameter beam. This eliminates the need for beam expanding optics.

2. The beam is diffracted twice by the grating, which provides increased dispersion.

3. The input and output beams from the grating are separated. A reducing telescope may be placed between the grating and the mirror to reduce the aperture required of the scanner.

For these reasons, the UTRC XeF(C-A) injection laser design is based on the *grazing incidence configuration*.

2.2 UTRC Injection Laser Design and Properties

A major driver throughout our approach to the design of the injection laser system for the Rice 'C-A' amplifier has been the underlying philosophy that the wavelength-agile dye laser should be simple, reliable and robust, requiring minimal user intervention. Inasmuch as this goal is achieved, complete computer control becomes viable, and a variety of system diagnostics can be utilized with

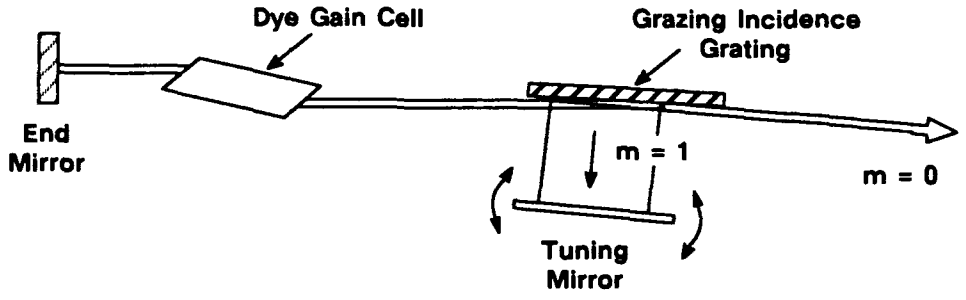

Figure 4. Schematic illustration of the grazing incidence grating configuration. The m=0 and m=1 orders of reflection are indicated.

89-10-16-19

diagnostic information presented graphically in real time and/or permanently logged in tabular form for later retrieval.

Toward this end, UTRC has developed an excimer pumped, wavelength-agile dye laser suitable for use as the injection source for the electron beam pumped XeF(C-A) laser amplifier developed by Rice University (Refs. 8, 9). The specifications and features of this source as it is presently configured are summarized in Table I. **Though other systems are available having one or more similar characteristics, we believe the UTRC injection source to be the *only* system capable of meeting all the indicated specifications, particularly, continuous, *pulse-to-pulse wavelength tunability* at relatively high PRF.** A schematic illustration of the overall laser design is presented in Fig. 5 and the corresponding photographs of the system are shown in Figs. 6 and 7.

TABLE I
PROPERTIES OF UTRC INJECTION LASER

Excitation configuration	UV excimer-pumped dye laser system
Excimer energy, pulse duration	100 mJ @308 nm, 15 ns FWHM
Bandwidth, wavelength range	30 nm, 465-495 nm (Courmarin 102)
Max pulse energy and duration	6 mJ @480 nm, 15 ns FWHM
Tuning method	Holographic grating (2400 lines/mm) combined with a galvo-driven mirror
Operating mode	*Continuous, pulse-to-pulse tunability throughout the band; any arbitrary pre-selected wavelength sequence*
Control strategy	Computer controlled galvo tuning
Maximum tuning speed	70 Hz limited by excimer pump
Wavelength accuracy	± 0.01 nm
Spectral width, *coherence length*	0.01 nm, 2.5 cm
Operational/design features	Menu driven IBM PC controlled; EMI shielded; industrial hardened electronics

2.2.1 Oscillator Design and Characteristics

As discussed briefly in Section 2.1, a laser oscillator utilizing a grazing incidence grating as the wavelength selective element results in the greatest number of resolvable wavelength elements, and

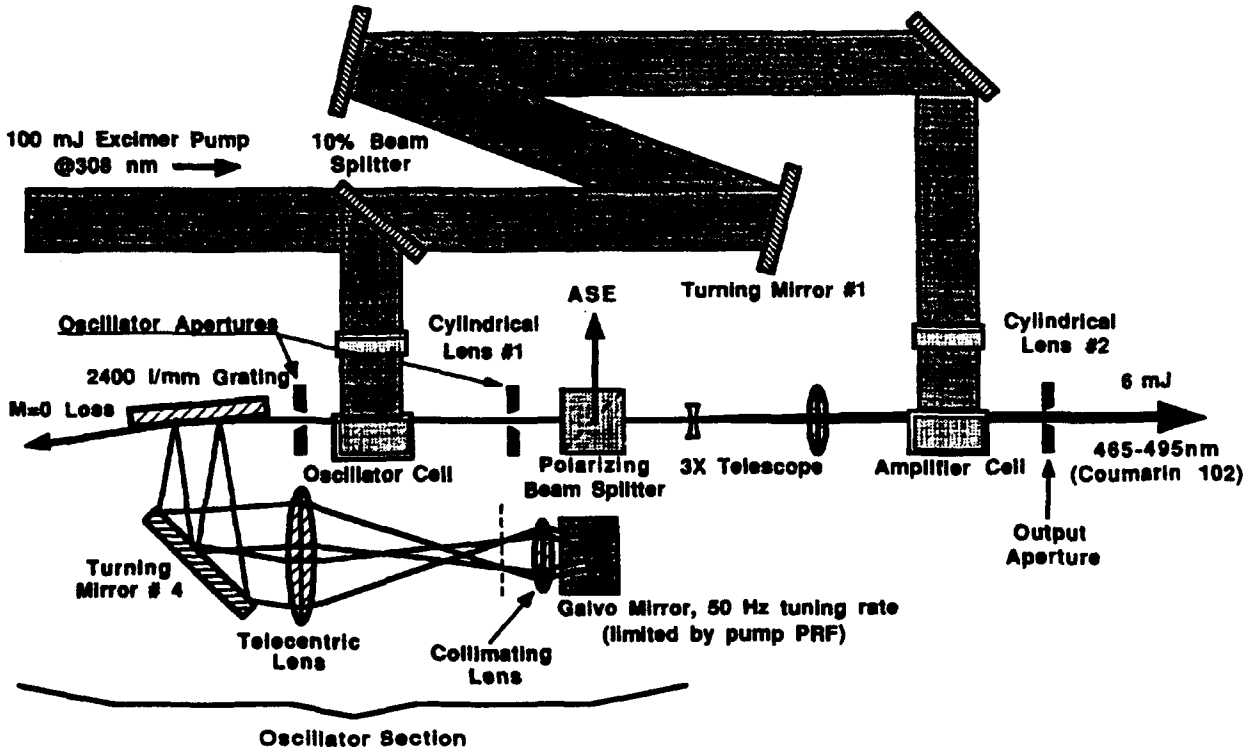

Figure 5. Schematic illustration of the existing UTRC wavelength-agile dye laser system. The oscillator portion is indicated.

89-10-16-1

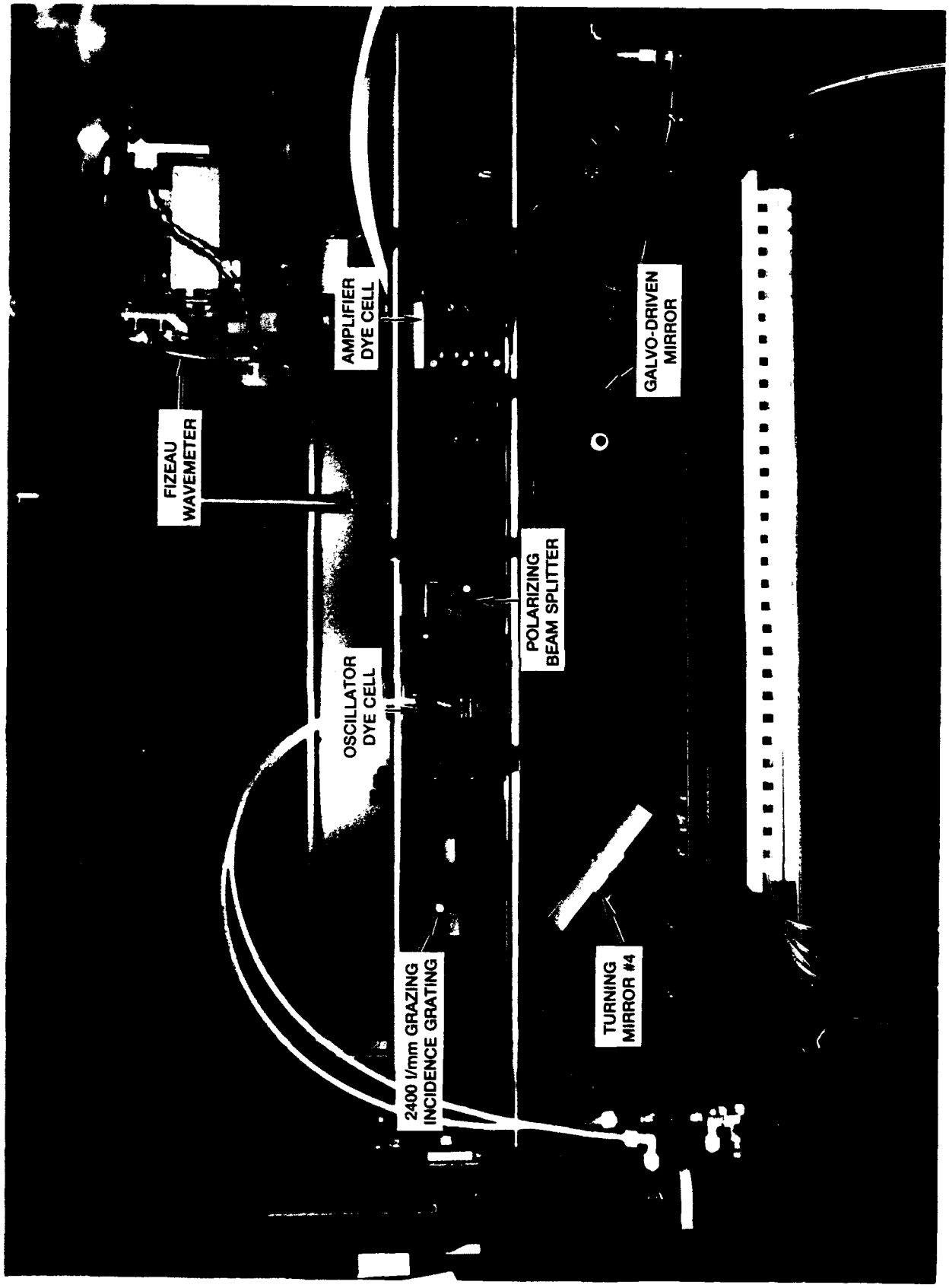

C-89-299-C-14

89-10-16-22

Figure 6. Photograph of the UTRC wavelength agile dye laser. The labeled items can be compared directly with the schematic of Fig. 5.

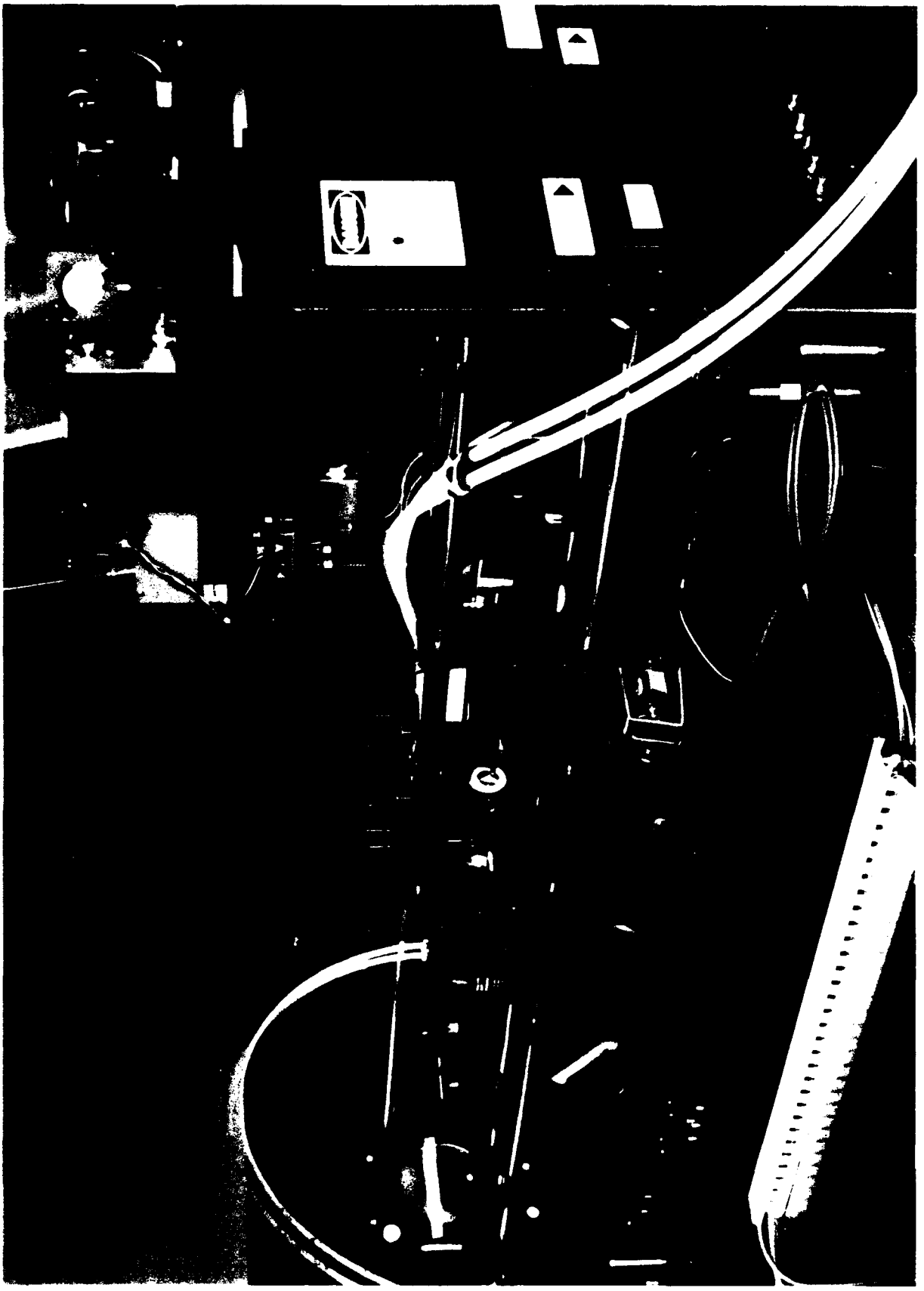

C89-299-A18

89-10-16-23

Figure 7. Photograph of the UTRC wavelength agile dye laser.

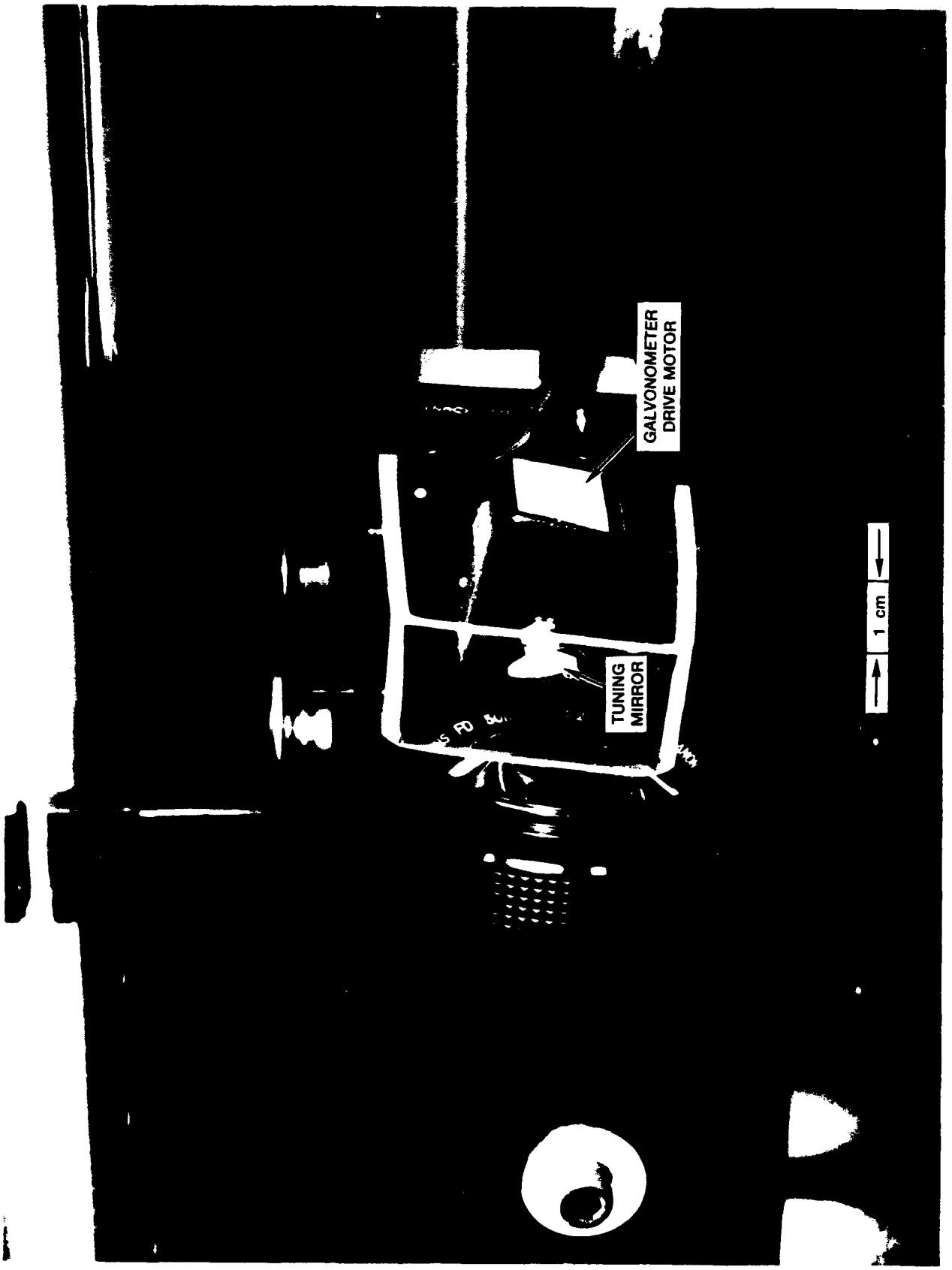

C-89-299-B-10

89-10-16-20

Figure 8. Photograph of the tuning mirror and galvonometer drive motor.

represents the minimum risk of implementation, as compared to other schemes incorporating tunable etalons, for example. As shown in Fig. 5, the oscillator cavity is comprised of a transversely pumped dye cuvette, a polarizing beam splitter which also serves as a low reflectance output coupler, a grazing incidence grating, and a galvanometer driven end mirror to provide tuning. A photograph of the galvanometer and tuning mirror is presented in Fig. 8. High speed wavelength agility is made possible through the incorporation of a telescope, whereby the tuning feedback mirror, which is typically at least as large as the illuminated portion of the grating, can be reduced in size by the magnification of the telescope thereby permitting operation at high PRF values.

For an oscillator of this design, comprising a 2400 line/mm grating 50 mm long having an angle of incidence of 87°, the theoretical wavelength resolution limit is ~ 0.0004 nm. In practice, this best-case limit is actually degraded significantly by the acceptance angle of the aperture/pumped region of the dye cell, which increases the spectral width of the oscillator output by about an order-of-magnitude to a value on the order of 0.004 nm. However, analysis of the interference fringes (shown in Fig. 9), produced by a Fabry-Perot (FP) monitoring etalon of 0.05 nm free spectra range (FSR), indicates that the spectral width of the oscillator output is actually ~ 0.01 nm, corresponding to a coherence length of ~ 2.5 cm. This additional increase in spectral width is caused by the blur circle of the reducing telescope required for high speed tuning.

It should be noted that the fine line structure of the fringes shown in Fig. 9 is caused by spatial hole burning within the gain medium, and does not reflect the presence of cavity modes. The cavity length of the UTRC oscillator is approximately 75 cm; therefore the cavity mode spacing of 200 MHz greatly exceeds the resolution capability of the monitoring etalon. The fact that the origin of this band structure is not due to cavity modes is further born out by the temporal profile of the dye laser.

The temporal pulse of the dye laser and the UV excimer pump are shown for comparison in Fig. 10. The smooth contour of the dye laser temporal pulse is indicative of *either* one or many operating modes. A chaotic temporal profile would be indicative of mode beating between several competing modes. Also, as a consequence of the long 75 cm cavity length of the oscillator, the optical build-up time of the cavity limits the narrow line pulse to roughly half the duration of the pump pulse.

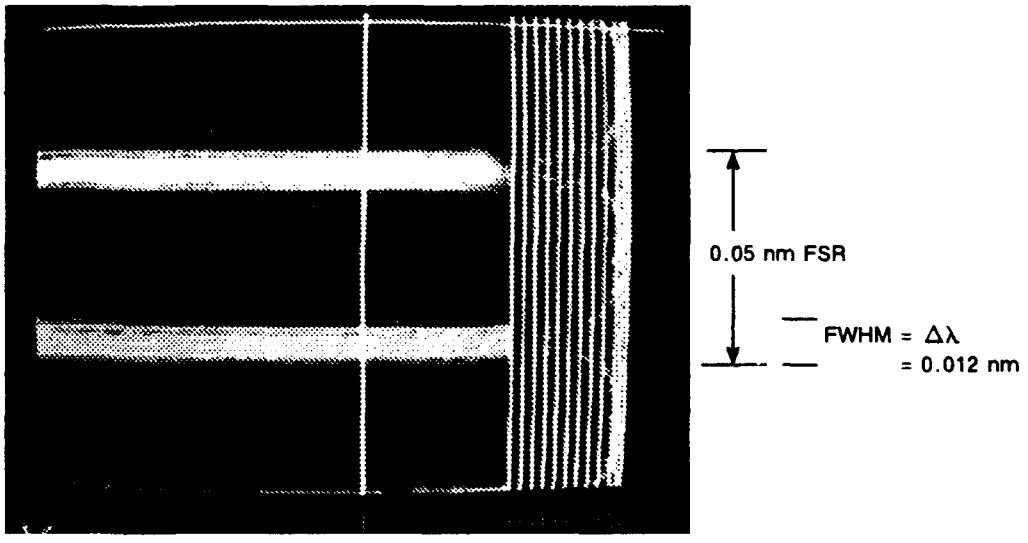

Figure 9. Interference fringes produced using a Fabry-Perot etalon. The spectral width of the laser pulse from the existing UTRC laser is found to be ~0.01 nm, as indicated.

89-10-16-4

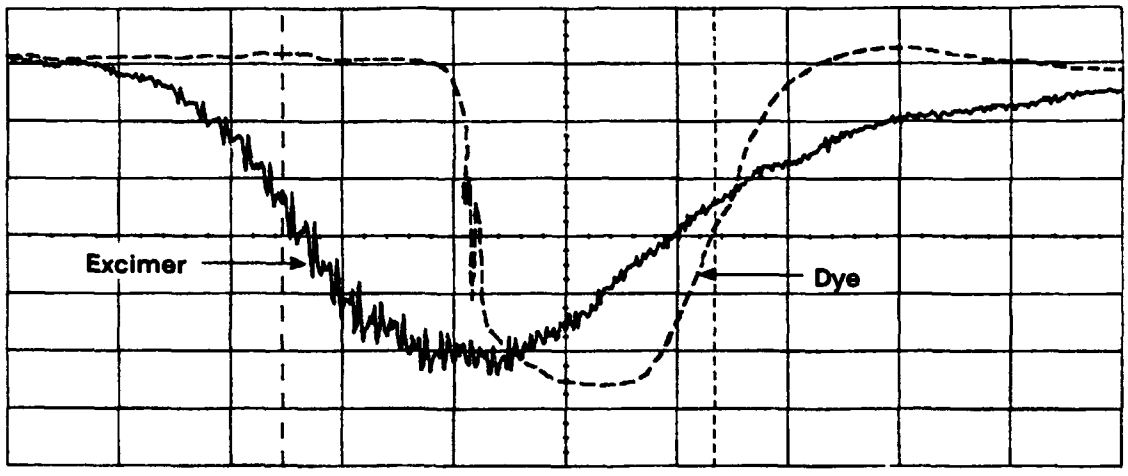

Figure 10. Comparison of the UV excimer pump and dye laser temporal pulses. The dye laser pulse duration is ~ 12 ns (FWHM).

89-10-16-7

2.2.2 Spectral Purity

The Rice XeF(C-A) amplifier requires an injection source having relatively high spectral purity, i.e., a low amplified stimulated emission (ASE) fraction in the direction colinear with desired narrow line laser output. Unfortunately, the high gain dyes characteristic of the blue end of the visible spectrum are subject to a relatively high ASE level. Accordingly, oscillators which operate in this region must be carefully designed to reduce the ASE content of the output beam. Typically, oscillators utilizing a grazing incidence grating design use the m = 0 order reflection as the output, as illustrated in Fig. 4. However, for the configuration shown in Fig. 5, tests have shown that up to 30% of the energy output in the m = 0 beam is ASE, as illustrated by the data shown in Fig. 11. For this reason, the m = 0 reflection *cannot* be used for the XeF(C-A) laser application.

The ASE fraction of the output can be reduced to an acceptable level by using the m = 1 reflection. As shown in Fig. 5, this can be accomplished by using a polarizing beam splitter as a partially transmitting outcoupler. The energy in the beam from the dye cell is filtered twice by the grating before returning to the dye cell and then to the output coupler. Furthermore, owing to the random polarization of the ASE, as opposed to the linear polarization of the narrow line lasing, the polarizing beam splitter reduces ASE an additional 50%. With this arrangement (Fig. 5), the oscillator spectral purity was found to be $\geq$ 96% over the entire system bandwidth, as illustrated by the spectral data shown in Fig. 12.

2.2.3 Bandwidth

In order to cover the exceptionally wide gain profile of the XeF(C-A) amplifier ($\sim$ 75 nm), at least two different dyes are required. Accordingly, the UTRC injection laser oscillator was designed to be as achromatic as possible, with wide band anti-reflection coatings and a minimum of wavelength dependent optics. However, as the data of Fig. 13 show, the system gain profile using Coumarin 102 is $\sim$ 20 nm (FWHM), significantly less that the $\sim$ 40 nm dye gain profile. Without the reducing telescope the nominal gain profile of the system is approximately 50 nm. Thus, in spite of the AR coatings, the "fast" telescope optics requiring twelve additional surfaces, reduce the oscillator bandwidth to $\sim$ 20 nm.

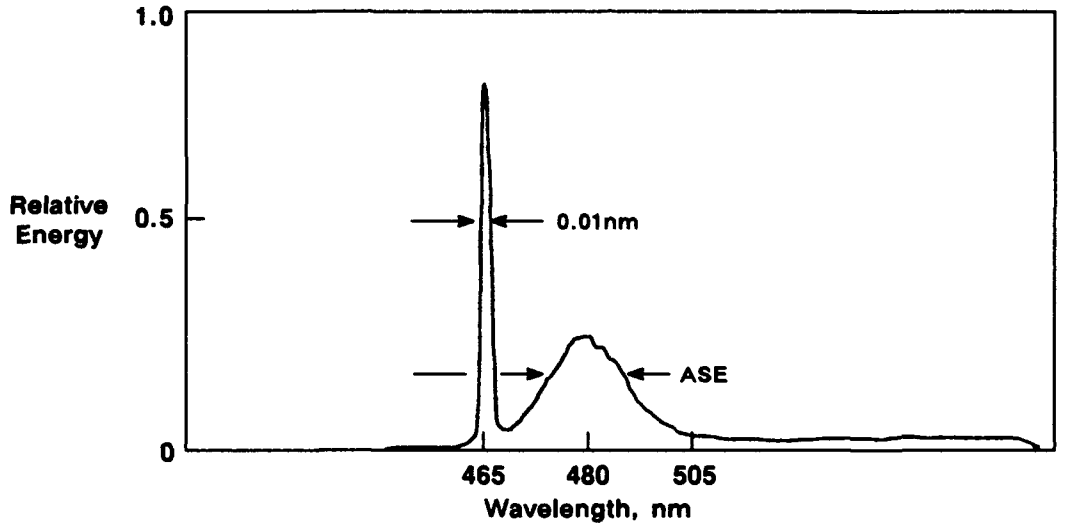

Figure 11. Illustration of the ASE content of the m=0 grating reflection of the UTRC laser as presently configured (Fig. 5).

89-10-16-5

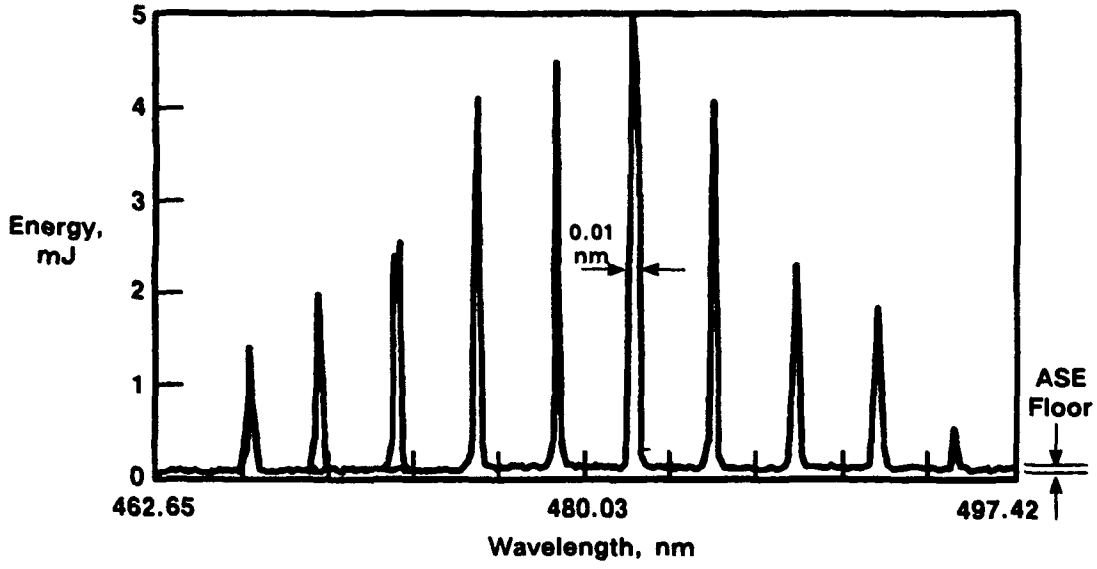

Figure 12. Representative spectral output of the existing UTRC laser using the m=1 grating reflection (Fig. 5). A 100 mJ pump pulse at 308 nm was used to pump Coumarin 102. Each wavelength corresponds to a different shot. For these conditions the ASE content is ≤ 4% over the entire band.

89-10-16-26

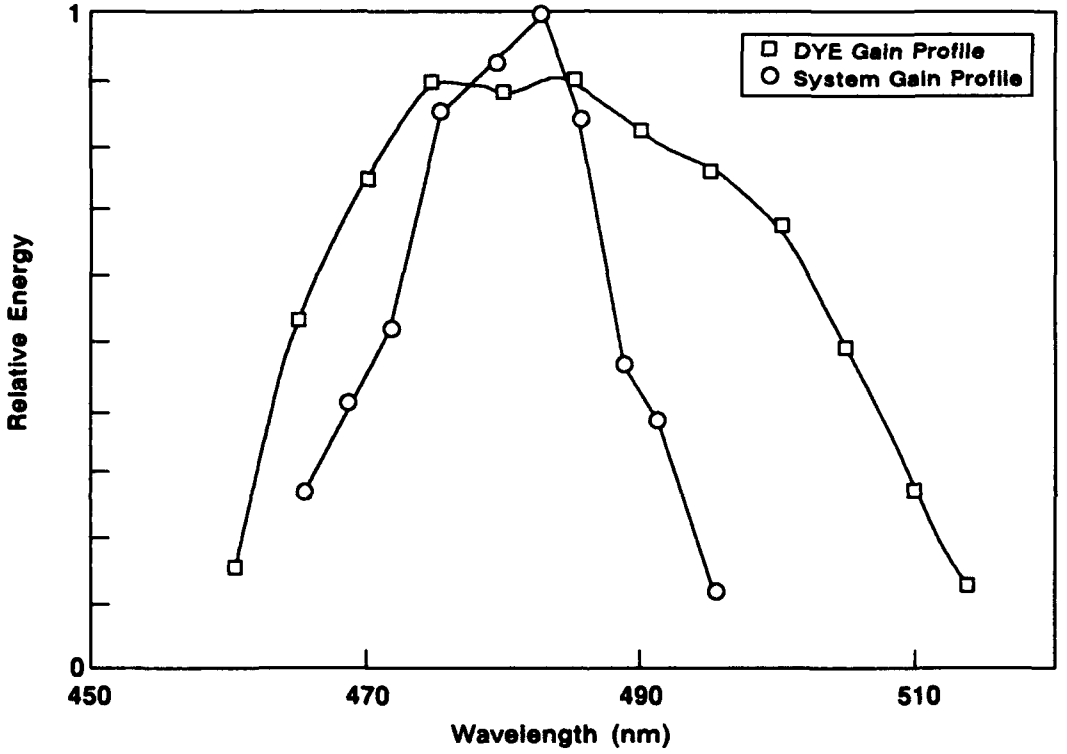

Figure 13. Comparison of the spectral energy profile of the existing UTRC laser with the gain profile of Coumarin 102.

89-10-16-6

Since three dye changes were originally thought necessary to cover the XeF(C-A) gain profile, the cost of an additional dye change was perceived as a minimal penalty when weighed against demonstration of high speed wavelength agility, an objective of the UTRC research. *In fact, bench tests of the galvanometer have shown repetition rates for full scale deflection of the 10 mm mirror of up to 200 Hz, with no degradation in angle pointing accuracy.* The actual wavelength accuracy of the galvanometer-tuned oscillator was verified using a Fabry-Perot spectrum analyzer and suitable detector array to be within ~ 0.01 nm over the entire 20 nm system bandwidth for repetition rates up to the 70 Hz limit of the excimer pump. Without the telescope, turning a 50 mm mirror would limit the PRF to approximately 10 Hz.

2.2.4 Amplifier

In order to saturate the XeF(C-A) transition, a minimum of 1 MW/cm^2 must be injected into the Rice amplifier (Ref. 7). To achieve this power density, an additional dye cell is utilized as an optical amplifier, as illustrated in Fig. 5. Approximately 90% of the excimer pump energy is delivered to the amplifier cell to pump a volume of 2.5 x 2.5 x 40 mm^3. Nominally, the non-saturated peak gain for the amplifier cell using Coumarin 102 is twenty. With a 100 mJ excimer pump beam, this arrangement results in a maximum efficiency of 6% and can deliver 6 mJ at the wavelength corresponding to the peak gain of the dye, ~ 480 nm. So as to ensure uniform narrow line operation over the entire 2.5 mm cross section of the amplifier cell, a 3x telescope is inserted between the oscillator and amplifier cells (Fig. 5).

An optical time delay between the pumping of the oscillator and amplifier cells is used to synchronize the arrival of the narrow line of the oscillator with the pumping of the amplifier. If the delay is properly chosen, the initial ASE spike from the oscillator is suppressed. Typically, the delay is on the order of the cavity build-up time of the oscillator, e.g., ~ 5 ns. For a non-optimized delay time, and with the dye laser operating off of the gain peak, an analyzing diffraction grating and a fast detector easily resolves the relative time between the ASE and narrow line operation. Using this technique, the shoulder preceeding the main lasing pulse (Fig. 14), was determined to be ASE and an

appropriate delay was chosen. For a 75 cm long oscillator cavity, a 6 ns delay was found to result in the most effective ASE suppression.

The required power density to completely saturate the dye amplifier is actually ~ 5 MW/cm^2. However, experiments show that the dye laser amplifier energy output is *not* saturated for conditions typical of the existing system. Nevertheless, since the 1 MW/cm^2 Rice amplifier requirement was easily met, the reduced system efficiency is not considered significant.

2.3 Laser Diagnostics

For the dye laser system depicted in Figs. 5-7, the integrated system diagnostics package is comprised of means for measurement of *absolute wavelength*, laser energy, and pulse spectral width *for each pulse*. Additionally, a port for an Optical Multichannel Analyzer (OMA) is provided. Overall system diagnostics account for no more than 10% of the total optical budget of the dye laser, a figure that is included in the overall 6% system efficiency (Table I). However, measurement of wavelength and energy for *every* shot imposes a maximum repetition rate of 10 Hz on the system as it is presently configured. In view of the ~ 1 Hz limitation of the scaled XeF(C-A) amplifier at Rice, this PRF limitation is not a factor. However, for operation above 10 Hz, alternate schemes can be incorporated in which the diagnostics are gated for non-repetitive sampling of laser shots. **Moreover, our experience with the dye laser indicates that after the initial system calibration of approximately 500 shots, system stability allows for *hours* of reliable operation.** Thus, based upon the experience of the first phase of our work, it appears that high repetition diagnostics may be waived altogether with minimal risk to system confidence, once the system has been calibrated at low PRF.

2.3.1 Fizeau Wavemeter

Owing to the pulse-to-pulse tunability and the short temporal pulsewidth of the dye laser, at the beginning of this program a Fizeau wedge-based wavemeter was the only commercially available technique for determining wavelength to the accuracy required (Refs. 10, 11). In principle, Fizeau wavemeter operation is straightforward and yields highly accurate results. However, as will be discussed, a host of subtle variables combine to make use of this instrument as an *online diagnostic* very difficult. Indeed, we have found that wavemeter operation can be erratic, particularly when the

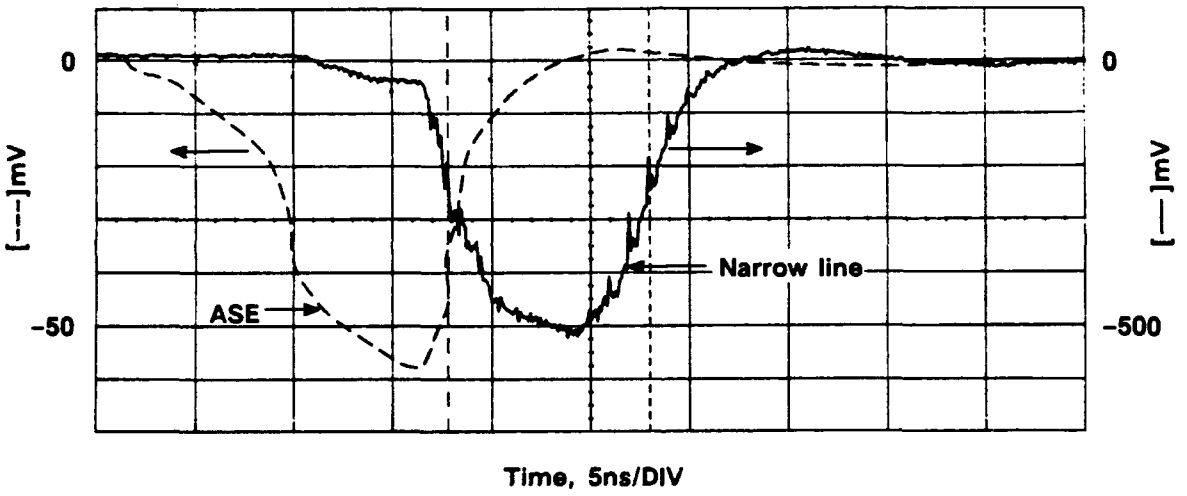

Figure 14. Illustration of the temporal delay between the initial broadband ASE output and the tuned, narrow spectral output of the UTRC laser.

89-10-16-10

wavemeter is used in conjunction with short pulse dye lasers, an experience substantiated by the work of others (Ref. 12). This problem had to be overcome in order to incorporate the Fizeau wavemeter in the system for *reliable on-line wavelength measurement.*

The basis of operation of this variety of wavemeter is an interferometric technique involving a Fizeau wedge. As illustrated in Fig. 15, light entering the wavemeter through an optical reference, expands to fill an off axis parabolic mirror, whereupon the beam is collimated and redirected to the Fizeau wedge. The air spaced, uncoated wedge resides within an evacuated, temperature controlled cell with an entrance/exit window so as to maintain long term absolute wavelength calibration. The two wave fronts reflected from the uncoated surfaces of the wedge propagate through a tilted compensation plate to cancel dispersion effects of the wedge, and subsequently impinge upon a photodiode array located at the plane of zero shear. The resulting interference of the two wave fronts produces a symmetric sinusoidal fringe pattern having an envelope determined by the near gaussian quality of the input beam. All things constant, the wavelength information is contained within the spacing and position of the fringes on the array. Immediately following a laser shot, the array is interrogated by a dedicated PC, and a series of mathematical operations are performed on the incoming data to reduce small uncertainties caused by non-uniformities of the fringe pattern. By a series of calculations whereby the first wavelength determination is used to begin the second of three iterations, the absolute wavelength can be determined to an accuracy of 5 parts in 10^7.

It has been our experience that problems associated with this variety of wavemeter can be reduced to two categories: (1) gross errors on the order of 0.1 nm associated with inadequate pre-conditioning of the input laser beam, and (2) minor instrumental inaccuracies, less that 0.01 nm, owing to temperature drift and gross light intensity fluctuations. The latter category are of minor importance for our purposes, since these fluctuations are less than or equal to the original laser spectral width. However, the gross errors which are typically characterized by a $\pm$ 0.12 nm wavelength error, corresponding to the free spectral range (FSR) of the wavemeter at 480 nm, are associated with errors in determining the order number of the interference pattern (Ref. 12). That these order errors do not represent true wavelength fluctuations has been confirmed by the use of a Fabry-Perot spectrum analyzer of non-multiple FSR. Furthermore, analysis of the wavelength determination algorithm

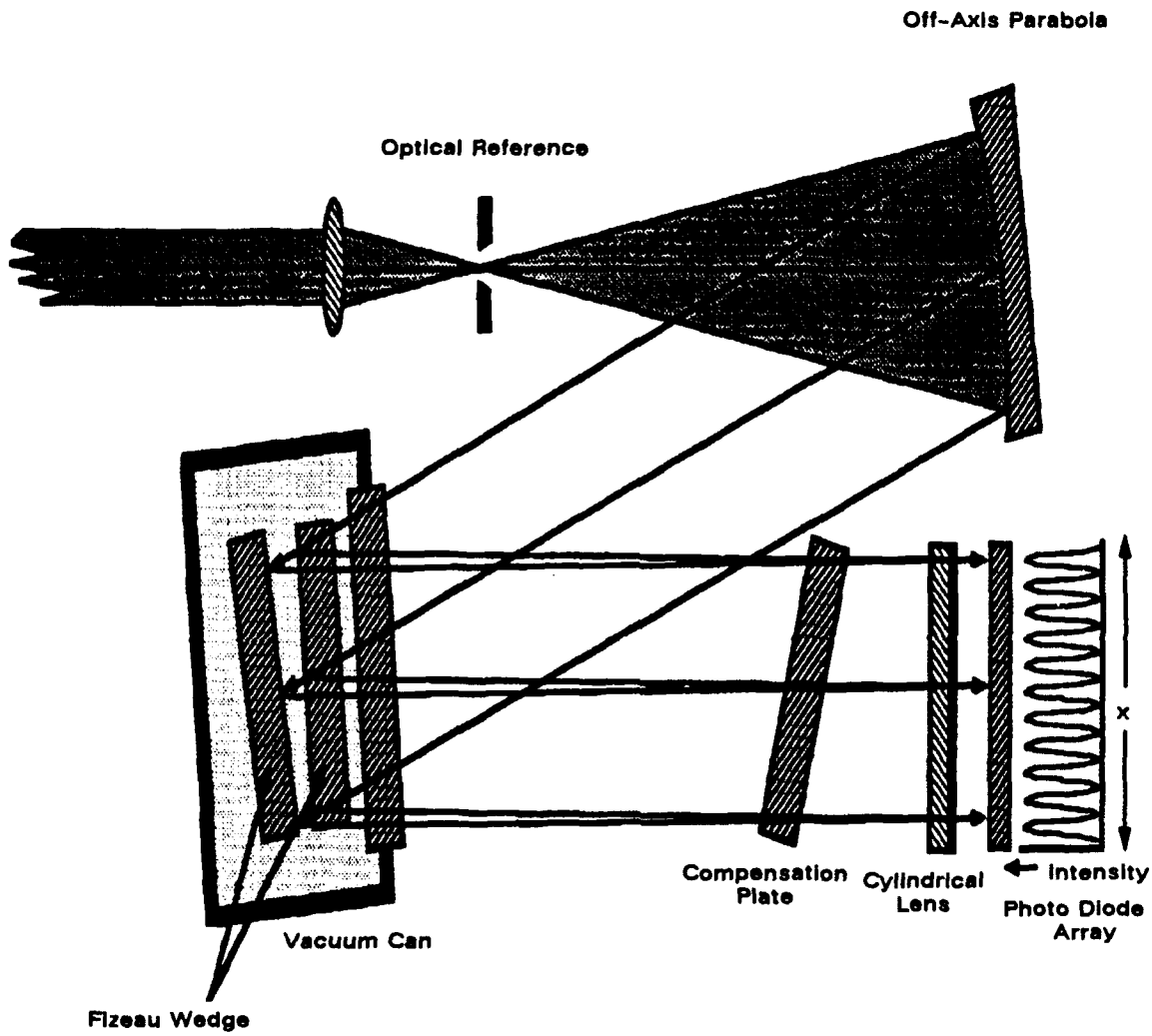

Figure 15. Schematic illustration of the primary elements of the Fizeau wavemeter.

89-10-16-3

suggests that wavelengths which are an integer multiple of the Fizeau wedge FSR will always be subject to this type of uncertainty.

For a grazing incidence dye laser oscillator such as the one depicted in Fig. 5, we have found that the number of wavelengths subject to spurious order estimates can be as large as 30%. That level of uncertainty is unacceptable for an *on-line* diagnostic system. Unfortunately, owing to the optical inefficiency of the wavemeter and the short temporal pulse length of the laser, the resultant extreme optical peak power densities (60-600 MW/cm^2) make the obvious solution of pre-spatial filtering with standard metal pinholes difficult and unreliable. **This represented a very serious problem that had to be solved.**

As a solution, a spatial filter consisting of a 42 cm lens and 50 micron *diamond* pinhole was installed *external* to the wavemeter to remove all shot-to-shot spatial fluctuations inherent in a laser of this design. Additionally, although the optical reference *internal* to the wavemeter is still used to serve as a low power alignment aid, it too has been replaced by a *diamond* pinhole. Most important, the high power optical reference is now provided by the *external* spatial filter. By increasing the optical spot size 20 fold and replacing the standard metal pinholes with *diamond* pinholes, the life of the spatial filter and optical reference can be on the order of several million shots, an enormous improvement over our initial experience (Ref. 13). As important, a true TEM_{00} beam provided through a non-eroding optical reference now results in order estimate errors on fewer than 1% of the laser shots. Error rates at this low level are easily identified by the system computer and handled accordingly. **Thus, the UTRC injection laser system features a reliable on-line wavelength measurement system capable of measuring wavelength for each pulse of the Rice XeF(C-A) amplifier.**

2.3.2 Spectral Width Measurement

An additional feature of the Fizeau wedge wavemeter is the capability of real-time measurement of the spectral width of the laser output using the contrast ratio of the fringe pattern. The decrease in contrast is analogous to the broadening of Fabry-Perot fringes. The fringes for the Fizeau case, however, are so closely spaced that the broadening tends to fill in the fringe minima and thus reduces fringe contrast. To accurately determine the fringe contrast, the spectral width measurement takes into

account the photodetector array zero level for a particular repetition rate, and the scattered light background caused by non-ideal optics and residual ASE. To further reduce errors, the algorithm uses only the central 80% of the detector array and only maxima above 25% of a full scale signal. The technique permits measurement of spectral widths as small as 0.2 GHz, i.e., ~ 0.0002 nm. However, utilization of this capability reduces the throughput rate of the wavemeter to ~ 5 Hz, and for this reason the line-width measurement is used only as a benchmark of laser performance and not as a real time diagnostic.

2.3.3 Energy and Temporal Width Measurement

Relative energy measurement of the dye laser output is provided by a fast pyroelectric detector with little spectral dependence on energy measurements. The detector displays a linear response for energies from 10^{-6} to several Joules. Referring to Fig. 16, surplus optical energy from the wavemeter is brought to the EMI shielded energy meter through a multimode fiber cable. Real-time energy measurements are communicated to the control computer via a high speed RS-232 fiber-optic link to avoid EMI.

The inclusion of a fast silicon photo-diode of 1 ns response time in the energy probe head allows for temporal measurement of the dye laser pulse. However, owing to the low signal amplitude and fast response time of the detector, EMI isolation is difficult. As a consequence, temporal information is not a real-time diagnostic and is provided only as an off-line utility.

2.4 System Characteristics

2.4.1 Control Strategy

As stated earlier, the overall design of the UTRC master oscillator laser for the Rice, 'C-A' application has been one of simplicity and reliability. Since the ultimate achievement of success for the dye laser injection source is solely dependent upon the integrity of the entire system, design of the system control and monitoring strategy must also be based on the same philosophy of simplicity and reliability. In light of this, the master oscillator control system as depicted in Fig. 17, has been built around a single IBM-compatible personal computer. Through this computer, system control and

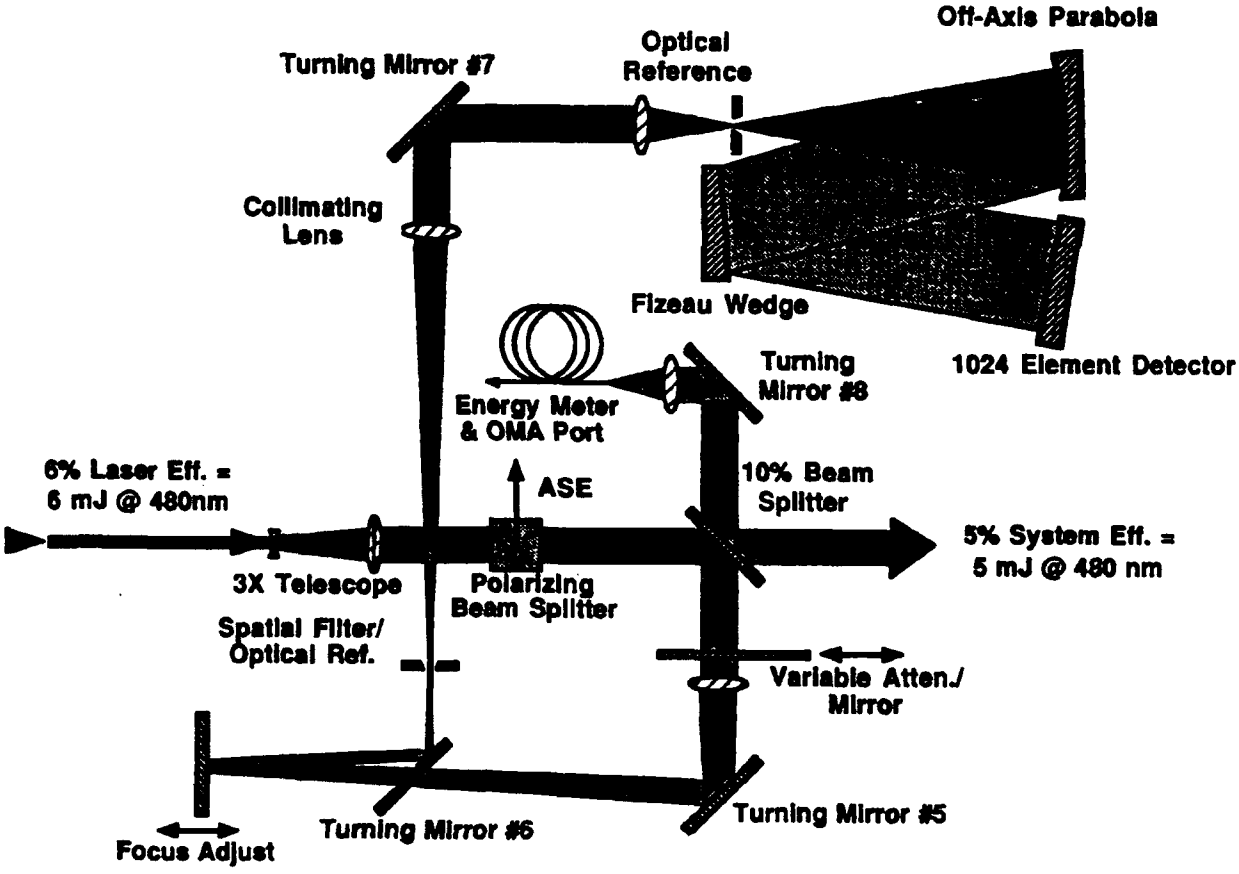

Figure 16. Schematic illustration of the wavelength and energy measurement diagnostics of the existing UTRC laser.

89-10-16-2

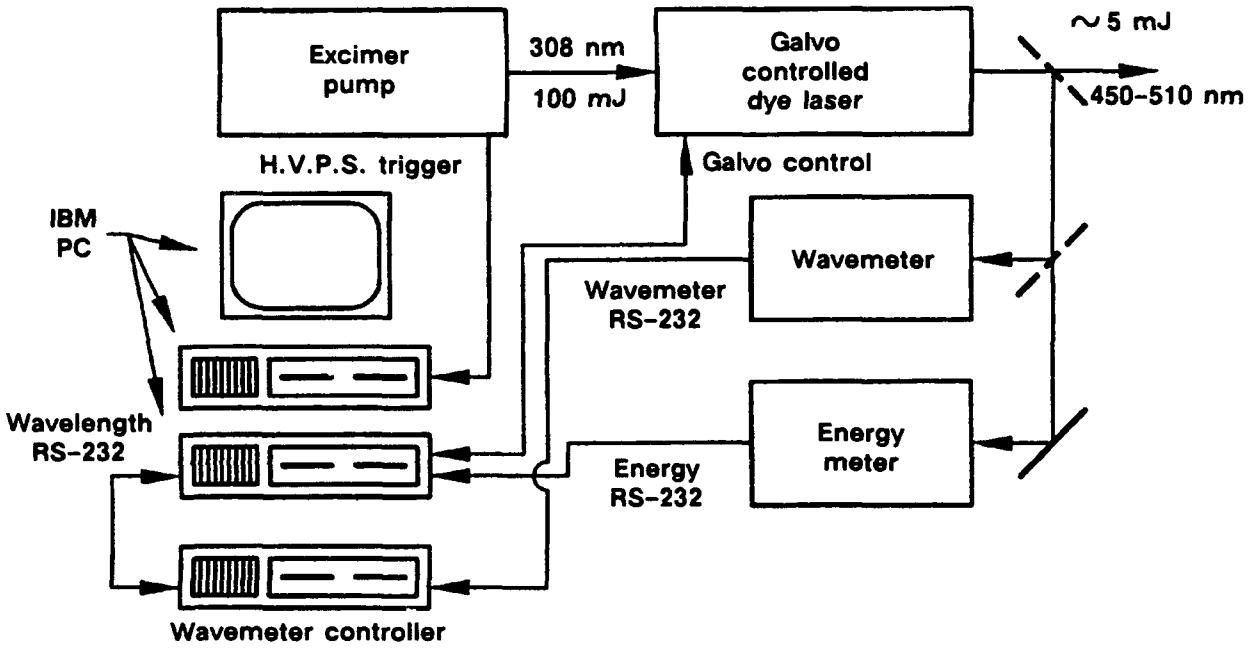

Figure 17. Illustration of the control system for the existing UTRC laser.

89-10-16-8

diagnostics are presented in a real-time informative graphics format as well as being logged for later retrieval. To ensure system reliability and protection of delicate control electronics, a comprehensive isolation and shielding scheme was implemented. The result is a wavelength-agile dye laser system which approaches "black box" operation.

2.4.2 EMI Shielding

A major concern in terms of system reliability, has been the extremely high EMI level produced by the Rice electron beam pumped amplifier system, which impacts significantly on both the UTRC injection laser and all associated control electronics. The EMI threat can be classified into two general categories: (1) interference with measurements of parameters occurring in coincidence with the EMI pulse, and (2) disruption or damage to delicate control or monitoring electronics. All diagnostics involving the sampling of the laser pulse fall into the first category. This type of interference is usually alleviated by locating the sensor in question in an EMI shield box and delivering the data via fiber-optic cable. However, operation of the Fizeau wavemeter requires high energy laser pulses sufficient to produce non-linear effects in fiber-optic cable which can lead to spurious Raman harmonics. Thus, shielding the wavemeter is more involved and must be accomplished *in situ*, with only the relevant timing and video signals communicated over fiber-optic links back to the wavemeter's control computer.

Control electronics, such as the galvanometer driver, fall into the second category by virtue of the fact that the galvanometer cannot respond mechanically fast enough to effect wavelength variations during the shot. This is not to say, however, that proper shielding and isolation of electronics in this category can be dismissed. To do so, in light of the close proximity of these electronics to the electron beam transmission line, raises serious survivability issues. In response to this risk, the majority of the electronic systems, such as the energy meter, galvo driver, and digital links, are located remotely in a nearby front-end EMI shield box. For electronics too large to fit in the front-end EMI box, a screen room housing the system computer and operator is provided. Communication from the screen room to the laser is via fiber-optic digital and analog links with the addition of a limited number of specially shielded and isolated coax cables.

2.4.3 Computer Control

During electron beam operation at Rice, the low level x-radiation near the electron beam transmission line requires the operator to perform systems control a safe distance from the dye laser. Hence, a great deal of effort has been expanded in developing a user friendly, menu-driven laser control and diagnostic software package which is both flexible and comprehensive in monitoring dye laser parameters.

In this regard, a graphic intensive format for display of system parameters was chosen to facilitate trend identification and troubleshooting. For repetition rates higher than 1 Hz, this becomes increasingly important. During data runs, the graphics presentation is accompanied by a complete data log for post-run analysis. Additionally, if repetition rates higher than 10 Hz are desired, a mode in which the diagnostics are waived can be selected. This mode has been tested up to the pump limit repetition rate of 70 Hz.

Figure 18 shows a photograph of the entire UTRC wavelength agile dye laser system in operation. This system was delivered to Rice University, in November of 1989 and has been in daily operation since then, as described in Section 3.0.

2.5 Injection Laser Performance - Wavelength Agility Demonstration

To the extent to which the entire ensemble of sub-systems performs as intended, a critical test of system performance is the accuracy with which a list of pre-selected wavelengths can be addressed. As a demonstration of this capability, a *randomly addressed* list of 6 wavelengths corresponding to transitions of the *Rubidium atomic resonance filter* was selected (Ref. 14). The laser repetition rate was 5 Hz and the number of cyclic iterations was 100. Table II shows an abbreviated listing of the *desired* and *measured* wavelengths and the pertinent statistics for this sampling. All 600 shots were within specifications with a standard system error (bias) not exceeding 0.008 nm and a standard random error (variance) of 0.001 nm.

The standard system error, the difference between the desired and the mean wavelength for all 100 shots, is tabulated for each of the desired wavelengths at the bottom of Table II. The system error

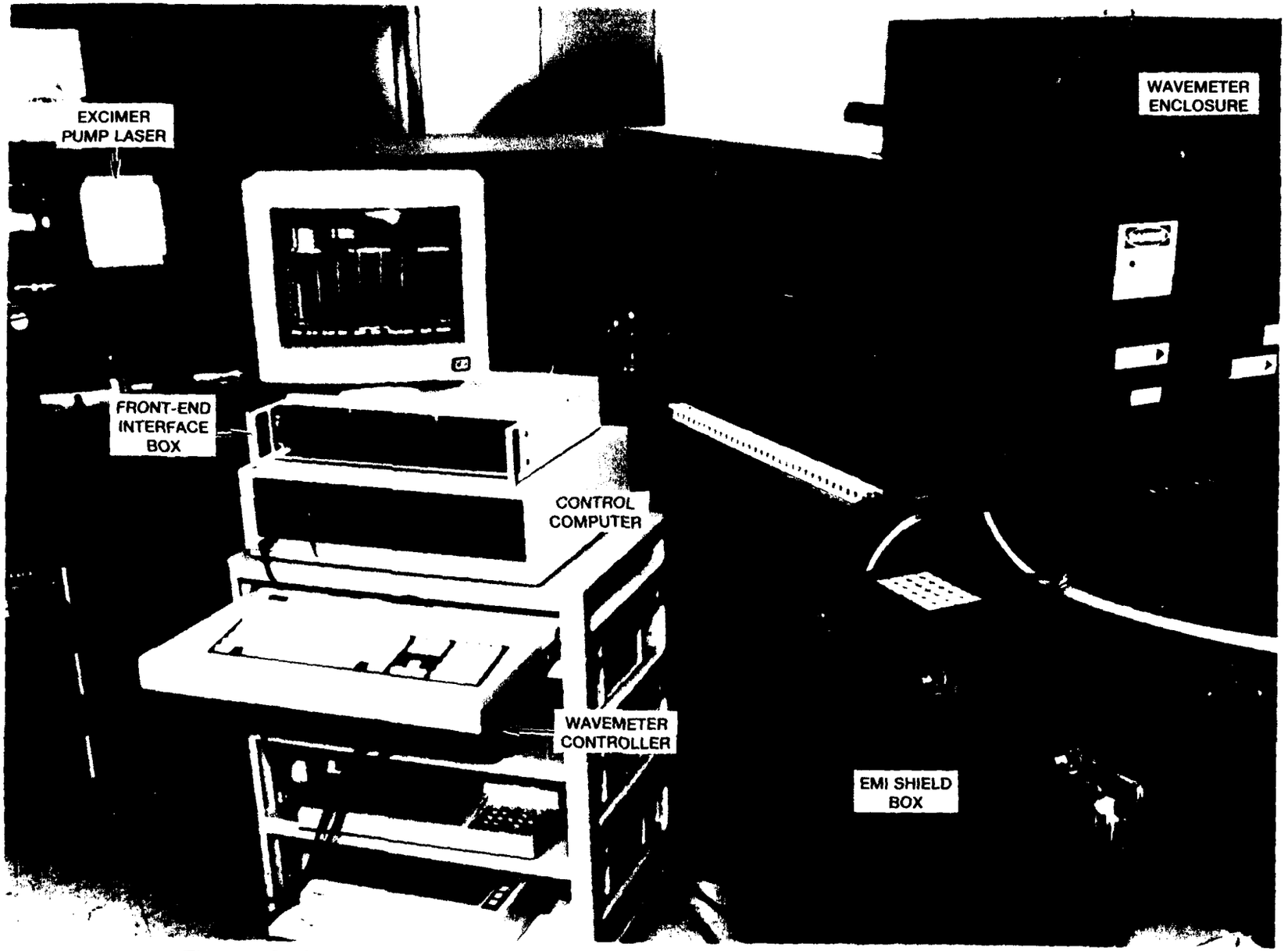

C-89-299-D-3

Figure 18. Photograph of the UTRC wavelength agile dye laser system in operation at UTRC.

89-10-16-21

accounts for non-random, system-attributable uncertainties, e.g., calibration errors, finite digital-to-analog conversion (DAC) accuracy and galvanometer drift. The effect of these errors on wavelength accuracy is typically characterized by a reoccurring trend. Close inspection of calibration data, wherein a galvo voltage is associated with a wavelength, reveals a repeatable step-like function superimposed on what should otherwise be a smooth curve. The magnitude of these steps and the system errors in the table approximate the least significant bit error of 1 part in 4096 associated with a 12 bit DAC. Hence, one can conclude some improvement in wavelength accuracy can be gained through employing a 16 DAC. The limiting factor then becomes random error effects.

The random error figures in Table II, correspond to a standard error calculation of the deviation of wavelengths about a mean wavelength for 100 shots. This represents random disturbances in the wavelength accuracy indicative of system "noise" such as, galvanometer wobble, electronic noise and wavelength uncertainty due to the centroid uncertainty of a "broad" spectral linewidth. Decreasing spectral width of the laser will reduce the uncertainty in wavelength determination, however, the hard limit here is related to the mechanical nature of the galvanometer and electrical noise associated with its control. Using the present random error as a conservative limit, we conclude a fivefold increase in system accuracy may be achievable, corresponding to system errors on the order of 0.001 nm.

Finally, it should be emphasized that all 600 shots fall within specification, and no measured wavelength jumps characteristic of wavemeter order-estimate errors were observed. This in itself is a statement of the reliability of the wavemeter and the UTRC injection laser system as a whole.

TABLE II

INJECTION LASER WAVELENGTH AGILITY DEMONSTRATION

	DESIRED RUBIDIUM WAVELENGTHS					
Iteration	495.6100	489.6900	492.6500	487.3800	491.9600	489.1500
1	495.6118	489.6862	492.6479	487.3850	491.9607	489.1529
2	495.6109	489.6863	492.6473	487.3837	491.9583	489.1538
3	495.6102	489.6843	492.6479	487.3853	491.9564	489.1550
4	495.6105	489.6869	492.6464	487.3845	491.9575	489.1535
5	495.6102	489.6847	492.6459	487.3843	491.9570	
6	495.6096	489.6844	492.6451	487.3840		
7	495.6086	489.6842	492.6453			
8	495.6078	489.6831				
9	495.6083					
91						489.1487
92					491.9549	489.1501
93				487.3814	491.9562	489.1489
94			492.6435	487.3818	491.9551	489.1495
95		489.6820	492.6432	487.3816	491.9538	489.1495
96	495.6076	489.6811	492.6444	487.3811	491.9551	489.1498
97	495.6062	489.6830	492.6446	487.3815	491.9551	489.1493
98	495.6079	489.6812	492.6417	487.3813	491.9552	489.1503
99	495.6076	489.6826	492.6433	487.3837	491.9541	489.1500
100	495.6076	489.6810	492.6440	487.3822	491.9546	489.1511
Average	495.6074	489.6821	492.6438	487.3818	491.9551	489.1502
System Error	-0.0026	-0.0079	-0.0062	0.0018	-0.0049	0.0002
Random Error	0.0011	0.0012	0.0011	0.0010	0.0010	0.0012

3.0 WAVELENGTH AGILE XeF(C-A) LASER DEMONSTRATION

3.1 System Integration at Rice University

After completion of fabrication and extensive optical testing of the UTRC wavelength-agile dye laser injection source, as described in Section 2, in November of 1989 the system was shipped to Rice University for integration with the scaled XeF(C-A) laser amplifier. Previously, the Rice amplifier had been operated successfully at the 1 J per pulse level on a repetitively pulse basis, albeit at a single wavelength. Additionally, the Rice amplifier was tuned manually over a 50 nm range. **The objectives of the research planned for the integrated Rice and UTRC systems was demonstration of repetitively pulsed tuning of the XeF(C-A) laser at the joule-per-pulse level i.e. wavelength agility—combined with reliable, robust system operation.**

Upon arrival at Rice University in Houston, integration of the injection laser and the C-A amplifier was easily accomplished. The standard Lambda Physik laser that had been used by Rice for single-shot experiments was replaced by the modified UTRC *wavelength-agile* source. Figure 19shows a photograph of the entire system, and the arrangement of system components is shown schematically in Fig. 20.

3.1.1 Optical Delay Line

With the exception for a requirement for an optical delay line between the injection laser and the 'C-A' amplifier, incorporation of the wavelength agile source with the Rice control and diagnostic strategy was entirely straightforward and in accordance with plan. The need for the delay line is a consequence of the positive branch geometry of the 'C-A' amplifier, which would result in axial reflections from the convex amplifier optic back to the injection laser shutting down the gain medium of the dye laser. To prevent these reflections from entering the dye laser during its pumping, a 25 ns optical delay equal to the duration of the injection pulse was inserted between the amplifier and dye laser as shown in Fig. 20.

Owing to the large (5mm) diameter of UTRC injection source beam, the existing compact, multi-pass delay line comprised of two small aperture retro- reflecting prisms had to be replaced with

an 8 meter optical path length "trombone". Though this technique lacked the elegance of the prism approach that had been in use at Rice, the number of relective surfaces and associated losses was greatly reduced, allowing for higher injection energies coupled into the 'C-A' amplifier. Initial testing showed that this technique, in conjunction with the relatively smooth temporal UTRC injection laser profile (compared to the unmodified Lambda Physik dye laser), permitted output energies of ~ 1.0 J from the XeF(C-A) amplifier when the system was operated in a single shot mode. **Demonstration of 1 Joule 'C-A' laser output from the *integrated systems*, combined with reliable, trouble-free operation represented a significant program milestone.**

3.2 Wavelength Agility Experiments

Demonstration of random-sequence XeF(C-A) laser wavelength agility at the 1 J per-pulse level was a primary objective of the Rice-UTRC program. This required operation of the electron-beam driven XeF(C-A) amplifier at its rated 1 Hz repetition rate which, in turn, required development by Rice of a an effective gas flow system to eliminate thermally-induced turbulence in the gain medium. The resulting transverse flow, gas recirculating system for the XeF(C-A) amplifier is readily apparent in Fig. 19, and is described in detail elsewhere (Ref. 15). Interferometric measurements with this system have shown complete thermal relaxation of the laser gas within 40 ms after electron beam excitation. In spite of the present 1 Hz limit of the electron-beam facility, the design goal of much higher PRF's for the gas conditioning system and the dye laser was desired for the purpose of demonstrating compatibility with future development of electron-beam technology.

For high speed, non-mechanical beam pointing applications wherein the beam direction depends on the wavelength of the laser beam as explained in Section 1, a large bandwidth combined with wavelength accuracy are required. To demonstrate compatibility of the agile XeF(C-A) system with this application, the first wavelength agility experiment involved *random sequence* tuning of the XeF(C-A) laser over a ~ 30 nm wavelength range corresponding to the gain bandwidth of the Coumarin 102 dye laser; the operating PRF was 1 Hz. The wavelength of the injection laser was changed for each shot in a pre-programmed, but random sequence. Figure 21a presents the resulting output energy and wavelength of the pulse train as a function of time. The observed difference in output energies for the various wavelengths is a reflection of the 'C-A' gain profile. Figure 21b shows

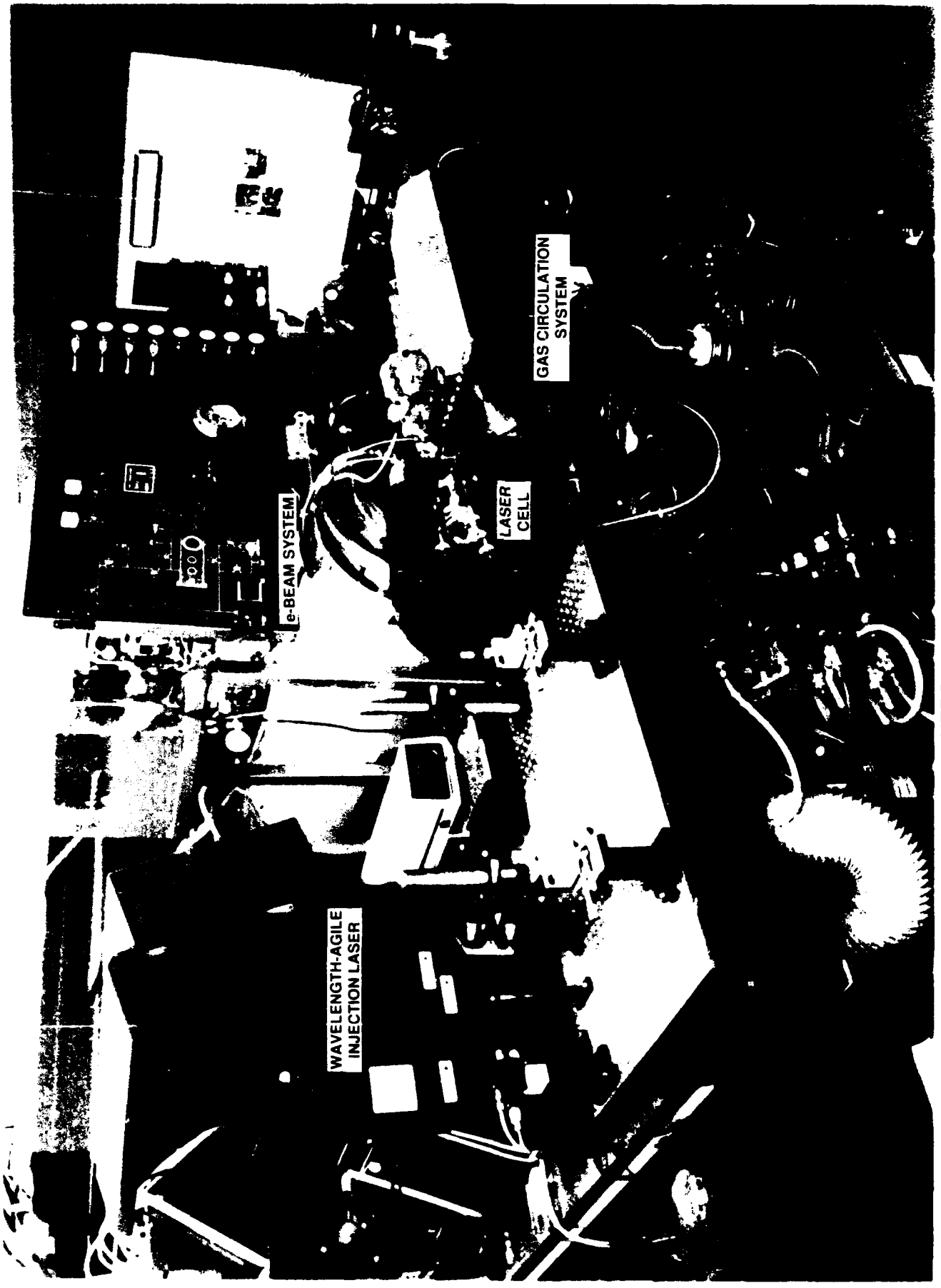

Figure 19. Photograph of the Rice-UTRC wavelength agile XeF (C - A) laser system at Rice University in Houston.

90-3-38-15

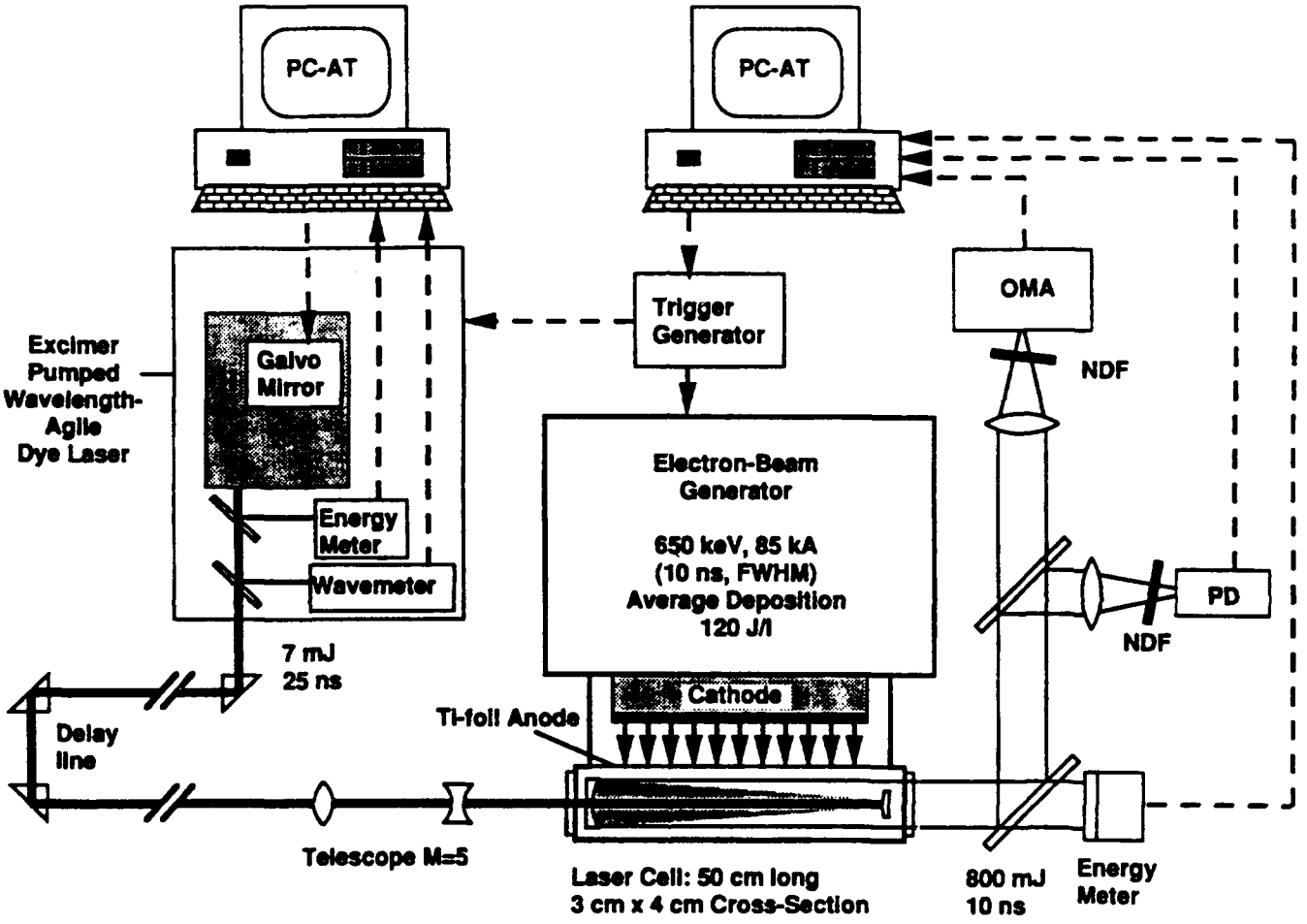

Figure 20. Schematic illustration of the Rice-UTRC wavelength-agile XeF (C - A) laser system.

90-8-38-4

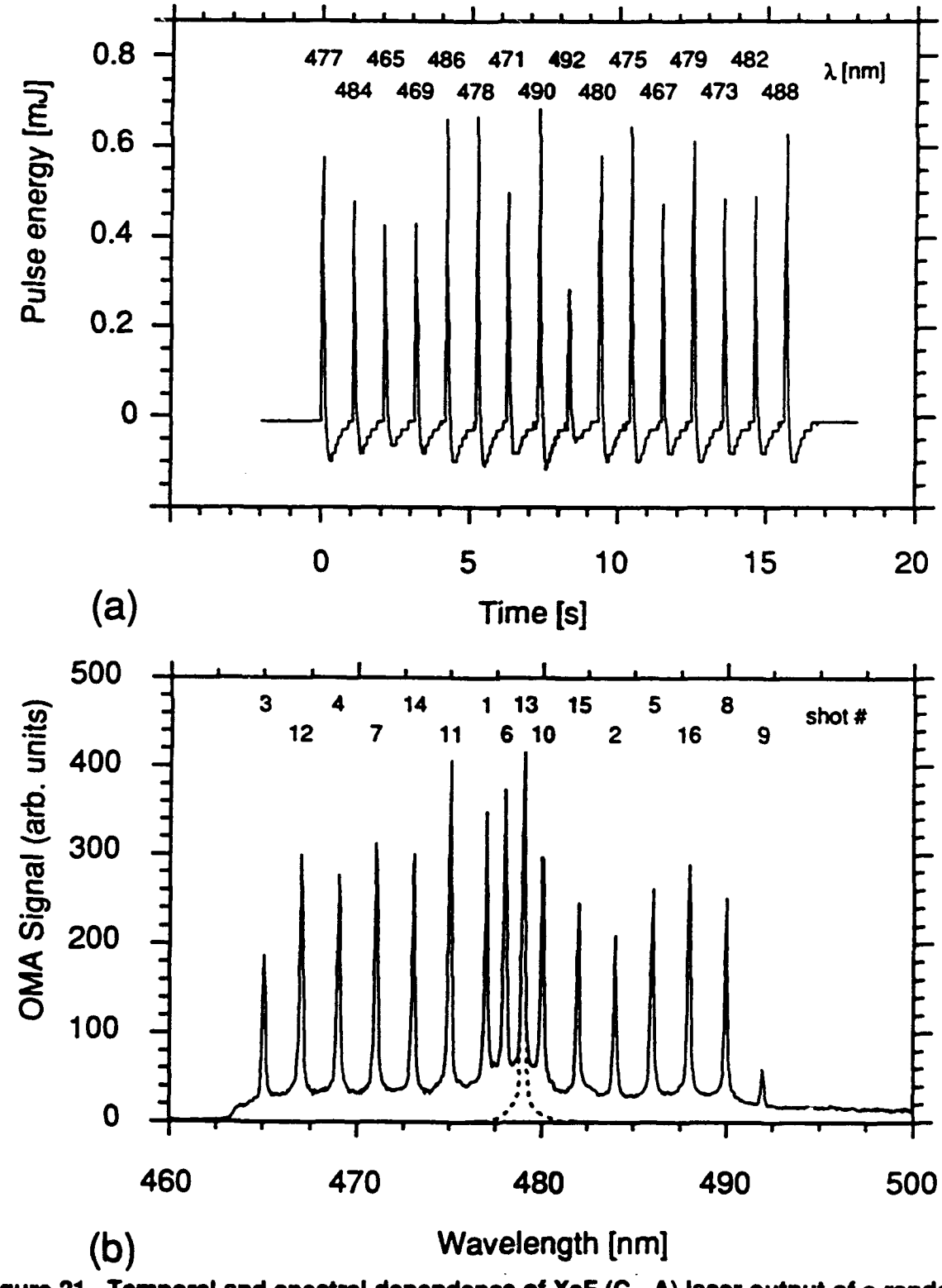

Figure 21. Temporal and spectral dependence of XeF (C - A) laser output of a randomly wavelength tuned 1 Hz shot sequence.
(a): Pulse energy versus time. The wavelength of each shot is indicated.
(b): Spectrum of the same shot sequence shown in Figure 21a recorded by an OMA. The elevated base line is due to a summation of pedestals of the shot recordings. The numbers at the top of the figure represent the order in which the shots were taken.

90-8-38-5

the wavelength spectrum corresponding to the data of Fig.21a. The origin of the background plateau accompanying the narrow-line output (Fig. 21b) is instrumental rather than amplified spontaneous emission (ASE) and is a result of integration of 16 individual shots. The OMA trace for a single shot at 479 nm is represented by the dotted line and shows an associated ASE background of less than 1 percent. The wavelength accuracy of the 'C-A' laser output, as measured by the OMA, is equivalent to that of the pre-selected dye laser injection wavelengths to within the OMA resolution of 0.1 nm.

3.3 Atomic Resonance Filter Application

To simulate a remote sensing or similar application for which an atomic resonance filtered (ARF) detection system might be employed (Ref. 14), an experiment was carried out to demonstrate the ability of the wavelength agile XeF(C-A) laser system to address four of the atomic Rubidium transition wavelengths. Figure 22 presents the output energy and wavelengths for a 1 Hz XeF(C-A) laser pulse train. Two consecutive sweeps through the four Rb wavelengths were made to demonstrate overall system stability. Output energies of ~0.7 J were obtained for the wavelengths 489.7 nm, 489.2 nm and 487.4 nm. The lower output energy at 492.0 nm results from the reduced injection energy of the dye laser operating in the gain wings of the dye, and is not a limitation of the XeF(C-A) laser amplifier. In both wavelength sweeps the desired wavelengths were obtained and output energy variations of less than 10% were observed.

3.4 Speckle Imaging Illuminator

Another possible application of a wavelength agile illuminator is speckle imaging. Although an experiment designed to simulate this unconventional imaging technique was not performed at this time, the basic requirements fo the illuminator required, such as: output energy, wavelength tuning, wavelength accuracy and PRF level have been met by the UTRC wavelength-agile injection laser. However, imaging of actual target geometries requires a **coherence length** on the order of 1 m, more than an order-of-magnitude greater than the ~ 2.5 cm coherence length of the present injection laser. To address this issue a 'second generation' injection laser design was developed, as discussed in Section 4.0

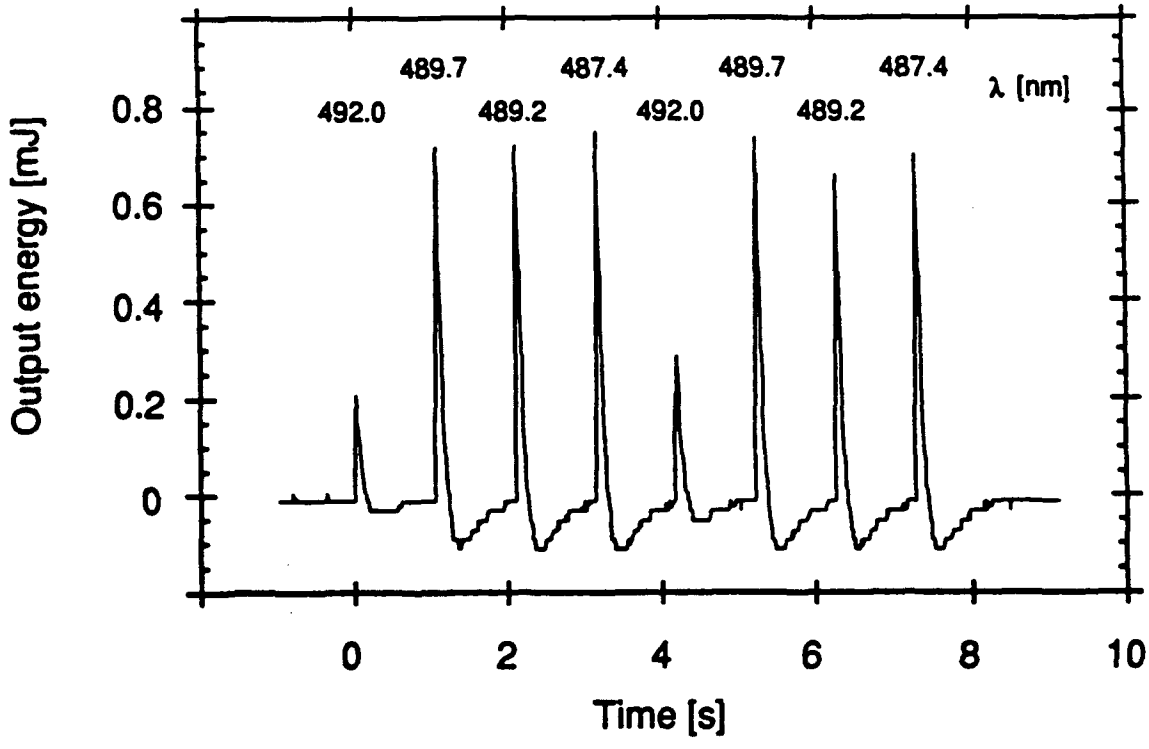

Figure 22. Temporal scan of XeF (C - A) laser output energy for four wavelengths corresponding to rubidium transitions. The wavelength of each shot is indicated at the top of the figure. The PRF was 1 Hz; the four-wavelength sequence was repeated as described in the text.

90-8-38-6

4.0 INJECTION LASER WITH IMPROVED COHERENCE PROPERTIES

4.1 Coherence Length

Coherence length refers to the temporal coherence of the transmitted laser beam, and can be thought of as a physical length (L_c) for correlatable phase information of any section of the beam as it propagates through space. **In most imaging applications, *both* spatial and temporal coherence are required.** Not only must the wavefront be coherent across the width of the set of objects, but also the temporal coherence must be such that the coherence length of the beam must exceed the depth of the set of objects. Then, the returning wavefront will contain, in its spatial and temporal phase patterns, information about the sizes, shapes, positions and orientations of the objects. Spatial coherence is achieved by transmitting a beam with a coherent wavefront, while temporal coherence is achieved by narrowing the spectral linewidth of the beam. The temporal coherence length (L_c) of the beam depends on the linewidth ($\delta\lambda$), and can be expressed, as follows:

$$L_c = c\delta t = c/\delta f = \lambda^2/\delta\lambda$$

For the UTRC injection laser system described in Section 3.0, the spectral width is 0.01 nm, corresponding to a coherence length of ~ 2.5 cm. **The optical design required to achieve an order-of-magnitude improvement to a more useful spectral width of ~0.001 nm, or coherence length of 25 cm, is described in this section.**

4.2 Oscillator Redesign

In order to meet these coherence requirements it is clear that the existing oscillator section (Figs. 5, 6) will have to be modified. The modification will include the insertion of an intra-cavity etalon in the oscillator which will narrow the linewidth by approximately the order of the etalon finesse, resulting in a reduction in spectral width so as to produce a coherence length of ~25 cm. To compensate for the additional oscillator loss due to the presence of the etalon, the efficiency of the oscillator optics must be increased. Accordingly, since the present system PRF far exceeds the electron-beam repetition rates of the Rice XeF(C-A) amplifier, the reducing telescope used to obtain a high tuning rate for the UTRC 'C-A' injection laser (Fig. 5) will be removed in order to increase the

cavity efficiency. Likewise, further control of ASE is provided by the etalon permitting cavity outcoupling through the much more efficient m = 0 order of the diffraction grating, a very significant factor.

In our judgment, this approach would pose the minimum risk to system reliability. With this in mind, **an enhanced linewidth system will comprise all the system features incorporated in the original 'C-A' laser system, as described in Section 2, with the exception of the oscillator section.** Inasmuch as the control of the oscillator optics will still be galvanometer-based, changes to the oscillator will be relatively straightforward insofar as the existing control strategy is concerned. Hence, we are confident in the overall ability of these modifications to meet the projected coherence specifications and still maintain high energy efficiency.

4.3 System Parameters

The principal components of the redesigned oscillator are illustrated in Fig. 23. Once again, the principal tuning element is a 2400 l/mm grating used in *near* grazing incidence. The reasons for not using the grating in the *full* grazing incidence configuration are twofold: (1) grating efficiency drops off sharply for incidence angles $\gtrsim 70°$, and (2) beam expansion is required for the etalon anyway. As discussed in Section 3.0 increasing the coherence length to 25 cm requires a spectral width limit of approximately 1 GHz, i.e., $\sim$ 0.001 nm. Spatial coherence of the output beam could further derate this limit. To achieve the required degree of coherence, a single grating alone would be too large to allow for agile wavelength tuning. Hence, an additional wavelength selective element, namely a Fabry-Perot etalon, has been included in the redesigned cavity.

4.3.1 Etalon Specifications

The etalon is essentially a resonant type structure having a Q, or coefficient of finesse, defined by the reflectivity and figure of the optical flats, the latter given by the expression,

$$F = \left(\frac{2r}{1-r^2} \right)^2 , \qquad (1)$$

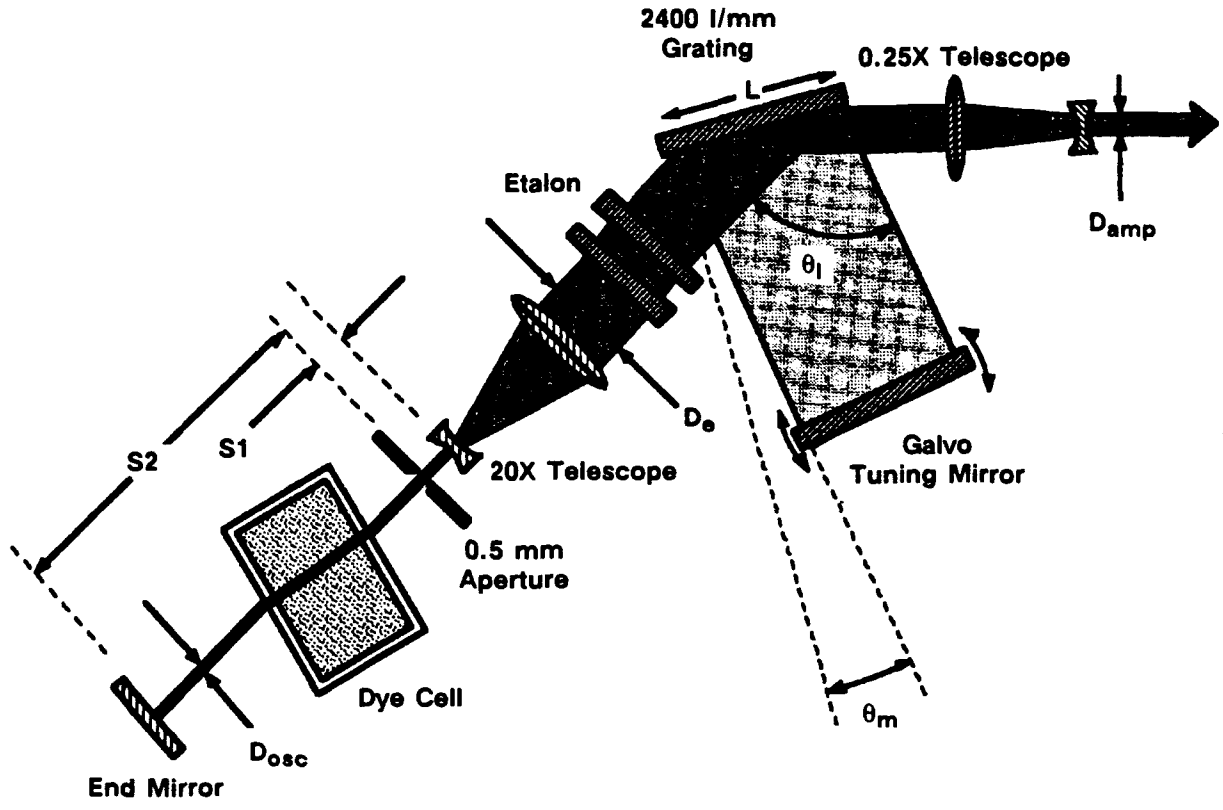

Figure 23. Principal elements of the proposed redesigned oscillator for enhanced linewidth and coherence operation.

89-10-16-11

where r is the amplitude reflectivity. High transmission through this element is achieved when the resonance condition for the etalon is met, and is characterized by a series of wavelengths differing by the free spectral range (FSR) of the etalon, expressed as,

$$\Delta\lambda_{FSR} = \frac{\lambda^2}{2d} \text{ or } \Delta\nu_{FSR} = \frac{c}{2d} , \tag{2}$$

where d is the air space between the optical flats. The width of the transmission band, or more important the spectral width of the laser, is defined by FSR/f, where f is the finesse of the etalon and is related to the coefficient of finesse by

$$f = \frac{\pi\sqrt{F}}{2} . \tag{3}$$

High reflectance, low loss dielectric coatings and quality optical flats allow for finesse values on the order of 30. Unfortunately, to prevent direct feedback from the reflective surfaces to the gain region, the etalon must be tilted. This in turn induces a "walk off" degradation of the finesse, thereby limiting the extent to which the etalon spacing can be increased for a given beam size. For an etalon spacing of 10 mm the incident beam diameter must be expanded to 10 mm in order to maintain a finesse of 25. Since the pumped diameter of the oscillator cell is approximately 0.5 mm, a 20x beam expanding telescope must be provided. An etalon with a spacing of 10 mm has a FSR of 15 GHz and provides a spectral width of 600 MHz for this finesse, i.e. ~ 0.001 nm at 480 nm. For comparison, Fig. 17 shows the etalon passband and the c/2L cavity mode spacing for the 50 cm long oscillator design. For dye lasers of this configuration, mode pulling ensures alignment of the cavity mode and the etalon passband. Therefore, cavity length tuning is not required.

To ensure that the oscillator does not operate with a multiplicity of etalon modes separated by the etalon FSR, the spectral selectivity of the grating must be greater than the FSR. Referring to Fig. 24, it is clear from the position of wavelength control of the grating, that an optimum grating resolution would be greater than, but not less than, twice the etalon FSR.

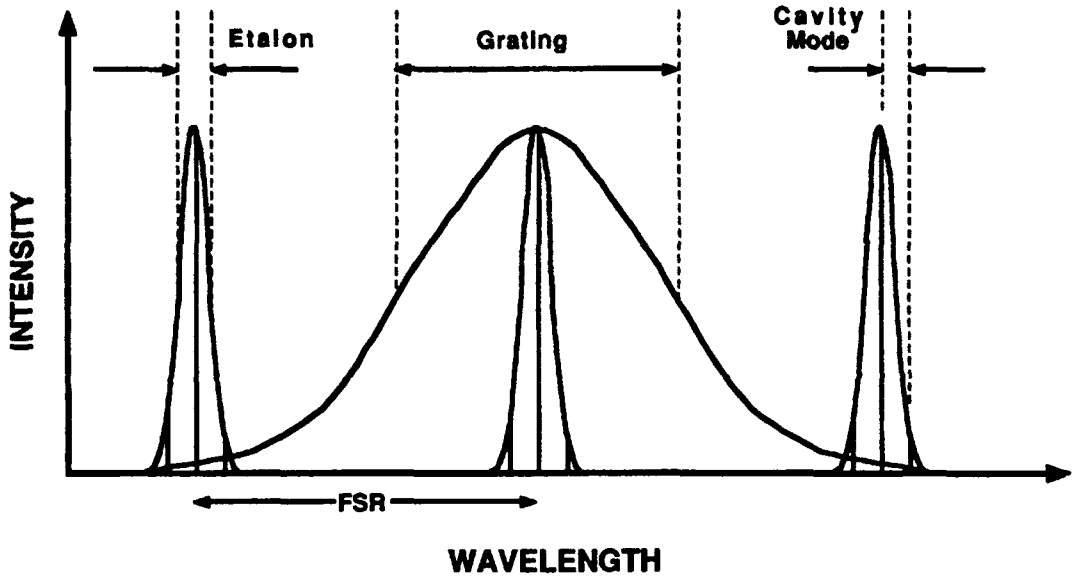

Figure 24. Comparison of the etalon passband and the c/2L cavity mode spacing for an oscillator length of 50 cm.

89-10-16-12

4.3.2 Diffraction Grating Requirements

The generalized equation describing diffraction of a ruled grating is given by,

$$d\ (\mathrm{Sin}\theta_m - \mathrm{Sin}\theta_i) = m\lambda\ , \tag{4}$$

where d is the rule spacing, m is the order number and θ_i, θ_m are the incident and diffracted angles, respectively. For maximum efficiency, and in order to avoid difficulty with higher orders satisfying the Littrow configuration, we impose the condition $d < \lambda$ to ensure solutions for only the first order. A 2400 l/mm grating satisfies this equation for wavelengths greater than 416 nm. By rotating the grating and increasing θ_i, the length of the grating illuminated, L, is increased. As L increases, the limit of angular resolution of the grating increases by,

$$\Delta\theta_{min} = \frac{\lambda}{L\cos\theta_m}\ . \tag{5}$$

Differentiating Eq. 4 with respect to λ, yields the grating dispersion,

$$DISP_g = \frac{d\theta}{d\lambda} = \frac{m}{d\ \cos\ \theta_m}\ . \tag{6}$$

After combination with Eq. 5 there results,

$$\Delta\theta_{min} = \frac{\Delta\ \lambda_{min} m}{d\ \cos\ \theta_m}\ . \tag{7}$$

Combining Eqs. 5 & 7 provides the resolving power of the grating,

$$\frac{\lambda}{\Delta\lambda_{min}} = mN\ , \tag{8}$$

where N is the total number of illuminated rulings. For a specific L value, these equations then yield self-consistent values for θ_i, θ_m, $\Delta\theta_{min}$, $\Delta\lambda_{min}$ and $\Delta\nu_{min}$. For purposes of comparison, results are presented in Table III for various values of L.

TABLE III
GRATING TUNING PARAMETERS

L cm	θ_i	θ_m 470 nm	θ_m 490 nm	$\Delta\theta_{min}$ Radians	$\Delta\lambda_{min}$ nm	$\Delta\nu_{min}$ GHz
3	70.5°	11.9°	14.7°	1.66E-5	6.9E-3	8.6
4	75.5°	9.3°	12.1°	1.25E-5	5.2E-3	6.5
5	78.4°	8.6°	21.5°	1.00E-5	4.1E-3	5.2

The resolving power is actually twice the values indicated since the grating is used in a double pass configuration. Moreover, gain narrowing and multipass effects in the laser cavity narrow the linewidth even further. Therefore, the values listed in Table III should be considered a conservative limit. Nevertheless, using the limits on $\Delta\nu_{min}$ as defined in the discussion of the etalon, 3 cm of illuminated grating appears to be an optimum choice.

To take full advantage of the resolving limit of the grating, the acceptance angle of the gain region must be made comparable to $\Delta\theta_{min}$ multiplied by the magnification of the etalon telescope in conjunction with the effective magnification of tilting the grating. For the case where L = 3 cm the effective 60-fold magnification reduces the acceptance angle requirements to approximately 1 milliradian. Using the 0.5 mm pumped diameter of the dye cell as the aperture size, the aperture distance must be $2S_2 + S_1 = 50$ cm.

Finally, so as to complete the modification of the oscillator section with minimal effect on the rest of the system, a telescope of 1/4 magnification has been included. This reduces the 10 mm diameter, m = 0 output beam to the 2.5 mm necessary for efficient energy extraction from the amplifier.

4.3.3 Oscillator Control Strategy

Depending on the application, continuous absolute wavelength control maybe necessary. This amounts to angle tuning the etalon passband with an accuracy on the order of its finesse. Presumably this would be achieved with another galvanometer. If the mass of the etalon is kept to a minimum, total system PAF's on the order of 20He can be achieved with minimal change to the existing calibration and control strategy. Of some concern is the fact that we have assumed that the etalon passband does not

change. In fact, typical thermal drift coefficients for an etalon of the appropriate dimensions, using the lowest thermal expansion materials, is about 1 GHz/C°. Obviously, long term operation will require real-time tracking and recalibration of the galvo tuning mirror, or the etalon will have to be temperature controlled. In deference both to system simplicity and the investment in the existing control software, the latter approach appears the most attractive. Accordingly, thermal control of the etalon, to better than 1 C°, will be incorporated into the oscillator design.

From the discussion above, it is clear that the most critical item of the oscillator control will be the extent to which the grating and etalon passbands coincide. Obviously, the worst case scenario, depending upon the choice of FSR, will occur when the grating passband falls in the middle of an etalon FSR and no lasing or multiline lasing occurs. For all other cases in which lasing occurs, the results of passband mismatch will be a degradation of energy output. The amount of mismatch-induced amplitude modulation can be mitigated somewhat by further optimization of the grating linewidth and etalon FSR, as well as by saturation of the amplifiers. This can be achieved by decreasing θ_i, thus illuminating a smaller portion of the grating and broadening the linewidth defined by the grating. However, the grating spectral width must remain smaller than the etalon FSR to ensure single line operation.

For the optimum case where the grating passband and etalon FSR coincide, assuming an energy degradation limit of 50%, the tolerated angle error of the tuning mirror is one part in 1700. *Based on our experience with the existing UTRC wavelength agile dye laser, we know that this can be readily achieved.* However, the tuning *rate* will be less than that of the configuration used in the existing 'C-A' injection laser system. Since the galvanometer tuning rate is limited by the inertia of the mirror, we project that the increased mirror size will result in an order-of-magnitude reduction in the tuning rate to approximately 10-20 Hz. The actual rate may be somewhat larger, since for the redesigned system the deflection angles will be much smaller and the wavelength steps could be sequential rather than random.

4.4 Anticipated System Performance

An effort has been made to minimize the effect of the modified oscillator design on the rest of the existing laser system and its control software. Nonetheless, the redesigned narrow line oscillator will not be a simple one-for-one replacement of the existing oscillator. It should be pointed out that some optimization would be required to integrate the redesigned injection laser oscillator and amplifier. For example, the shorter oscillator cavity affects the cavity build-up time. Consequently the optical delay lines between the oscillator and amplifier will have to be shortened. In addition unknowns related to the use of a significantly higher pump energy and possible optical damage to critical components will have to be addressed. However, our experience with the present system allows us to make projections with some confidence concerning impact of the narrow line oscillator on overall system performance. These specifications are summarized in Table IV.

TABLE IV
PROJECTED PERFORMANCE OF AN INJECTION LASER
WITH IMPROVED COHERENCE PROPERTIES

Pump	100 mJ, 308 nm
Pulse Duration	15 ns
Lasing Medium	Coumarin 102
Bandwidth, Tuning Range	20 nm, 470–490 nm
Energy Oscillator Amplifier Variation	 .3 - .6 mJ (wings, peak) 5 - 8 mJ (wings, peak) < = 20 - 30%
Wavelength Agility Maximum PRF Number of Addressable Wavelengths	 20 Hz ~20,000
Spectral Width	< 0.001 nm, < 1 GHz
Coherence Length	~25 cm
Beam Quality	Three x diffraction limit
ASE	< 5%

5.0 INJECTION LASER BASED ON AN OPTICAL PARAMETRIC OSCILLAOR

5.1 Introduction

Although the dye laser system described in Sections 2.0 and 3.0 provided a very convenient, low risk approach for wavelength agile control of the Rice XeF(C-A) amplifier, a dye laser would not be suitable for many SDI/DoD applications. Thus, as part of our research, other wavelength agile injection lasers were considered and evaluated as possible candidates for advanced XeF(C-A) laser systems.

The appearance in 1985 of large, high optical quality, damage resistant, strongly nonlinear, birefringent crystals of *beta-barium borate* (BBO) made possible for the first time the development of an efficient optical parametric oscillator (OPO) suitable for tunable narrow-band sources in the visible region of the spectrum. **This section describes a preliminary conceptual design for an advanced concept for the injection source based on an OPO using BBO.**

5.2 Baseline Requirements

Let us begin by briefly noting that the goal of the Rice-UTRC laser scale-up program was to develop a XeF(C-A) laser having the following properties: ~ 1 J/pulse, 20 ns pulsewidth, ~ 1 Hz pulse repetition frequency (PRF), continuously and randomly tunable in the blue-green region (450 - 510 nm). The baseline laser concept consists of a master-oscillator (MO) for injection control, and a XeF(C-A) power-amplifier (PA) configuration. The baseline MO (developed at UTRC and described in Section 2) is a modified Lamda-Physik dye laser in which an oscillator and preamplifier dye-cell are both pumped by a common XeCl excimer laser. The optical chain has been modified to permit high-speed, agile, random access to wavelengths within the gain bandwidth of the dye. The properties of the injection laser are set by the following amplifier input requirements: (1) power density, or intensity, 1 - 10 MW/cm^2; pulse duration, 10 - 20 ns; mirror injection hole diameter, 1.5 mm. These will be adopted as the requirements for the advanced injection source. In addition, there are always requirements on spectral quality of the input beam, depending on the application. For the purposes of the present BBO/OPO evaluation, the spectral requirement will assumed to be 0.001 nm in the blue-green region of the spectrum.

5.3 Optical Parametric Oscillator Using Beta Barium Borate

The earliest literature reports on nonlinear wavelength conversion with BBO (Refs. 16–19) led us to consider the possible use of an OPO/BBO tunable source to replace the dye laser MO in the baseline injection laser design. The OPO would require its own UV pump source, which could be an excimer laser (Fig. 25) as used in the existing wavelength-agile dye laser . The coherent UV 'pump' beam passing through the BBO crystal is converted into two new beams: a 'signal' beam at one wavelength and an 'idler' beam at another (Fig. 26). The signal beam is then tuned to the wavelength of interest (in the blue-green) by rotating the crystal. The idler beam occurs elsewhere in the spectrum and is not used. The OPO/BBO device is similar to a laser, except for the importance of three beams. Figure 26 illustrates a singly resonant oscillator (SRO) in which the optical cavity is resonant only for the signal beam.

The advantages of BBO (Refs. 17, 20) are: (1) wide optical transparency range (190 - 2600 nm); (2) wide phase-matching wavelength band (overlaps transparency range); (3) large nonlinear coefficient (d_{11} = 4.1 d_{36}(KDP)) (4) high damage threshold (5 GW/cm^2 for 10-ns pulses at 1064 nm); (5) large birefringence and relatively low dispersion; (6) low thermal birefringence coefficients; (7) high optical homogeneity (n = 1 x 10^{-6}); (8) chemical stability; (9) high melting point (1095 C); (10) high fracture temperature; (11) good hardness, Mohs = 4); and (12), usefully large sizes (20 mm inclusion-free cubes commercially available in 1989). Three disadvantages have been noted (Ref. 17): (1) absorption edge at 190 nm (which is not a problem for the present application); (2) small angular acceptance (< 1 mrad-cm) implying the need for diffraction-limited pump beams; and (3), small Z-component of second harmonic generation (SHG) coefficients (also not a problem here).

An OPO/BBO device would be small and rugged and so, for certain applications, an OPO tunable source should represent an improvement in compactness, simplicity, and reliability over the baseline dye laser MO. However, an even greater degree of compactness may be possible if the OPO/BBO subsystem can be 'self-pumped' by way of integration with the power amplifier itself (Fig. 25). **Self-pumping or self-injection may be possible since the XeF gain medium is capable of strong UV emission on the B–X transition of either XeF (351nm, 355 nm) or KrF (248 nm), and the gain medium can be tailored to provide efficient oscillation on both the XeF C–A and B–X transitions**

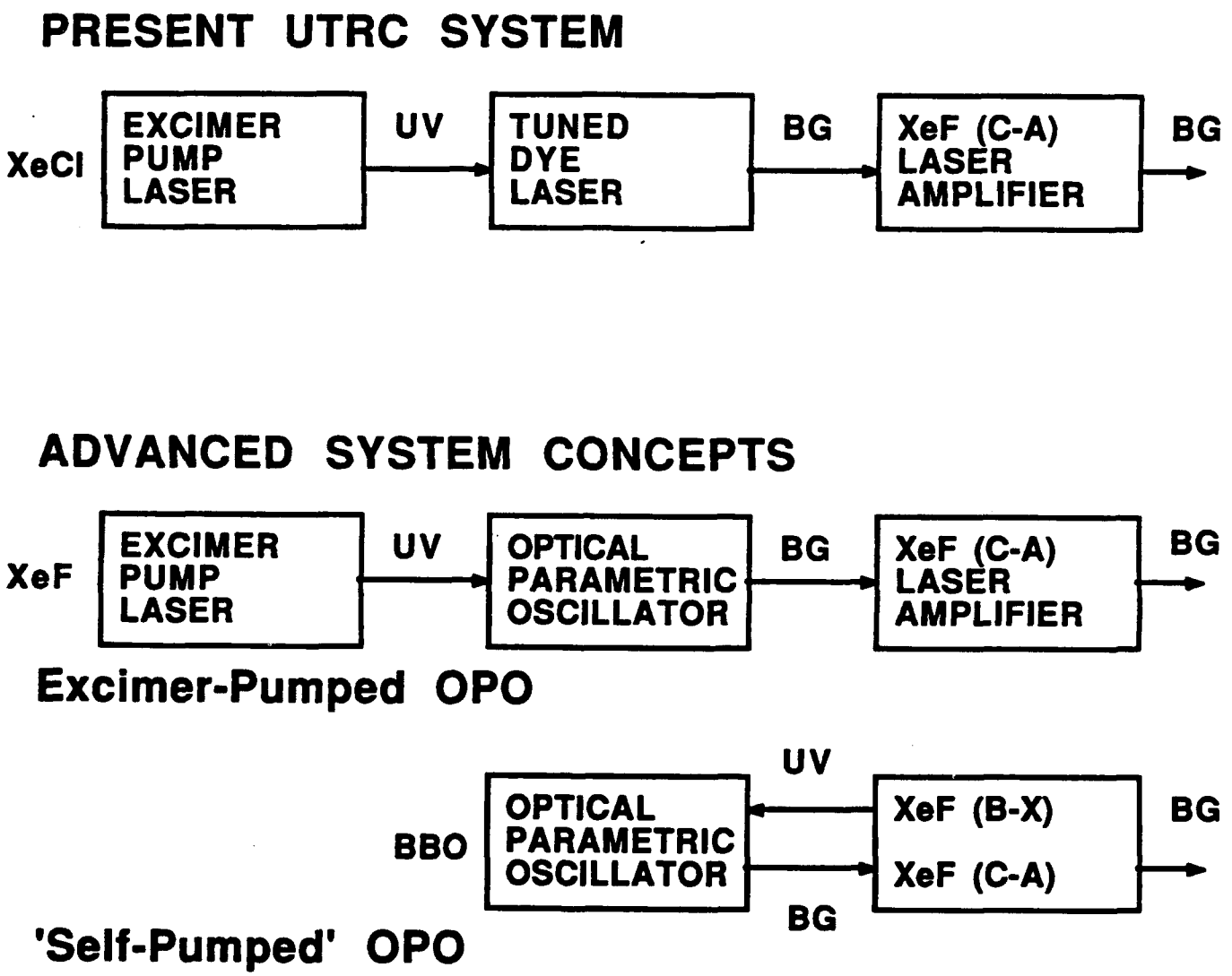

Figure 25. Illustration of the basic elements of the existing UTRC excimer pumped wavelength agile dye laser. Two advanced, second generation concepts are also shown: one in which the dye laser is replaced with an OPO; and another in which the tunable OPO is pumped by UV radiation emanating from the same active volume in which the XeF (C - A) laser is produced, i.e., 'self-pumping' of the OPO.

90-8-38-7

3 COAXIALLY PROPAGATING WAVES

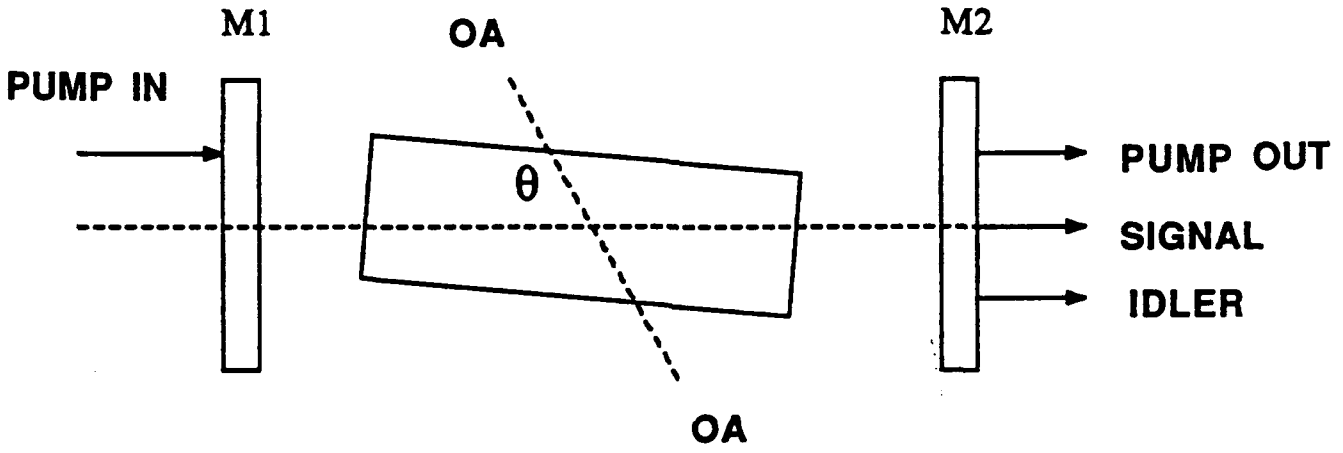

Mirrors M1 & M2: Transparent at pump and idler; Reflecting at signal.

Figure 26. Singly Resonant Oscillator (SRO).

90-8-38-8

(Refs. 9, 21). Thus, it is possible to envision an XeF device in which: (1) part of the XeF gain medium is allowed to lase in the UV; (2) the UV output is used as the pump beam for the OPO; and (3) the signal beam from the OPO is fed back (or 'self injected') into the amplifier formed by the remainder of the XeF gain medium to produce the high-energy blue-green output. This advanced concept will be referred to herein as the 'self-injection' concept (Fig. 27). It should be pointed out that although the schematic illustration of Fig. 27 shows separate UV and blue-green optical regions within the active pumped volume, efficient XeF B-X and C-A laser oscillation has been demonstrated for a dual optical design such that the UV and blue-green optical volumes were the same (Refs. 9, 21).

5.4 Analysis of the OPO/BBO

5.4.1 Tuning Curves

Optical parametric ampification (OPA) converts a fraction of the pump laser beam at wavelength λ_p into two other beams: the signal beam at wavelength λ and the idler beam at wavelength λ . However, this conversion requires that the three beams propagate colinearly, and that two colinear phase-matching conditions be satisfied. The two conditions are: $f_p = f_s + f_i$ and $n_p f_p = n_s f_s + n_i f_i$, (Ref. 22). The symbol f stands for the frequency, and λ for the vacuum wavelength of a monochromatic (single-frequency) beam, and these are related by the familiar relation $\lambda = c/f$ (where c is the speed light in vacuum). Also, n stands for the index of refraction, and the subscripts p,s,i always refer to the pump, signal, and idler beams respectively. In addition, S will be used for the local intensity of a beam.

The phase-matching relations are generally difficult to satisfy simultaneously, but in a birefringent crystal (like BBO) with sufficient difference between the ordinary (O-wave) and extraordinary (E-wave) indices, one can find an angle of propagation θ with respect to the optic axis (the OA), for which the relations can be satisfied for one signal frequency for a given pump. Thus, by rotating the crystal relative to the input pump beam, one can tune the output signal beam. (In our case, the required angular range is small, so that the crystal can be cut so that its faces are essentially normal to the input and output beams over the desired signal wavelength range). In general, the beams are mixed-wave, i.e., a mixture of O- and E-wave. Phase-matching can be achieved with three possible choices of polarization, grouped in two classes. In all cases, the pump beam is a mixed-wave. In the

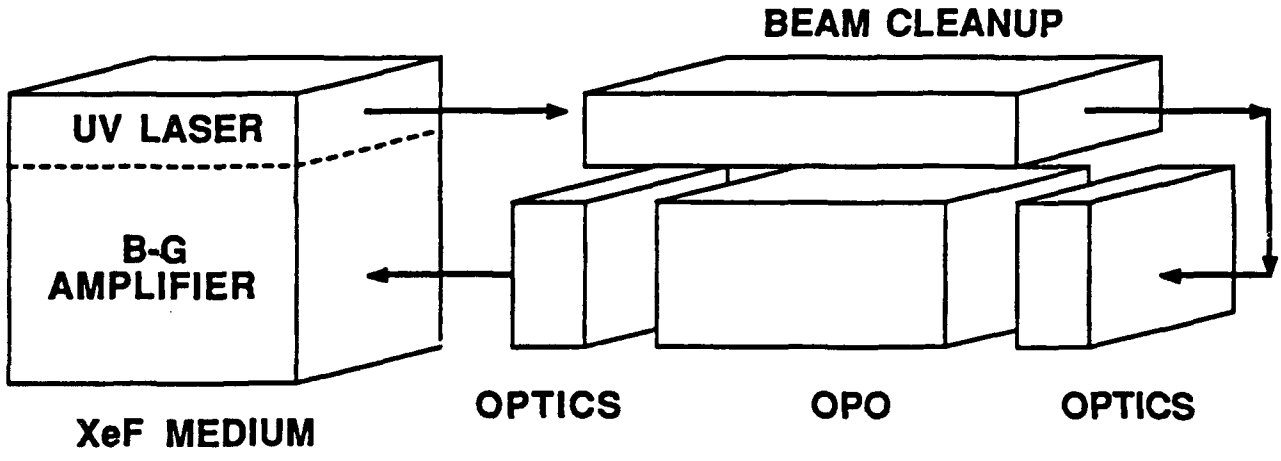

Figure 27. Conceptual illustration of the elements a 'self-pumped' XeF (C - A) laser design in which the OPO tuning element is pumped by UV from the XeF (B - X) laser transition excited in the same active volume as the blue-green 'C - A' laser transition.

90-8-38-9

so-called Type I phase-matching, both the signal and idler beam are O-wave. In Type II, the signal can be O-wave and the idler mixed-wave (Type II-A); or the signal can be mixed-wave and the idler O-wave (Type II-B).

Figure 28 shows the three tuning curves for the 351 and/or 353 nm wavelength of the XeF(B-X) transition. (The two sets of curves are indistinguishable on the scale employed.) Data for the O- and E-wave refractive indices were taken from Ref. 17. The index n for a mixed-wave is a solution of the equation

$$n^{-2} = \cos^2(\theta)\, n_O^{-2} + \sin^2(\theta)\, N_E^{-2}$$

at each wavelength. Only the signal range between 400 and 600 nm is shown. The slopes of the tuning curves determine how selective the tuning will be, and also how narrow the signal linewidth will be (without additional measures taken to narrow it). A steeper slope means that a larger range of signals will be generated at a fixed tuning angle. From this qualitative point of view, Type II-B phase-matching should be somewhat better for tuning than the others, other things being equal, but Type I is adequate.

Figure 29 is a similar plot for the 248 nm wavelength of the KrF(B-X) transition, which has also demonstrated strong laser oscillation in XeF(C-A) laser media (Ref. 9). The steepness of the slope for Type I suggests that the 248 nm pump is inappropriate for an application requiring a blue-green wavelength because tuning would be difficult, and the linewidth would be very large. Furthermore, Types II-A and II-B cannot access the blue-green region at all.

5.4.2 Finite Beams

In contrast to plane-wave beams, finite-diameter beams will eventually separate because of birefringence (which gives rise to the term 'beam walkoff') even though they start travelling together and satisfy the colinear phase conditions. The walkoff length depends on a walkoff angle and the beam diameters. As the beams separate, the conversion efficiency goes to zero. For Gaussian-profile beams, there are analytical solutions. Consider a circularly symmetric beam whose radial intensity profile is given by

$$S = S_o \exp(-2r^2/w^2),$$

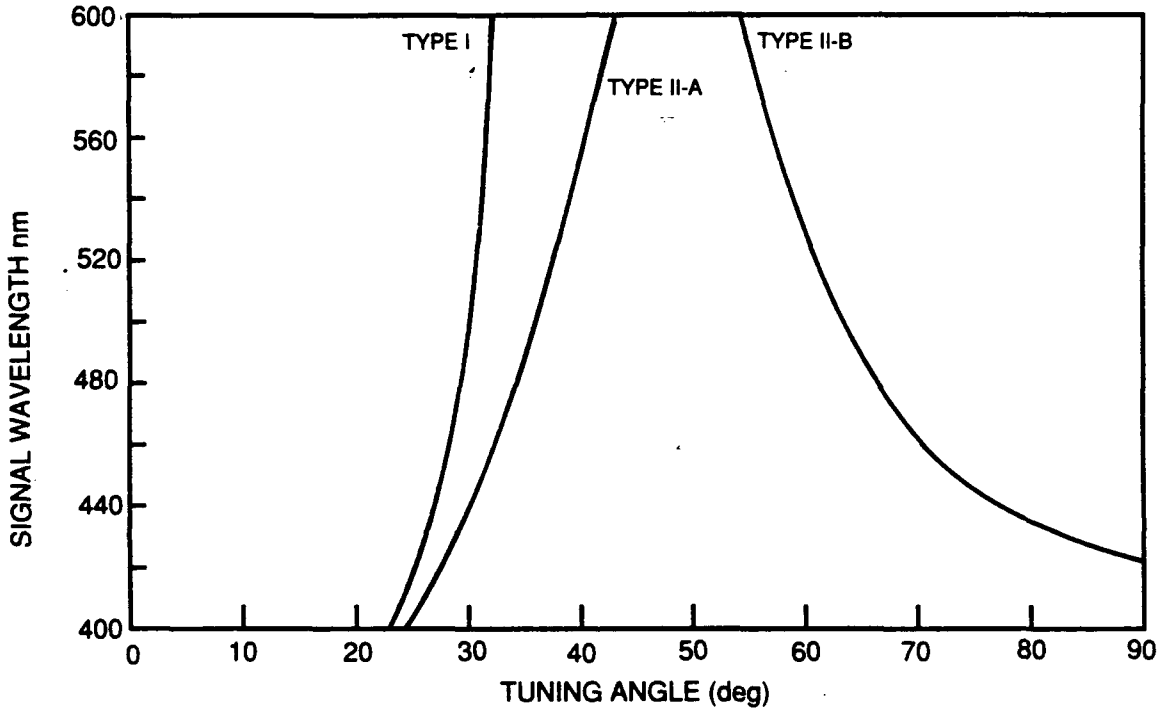

Figure 28. 331/353 nm tuning curve for BBO/OPO.

90-8-38-10

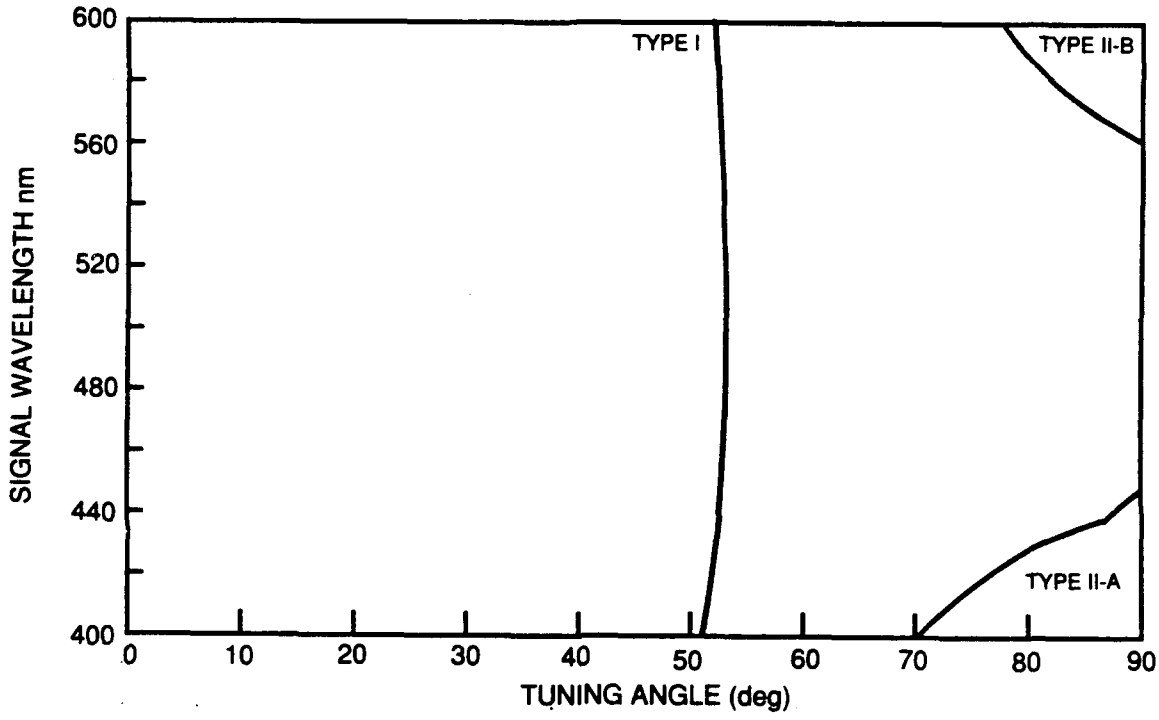

Figure 29. 248 nm tuning curve for BBO/OPO.

90-8-38-11

which also defines the beamwidth parameter w. Then, the effective area A of the beam, effective diameter D, and power P are given by

$$A = \pi w^2 , D = 2w, \text{ and } P = SA.$$

If $(S_p)_{th}$ is the threshold intensity for OPA, then for the condition of 'loose focusing' (near field, minimal beam spreading) the threshold pump power depends on the beam areas of pump and signal beams (A_p and A_s):

$$(P_p)_{th} = (A_p + A_s)(S_p)_{th}.$$

Also, because of beam walkoff there is an effective OPA conversion length L_{eff}. For typical conditions, with either a 351 or 353 nm pump beam of diameter about 2 mm, and Type I phase-matching, the walkoff length is about 13 mm, and the effective length about 10 mm. The crystal length L need be no longer than the walkoff length.

If the finite beam is also a finite pulse, as in our case, then the conversion efficiency will vary during the pulse and there will be an effective pulse width. We have calculated how the effective pulse-width for a Gaussian time profile varies with the height of the peak pulse intensity above threshold.

5.4.3 Non-Linear Coefficients

The effective non-linear coefficient d_{eff} for the OPO process is also a function of polarization, and so is different for Type I and Type II. The space group for BBO is believed (Ref. IV-2) to be R3C, for which there are three non-linear parameters, d_{11},d_{31}, and d_{33}, but only the first two contribute, and the second is much smaller than the first. The accepted value for d_{11} is 4.1 x d_{36}(KDP), where d_{36} = 0.63×10^{-12} m/V. Thus, $d_{11} = 2.6 \times 10^{-12}$ m/V. (The SU/UH experiments concluded that a coefficient of 5.1, in place of 4.1, would explain the higher than predicted conversion efficiency).

Type I: $d_{eff} = d_{11} \cos(\theta) \cos(3\phi)$

Type II: $d_{eff} = d_{11} \cos(2\theta) \sin(3\phi)$

The angles θ, ϕ are spherical polar coordinate angles: θ is the propagation angle (introduced above) with respect to the OA (the polar axis, which is the c-axis of the crystal); ϕ is the angle measured around the polar axis with respect to the a-axis of the crystal. For Type I phase-matching, the crystal will be cut so that $\phi = 0°$.

For example, for Type I phase-matching, $\lambda_p = 351$ nm and $\lambda_s = 500$ nm imply that $\lambda_i = 1178$ nm, $n_p = 1.6700$, $n_s = 1.6774$, $n_i = 1.6526$, $\theta = 30.73°$, and $d_{eff} = 2.22 \times 10^{-12}$.

5.4.4 Optical Parametric Gain

For a CW plane-wave (infinite beam) pump, the signal and idler beams are also CW and plane-wave, and the gain experienced by the signal depends only on the pump intensity $Sp(W/cm^2)$ and a material constant K:

$$K = 8\pi(d_{eff})2/\epsilon_o c n_p n_s n_i \lambda_s \lambda_i$$

The pumped non-linear crystal acts like a medium with gain for energy at the signal wavelength, i.e., it acts like a laser medium. The initial signal originates in noise (but it could also be injected). For the pump propagating through the crystal in the z-direction, from the input face ($z = 0$) to any distance z, the signal growth is given by the formula

$$S_s(z) = S_s(0) \cosh^2 (G_o z)$$

in which the second factor on the right (which will be referred to as the gain factor, GF) depends on the gain parameter G_o which is given by the relation

$$G_o^2 = \pi K S_p$$

These last two formulas depend on the assumption that the pump is not attenuated, nor depleted by conversion to signal and idler, as it passes through the crystal. It also assumes perfect phase-matching. A small amount of phase mismatch gives rise to the signal linewidth (see below for more details).

For the same typical parameters as above,

$$G_o^2 = 0.0537\, S_p.$$

If the pump intensity Sp is given in units of MW/cm^2, G_o will have the units of inverse cm. For the three values S_p = 1, 10, 100 MW/cm^2, G_o takes on the values 0.23, 0.73, 2.32 /cm. Then, for an effective conversion length of $z = L_{eff} = 1$ cm, the gain factor takes on the values 1.055, 1.64, 26.3 respectively. One can see that the non-linear gain grows quite rapidly for pump intensities in excess of 10 MW/cm2.

5.4.5 Optical Parametric Oscillation

The optical parametric amplifier can be converted to an optical parametric oscillator, which has many of the features of a laser, by enclosing the crystal between partially reflecting mirrors forming an optical cavity. The 'lasing' action of this device now depends on the losses of the cavity as well as the gain in the crystal, and there will be a threshold pump power $(P_p)_{th}$ for this device defined by the condition that the net round-trip gain equal the net round-trip loss. Since there are three inter-related wavelengths active in this device, there are new options for optimizing the resonances of the optical cavity. The easiest option to implement is to make the cavity resonant for the signal and not resonant for the pump and idler. This is the case that will be assumed.

Theoretical calculations for plane-wave beams gives the actual fraction of power in the pump which is converted to signal plus idler energy. A very convenient way to express the internal conversion efficiency ηint is in terms of the threshold power, but it is necessary to introduce an additional parameter $B = \beta L$ (the meaning of β is not important for this discussion, but becomes important when phase-mismatch is considered). For perfect phase-matching,

$$\eta_{int} = \sin^2(B)$$

with B given as a solution of the equation

$$\sin^2(B)/B^2 = (P_p)_{th}/P_p.$$

For example, if the pump power is 10 times the threshold value (which is a value reached in the SU/UH experiment), then B = 2.3186, and the internal conversion efficiency is about 53.8%. The fraction of the converted power which is signal is given by the ratio of signal to pump frequencies (or pump to signal wavelengths, namely 351/500 = 0.702). Thus, this simple theory predicts that approximately 38% of the pump power could be converted to signal power (and another 16% to idler simultaneously). The maximum conversion efficiency observed in the SU/UH experiment was 13% for signal (24% total). For a pulse, the average conversion efficiency over the pulse duration will be less than at the peak, and has been calculated by us, too.

5.4.6 Signal Linewidth

There is signal gain even when the colinear phase condition is not satisfied. In that case, the gain factor becomes

$$GF = 1 + (G_o/G)^2 \sinh^2(Gz)$$

where the reduced gain parameter G is

$$G^2 = G_o^2 - (\Delta k)^2/2$$

and the phase mismatch parameter is

$$\Delta k = 2\lambda(n_p f_p - n_s f_s - n_i f_i).$$

For the highest gain example used above, these formulas predict a signal linewidth around 1 nm, but this is the linewidth for optical parametric gain only. In the OPO there will be linewidth narrowing as in any laser.

5.5 The Stanford/Hannover Experiments

The recent experiment carried out as part of a Stanford University/University of Hannover (SU/UH) collaboration (Refs. 19, 23) is of immediate interest to the present analysis because the pump wavelength was 355 nm, very close to the XeF (B–X) transitions at 351 and 353 nm. The key physical

parameters of the OPO are weakly dependent on pump wavelength, so that the SU/UH experimental results are particularly relevant to the XeF *self-injection* laser concept with virtually no extrapolation required. The following is a description of the pertinent details of the SU/UH experiment (see Fig. 30). Also included below are interpretative comments concerning the relevance of these results to the present XeF(C-A) laser application. The more detailed scaling discussion appears in the next subsection.

5.5.1 The Pump

The 355 nm pump was obtained by non-linear tripling of the frequency of the primary pump source, a Q-switched 1064 nm unstable-resonator Nd:YAG laser. The Nd:YAG laser was injection-seeded to obtain a single axial mode 355 nm pulse, and the donut-shaped output beam was propagated and spatially filtered to achieve an approximately Gaussian beam profile. The typical pump pulse had an energy E = 30 mJ, an approximately Gaussian pulse shape of FWHM pulsewidth T = 6 ns, and a $1/e^2$ beamwidth diameter d = 2.5 mm (beam area = A = $d^2/4$). Thus, a rough estimate of the the average pump intensity is S_{av} = E/A = 100 MW/cm^2, but the peak intensity is S_{pk} = 2.355 S_{av} = 240 MW/cm^2. The pump laser could be operated at a 30 Hz pulse repetition frequency (PRF), and the pump beam could be attenuated to study the onset of OPO action. The damage threshold for BBO was quoted at 5 GW/cm^2; therefore, pump pulses of still higher intensity should be usable in BBO.

5.5.2 The OPO

The OPO consisted of an L = 12 mm long, 6 mm x 6 mm, BBO crystal set within a cavity composed of two flat mirrors parallel to one another and spaced 3 cm apart. There were two BBO crystals available, cut at 25 and 35 deg with respect to the optic axis, but it was concluded that only one crystal would be required to obtain angle tuning over the full wavelength range. The crystal surfaces were uncoated, and had Fresnel reflection losses of about 5% per surface. Three sets of mirrors were used. The input mirrors were 98% reflecting at the OPO signal wavelength and 80% transmitting at the pump and idler wavelengths. The output mirrors were 80% reflecting to the signal and more than 80% transmitting to the idler and pump. Consequently, the OPO was singly resonant (resonant for the

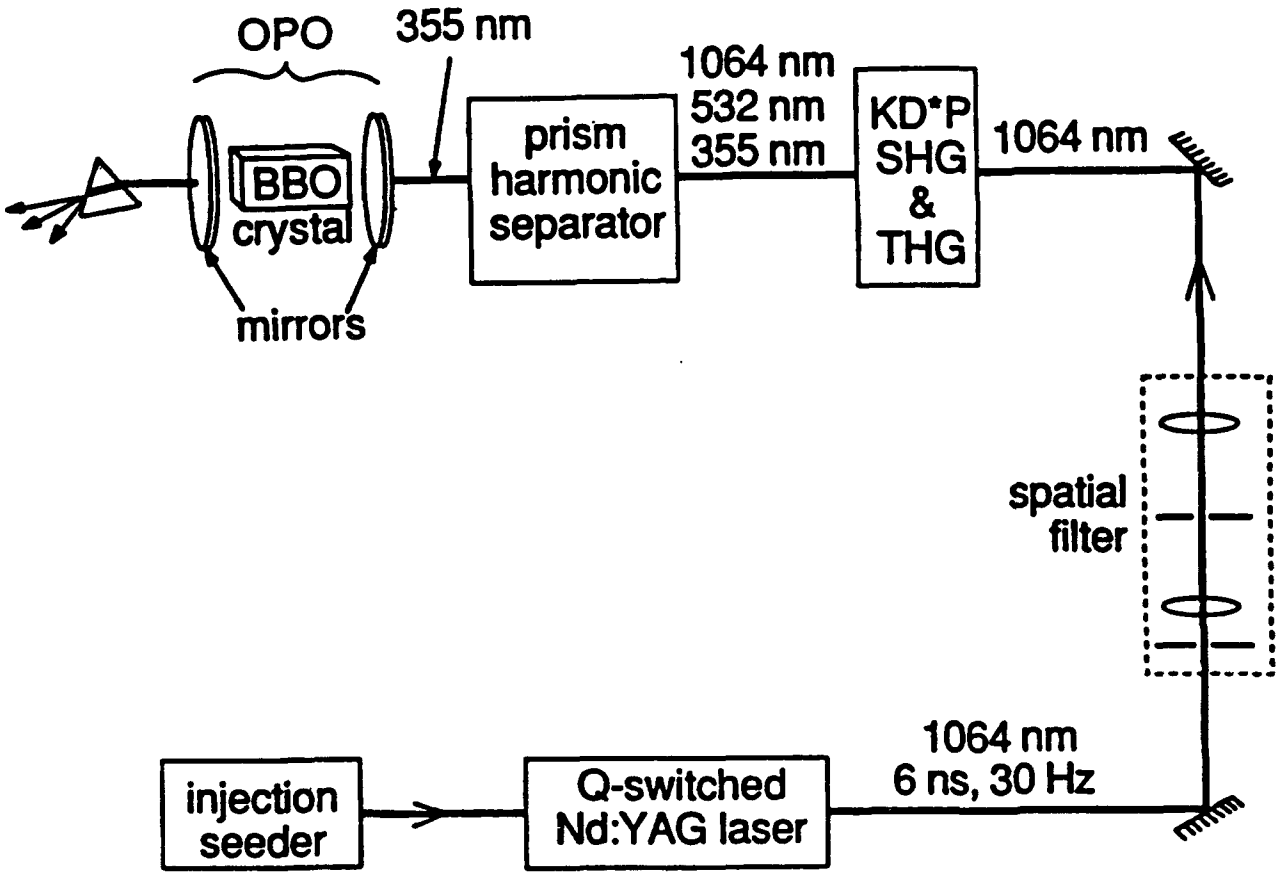

Figure 30. Schematic illustration of the Stanford/Hannover experiment.

90-8-38-12

signal only). The signal could be tuned from 412 nm (in the blue) to 710 nm (the degeneracy point), while the idler varied from 710 nm to 2550 nm (2.55 um). The limiting wavelength was set by the rapidly increasing absorption in the BBO crystal (0.5/cm at 2.55 um).

Interpretation: The blue-green wavelength range of interest (450 to 510 nm) is comfortably within the operating range of the SU/UH system.

5.5.3 Threshold and Efficiency

The threshold pump energy varied from 2 - 5 mJ over the tuning range. For a Gaussian-like beam, or a Gaussian-like pulse, or for a combination of these, threshold occurs when the peak intensity reaches the threshold intensity. The intensity threshold was reported to vary from 12 - 36 MW/cm^2 over the tuning range. A specific case was given: at 675 nm (signal wavelength) the threshold intensity was 20 MW/cm^2 (we estimate the corresponding threshold pump energy to be 2.7 mJ). At 30 mJ pump energy, the input intensity would have been over 10 times threshold, so that the maximum efficiency for frequency conversion would be very high. The conversion efficiency is highest at the peak intensity and decreases away from the peak. Since the intensity falls off both spatially (away from the center of the beam) and temporally (away from the center of the pulse), the output beam may be expected to be effectively both smaller and of shorter duration.

The authors reported that 13% of the input energy was converted to signal, and 11% to idler, for a total energy conversion of 24%.

5.5.4 The Signal

The maximum signal output reported for this experiment was 4.7 mJ/pulse, or 140 mW at 30 Hz PRF, at 560 nm. This was achieved with 36 mJ pump pulses. The output pulse width (or duration) was 2.4 ns (which is less than the 6 ns input because, as noted above, the conversion efficiency varies with intensity); and the beam divergence was 2.0 mrad (which is about 4 - 5 times diffraction-limited). It was not reported in the published material if the conversion efficiency was 13% at 560 nm also, but it could not have been much less.

The beamwidth of the signal was not reported. Scaling arguments (see subsection 4.6.1) suggest that the signal beam was about 20% wider than the pump beam, or 3.0 mm versus 2.5 mm for the

pump. Hence, using the same definition of average intensity, S_{av} = 28 MW/cm^2 for the signal versus 100 MW/cm^2 for the pump. This is more than adequate to meet the PA input requirement. Only the input pulse requirement (20 ns) is not met in the SU/UH experiment. As discussed further in subsection 5.6.1, the pump intensity cannot be reduced if the conversion efficiency is to be maintained.

Interpretation: Longer pulses with more energy are required for the present XeF(C-A) laser application, but the intensity requirement is essentially satisfied already in the SU/UH experiment.

5.5.5 Seeding the Pump

Efficient operation of the OPO required control over the axial modes (angular divergence) and longitudinal modes (frequency spread) of the pump laser and of the OPO. Efficient operation also implies a reduction in the energy (or 'amplitude') fluctuations of the output pulses. When the Nd:YAG source laser was allowed to run with many axial modes (linewidth of 30 GHz), the output of the OPO had a very large spectral width (linewidth > 100 GHz, or 0.1 nm at 560 nm). But when the source laser was 'seeded' (i.e., controlled by injecting a weak single-mode control beam, presumably CW), the source laser had a much smaller linewidth (60 MHz), and the OPO output signal had a better linewidth too (23 GHz, or 0.024 nm). In addition, the peak-to-peak intensity fluctuations dropped from ± 30% to ± 10%. The OPO output still contained a few axial modes.

Interpretation: Mode control of the pump appears to be required to achieve high efficiency OPO conversion, and to reduce signal fluctuations. It appears to be straight-forward to get the signal linewidth below 0.1 nm, but not to get it below 0.01 nm. Additional methods of linewidth narrowing need to be explored.

5.5.6 Seeding the OPO

The SU/UH experiment also included a demonstration of seeding of the OPO itself simultaneously with seeding of the pump source. The OPO was seeded at the resonant signal wavelength with the available wavelength 532 nm (2nd harmonic of the Nd line), and at the nonresonant idler wavelength with the other available wavelength 1064 nm (the Nd line). In both cases the OPO operated more efficiently and in a single axial mode (linewidth < 3 GHz) at the injected

wavelength. Only a tiny amount of injected power was required (the equivalent of 25 μJ at 1064 nm) for this improvement.

Interpretation: The seeding of the OPO is only of academic interest now because there will generally not be available another tuned source with spectral quality better than the OPO source in question! However, this technique may become important in the future, because only small amounts of power (about 5 kW) are required to control the linewidth of a much larger power (about 5 MW), and because narrow-linewidth control sources are more likely to be developed at low power than at high power. For now, though, one should work towards improving the linewidth of the OPO by spectral filtering and better design.

5.6 Extension of the Stanford/Hannover Technology

5.6.1 Scaling Arguments

From the discussion in subsection 5.4.5, we see that the conversion efficiency of a singly resonant OPO depends primarily on the ratio of actual pump intensity to threshold pump intensity. The threshold intensity depends on material parameters and on the optical resonator quality. Assuming that the threshold has been made as low as possible, the maximum conversion efficiency depends on the maximum achievable intensity, while the average efficiency and signal pulse shape depends on the input pulse shape. Using the SU/HU results as a state-of-the-art baseline or reference case, the extrapolation of those results can be based on a single parameter SP, an intensity characteristic of the pump beam pulse — for example, its peak intensity. Apart from constants and shape-dependent factors, SP depends simply on three basic parameters: the pulse energy E, pulse beam diameter d (beamwidth), and pulse duration T (pulsewidth). Thus, we can extrapolate from the the SU/UH experiment by keeping the scaling parameter SP, which is defined by

$$SP = E/d^2T$$

constant at the value it has for the experiment for 13% conversion to signal:

$$SP(13\%) = (30\ mJ)/(2.5\ mm)^2(6\ ns) = 0.8\ mJ/mm^2\text{-}ns.$$

Table V shows the baseline case and two possible extrapolations, i.e., choice for E, d and t, which should give the same 13% conversion efficiency. Both use the same beam diameter as the SU/UH experiment. The extrapolated case (a) is chosen to have the same signal beam diameter (2.5 mm) as SU/UH and to increase the pump pulse duration to 24 to 48 ns. Case (b) is similar to (a) but with the pulse duration a factor of 8 greater.

TABLE V
SCALING OF THE PUMP BEAM
- SIGNAL CONVERSION EFFICIENCY CONSTANT AT 13% -

PARAMETER	SU/UH	INJECTION SOURCE	
		(a)	(b)
PUMP			
E (mJ)	30.0	120–240	960–1920
d (mm)	2.5	2.5	2.5
T (ns)	6.0	24–48	192–384
SIGNAL			
E (mJ)	4.7	~ 20–40	~ 150–300
T (ns)	2.5	~ 10–20	~ 100–200

In the SU/UH experiment, the signal pulsewidth (2.5 ns) is less than half of the pump pulsewidth (6 ns). This is because the conversion efficiency is such a steep function of intensity that the region of the pulse near the peak gets the maximum growth. We have calculated the change in the shape from a Gaussian pump pulse to the signal pulse and found that the signal pulse is roughly half as long as the pump pulse, depending on peak-to-threshold ratio, but is independent of the absolute pulsewidth. The latter is not true experimentally; in fact, the depleted pump pulse is not even symmetrical with respect to the pump pulse. The experimental ratio of pulsewidths is 6/2.5 = 2.4. However, we have simply used a factor of 2 to extrapolate to signal pulsewidths. The signal energy was taken to be the same fraction of pulse energy as in the SU/UH experiment.

Note that to get a signal pulsewidth in the range of 100 to 200 ns, the pump pulsewidth must be twice that, and the pump pulse energy must be between 1 and 2 J. This is a large fraction of the energy stored in the gain medium. No studies were done as part of this analysis to evaluate configurations

which could extract these large OPO pump energies and still maintain sufficient gain in the blue-green.

The extrapolated pump beamwidth was set equal to the SU/UH value (2.5 mm) because the performance of the OPO is sensitive to the collimation of the pump beam as it passes through the BBO crystal, and because the required length of crystal depends on beamwidth through the walkoff effect discussed in Subsection B. Reducing the beamwidth is a way to increase beam intensity, but it also increases the beam diffraction and angular spreading. In addition, the increase in pump energy from 30 mJ to 120–240 mJ (a factor of (4–8) reduces the margin of safety against crystal damage. We have assumed that the SU/UH experiment represents a carefully optimized tradeoff of beamwidth and crystal length in an effort to get to high efficiencies. (However, increasing beamwidth is an acceptable way to go provided one has the pump energy to keep the peak intensity at SU/UH levels.)

Finally, the system beamwidth requirement on the signal is 1.5 mm, which is set by the input aperture at the power amplifier. The signal beamwidth is not the same as the pump beamwidth and depends on the type of resonator configuration. The SU/UH reports do not present data on the signal beamwidth. Theoretically, for a singly resonant oscillator (SRO), the optimum focusing condition is known (in a special simplified case) to occur when the confocal parameters of signal and pump are equal: $b_s = b_p$. The confocal parameter is a relation between beam size, wavelength, and index of refraction with the dimensions of length:

$$b = 2\pi n w^2/\lambda.$$

The best choice for a narrow beamwidth in the crystal is achieved when b = L. The optimum focusing condition for the SRO implies that the signal beamwidth is about 20% larger than the pump beamwidth. Hence, the signal beam will be larger than the system requirement, which means that the optical transfer of the beam from OPO to PAQ input will need to include an afocal system to reduce the beamwidth from 2.5 to 1.5 mm. The change in beam area translates to an increase in intensity level in the beam by a factor of about 2.8, and provides a useful margin for the injected beam. It does not

translate to a reduction in the pump energy, since the pump intensity must be maintained at a high level for good conversion efficiency.

5.7 BPO/OPO: Summary and Discussion

Our study and evaluation of the SU/UH experiment shows that the basic technology is in place for a XeF(C-A) laser injection source based on an OPO/BBO device. It also shows that the present intensity levels are sufficient for controlling the (C-A) power amplifier. However, the pulse duration (pulsewidth) in the SU/UH experiment was not long enough to meet the energy extraction requirement for the (C-A) power amplifier. Increasing the pulse duration by at least a factor of 4 - 8, with a corresponding increase in pulse energy (to keep the intensity level the same as in the experiment), will be required.

The SU/UH experiment demonstrated significant energy conversion efficiencies in the blue-green region of the spectrum from a pump at a wavelength of 355 nm, very close to the XeF(B-X) pump wavelengths that would be used for the proposed 'self injection' concept. A diffraction-limited narrow-linewidth pump is required for high efficiency and also for narrowing of the signal linewidth below 0.1 nm. Single-mode longitudinal and transverse operation of the pump, achieved by seeding the pump laser by injection of a lower-power, high quality beam, was used by SU/UH to get to 0.025 nm Additional means will be required to narrow the linewidth to 0.01 nm and below.

Linewidth narrowing using a filter or grating either internal or external to the OPO cavity filter has not been considered in this study, but will be required to get to linewidths below 0.01 nm. The SU/UH experiment achieved 0.024 nm. A optical width of 0.01 is probably achievable by incremental improvements in the SU/UH design without the use of a filter or grating. Such an additional element will increase the losses in the device, and thereby create the need for greater gain. For optical parametric amplification, that usually means more peak pump power. The effect of increasing pump power on linewidth stability will need to be

The theory shows that the performance of an OPO/BBO device can be scaled through a single variable, namely, the peak pump intensity, which can be related to the pump pulse energy, beam

diameter, and pulsewidth. Scaling of the SU/UH shows that an increase in pulse energy is primarily required to meet the power amplifier input requirements.

Sufficient energy in the amplifier gain medium is available to generate the pump beam, but a separate study is needed to anticipate any problems that may need to be solved in producing a narrow-linewidth, diffraction-limited, high-power pump beam.

The calculation of the tuning curves shows directly that the option of a 248 nm pump is a poor choice for generating signals in the blue-green spectrum around 500 nm. Type II phase matching is impossible, and Type I phase matching is close to the degeneracy point at which the signal and idler wavelengths are equal. Near this point, the tuning curve is nearly vertical, meaning that tuning of the signal by angular rotation is expected to be difficult. The signal wavelength is especially sensitive to angle, and the linewidth will be broad because a relatively wide range of wavelengths is able to satisfy the phase-matching conditions. The tuning curves for 351/355 nm appear to be without any problems, and Type II may be better than Type I in that its tuning curve has the less sensitive slope.

We have not considered in detail the question of wavelength agility, i.e., how rapidly the crystal can be turned, or equivalently, how rapidly the beam angle through the crystal can be changed, in a random manner. However, it is easy to anticipate that wavelength scanning (i.e., continuous sweeps through the blue-green) will be easier to perform than random wavelength hopping.

6.0 SUMMARY AND DISCUSSION: XeF(C-A) LASER TECHNOLOGY & APPLICATION ISSUES

In May of 1987 the Rice-UTRC team embarked on an ambitious scaling demonstration of the XeF(C-A) laser. The primary goal of the program was demonstration of 1 J per pulse, wavelength-agile, repetitive operation of a robust XeF(C-A) laser system suitable for use at a government facility. This goal was met and all initial system performance objectives were either met or exceeded. Several key performance features of the XeF(C-A) laser amplifier at Rice are summarized in Table VI, while the features or the UTRC wavelength-agile dye laser injection source are summarized in Table VII. Currently, both systems are in operation at Rice University.

6.1 Short Pulse or Long Pulse

The Rice-UTRC program was focused entirely on excitation provide by an intense, high current density electron beam of short temporal duration (~ 10 ns, FWHM), characteristics very similar to those of a small scale experiment, the performance of which was the basis of the present scaling demonstration. During the course of this work efficient XeF(C-A) laser operation at the J/pulse level was demonstrated by the Avco group using a low current density electron beam having a temporal duration of approximately 1 microsec (Ref. 24). This development raised questions about which was the 'best' approach to e-b excitation of the XeF(C-A) laser—short pulse (< 100 ns) 'hard-pumping' or long pulse (~ 1 microsec) 'soft-pumping'. Before addressing a few of the issues impacted by this question, it should be pointed out that while *efficient*, high energy density XeF(C-A) laser operation has so far been limited to either very short or very long pulse operation, detailed kinetic modeling shows that excitation conditions resulting in laser pulses duration intermediate between these two extremes can be expected to result in similar performance.

6.1.1 Electron Beam Technology

Among the issues to be considered are the relative effects of hard and soft pumping on e-beam system components such as the foil, diode and power conditioning equipment. Accordingly, we asked Mawwell Laboratories, builder of the custom designed e-beam system used for the Rice 'C-A' amplifier, to assist in the evaluation of the relative complexity of scaling a short pulse (< 100 ns) high

TABLE VI
RICE/UTRC XeF (C - A) LASER PROGRAM

Key performance features of the Rice *scaled, wavelength-agile* amplifier

Excitation	**High current density e-beam, 10 ns FWHM,** *PRF 1 Hz*
Energy deposition	**60 Joules, 125 J/liter**
Active length, volume	**50 cm, 0.5 liters**
Operating mode	**Injection controlled regenerative amplifier**
Optical cavity	***Internal or external* unstable resonator, M ~ 2**
Wavelength, spectral width, max coherence length	**450 → 530 nm, < 0.005 nm, 0.25m**
Maximum laser energy, energy density, power	*1.2 J, 1.8 J/liter, ~ 0.1 GW*
Intrinsic efficiency	*1.5%*
Laser pulse duration	**10 ns FWHM**
Beam divergence	**150 μrad (3x DL)**

90-8-38-13

TABLE VII
RICE/UTRC XeF (C - A) LASER PROGRAM

Performance of the UTRC *wavelength agile* injection laser

Excitation configuration	**UV excimer-pumped dye laser system**
Excimer energy, pulse duration	**150 mJ @ 308 nm, 60 ns FWHM**
Bandwidth, wavelength range,	**30 nm, 465-495 nm (Courmarin 102)**
Max pulse energy and duration	**7.5 mJ @ 480 nm, 30 ns FWHM**
Tuning method	**holographic grating (2400 lines/mm) combined with a galvo-driven mirror**
Operating mode	*continuous, pulse-to-pulse tunability throughout the band; any arbitrary pre-selected wavelength sequence*
Control strategy	**computer controlled galvo tuning**
Maximum tuning speed	**50 Hz (limited by excimer pump PRF)**
Wavelength accuracy	**±0.008 nm**
Spectral width, coherence length	**0.01 nm, 2.5 cm**
Operational/design features	**menu driven IBM PC controlled; EMI shielded;** *industrial hardened electronics*

90-8-38-14

current density e-beam system as compared to a long pulse (> a few hundred nsec) system, both systems designed for 'C-A' lasers having the same energy output. **After consideration of many engineering issues, Maxwell concluded that "there are no known technology issues of significance differentiating short pulse and long pulse e-beam systems as regards scaling to the average power/energy levels required for SDI sensor applications. Accordingly, decisions concerning scaling of of the XeF(C-A) laser should be based on criteria other than the e-beam pulse duration and/or current density". On this basis we conclude that electron beam technology issues are of secondary performance insofar as comparison of long pulse and short pulse XeF(C-A) lasers is concerned.**

6.1.2 Broadband Tuning and Wavelength Purity

By far, the single most significant feature of the XeF(C-A) laser is its continuous, broadband tunability, which can cover a wavelength range > 50 nm centered at ~ 480 nm. The only practical way to capitalize on the broadband tunability of the 'C-A' laser is by using a laser injection to control the XeF(C-A) laser wavelength (Ref. 6). Indeed, development of the required injection laser technology was the primary thrust of the present contract.

Injection controlled tuning of the C-A laser has been demonstrated routinely with a spectral width of 0.001 nm, corresponding to a coherence length of ~ 0.25 m. As mentioned in Sections 3.0 and 4.0, certain SDI/DoD applications will require a tuned laser output with a coherence length of several meters, $\Delta\lambda \leq 0.0001$ nm. Experimental evidence shows that broadband tuning combined with the a high degree of spectral purity (coherence) and wavelength control are not likely to be attainable using a long pulse, low gain C-A laser. It is possible to control the wavelength of a long pulse laser exhibiting broadband gain; but only if the injection wavelength is very near the gain peak. Of course, that restriction severely compromises the main feature of the XeF(C-A) laser, i.e., broadband tunability. Injection controlled tuning of a broadband laser is known to be most effective if the gain is large and of short temporal duration (Ref. 6). **Thus, we conclude that as far as broadband tunability and highly coherent output are concerned, short pulse 'C-A' lasers have a distinct advantage over their long pulse counterparts.**

6.1.3 Amplifier - Oscillator Issues

Analysis of the requirements of SDI/DoD missions indicates that laser systems that use amplifiers are better suited for most applications than those that use oscillators. For example, in radar applications amplifiers are far more versatile than oscillators because amplifiers allow a multiplicity of radar formats to be used in measuring target parameters. Also, for applications requiring the tunability discussed above, wavelength control is best achieved by injecting an efficient amplifying medium. Since the gain of long pulse (~ 1 micro sec) 'C-A' lasers is up to 5-6 times lower than that of short pulse (~ 10-20 ns) lasers, and the absolute gain level of long pulse 'C-A' lasers in quite small (~ 0.5 %), short pulse 'C-A' lasers are better suited for applications requiring an amplifier configuration. Indeed, even relatively simple applications such as broadband target illumination are best addressed using amplifiers. **Since the low gain of very long pulse 'C-A' lasers would appear to preclude their use as amplifiers, lasers exhibiting higher gain (shorter pulse duration) have the advantage. However, modeling has shown that 'C-A' lasers of intermediate pulse duration (~ 100 nsec) exhibit gain levels (> 1 %/cm) that should be compatible with amplifier configurations.**

6.1.4 Application Requirements in General

Independent of the issues discussed above, certain applications place restrictions on the laser pulse duration that will be the over-riding issue. For example, spatial imaging using a laser radar may require a pulse length of a microsec, or more, while freezing speckle patterns in order to perform speckle imaging of non-rotating targets may require a pulse duration on the order of 10-20 ns. **Thus, it is clear that in many cases the application will determine whether an XeF(C-A) laser having a short, long or intermediate duration is required.** In that case, the problem is reduced to determining whether or not a 'C-A' laser can be designed having the required pulse length, while at the same time meeting the energy/power requirements of the application.

6.2 Tunable Gas Lasers vs Solid State

Solid state lasers such as Alexandrite exhibit broadband tuning comparable to that of the XeF(C-A) laser and are much better developed. Additionally, such solid state lasers are capable of high pulse energy. Since it is difficult to remove excess heat from a solid state laser, while heat removal from a gas laser by convection is straightforward, the key issue in the solid state vs gas laser debate is

average power. **Insofar as broadly tunable lasers such as Alexandrite and Ti-sapphire are concerned, they appear to be the systems of choice for average powers $\overline{<}$ 1 kW, while the XeF(C-A) laser would have a distinct advantage for applications requiring average power at the multi-kW level.**

6.2.1 Wavelength Criticality

The wavelengths of the XeF(C-A) laser (455 nm - 515 nm) and the solid state Alexandrite (700 nm - 800 nm) and Ti-sappire (700 nm - 1000 nm) lasers each are compatible with relatively good atmospheric transmission, an important issue for many SDI/DoD missions. **However, the wavelength of the XeF(C-A) laser is uniquely suited for transmission through sea water. Thus, for Naval applications requiring tunability and high energy/average power, the XeF (C-A) laser is the only candidate having demonstrated scaling potential.**

6.3 Electron-Beam vs Electric Discharge Excitation

Clearly there are laser applications requiring relatively low power/energy for which a blue-green wavelength combined with tunability would be advantageous. In that case electric discharge excitation has many advantages over electron beam excitation because of its relative simplicity and reliability. Moreover, as regards the potential for development of a discharge excited XeF(C-A) laser, the very successful and closely related UV rare gas halide lasers provide an excellent technology base.

However, the gain cross section for the XeF(C-A) laser transition is more than an order of magnitude smaller than that of the UV B-X transitions, meaning that achieving a practical 'C-A' gain requires a pump energy density much higher than is typical of discharge excited UV lasers. Additionally, for typical discharge conditions the gain of the competitive XeF(B-X) laser is very high, with the result that UV oscillation is difficult to suppress. Finally, it is very difficult to obtain stable self-sustained discharges using the gas mixtures kinetically optimized for the 'C-A' laser (Refs. 1, 21). To date, these issues have proven to be formidable obstacles to the demonstration of efficient discharge-excited XeF(C-A) laser operation. **While identification of conditions compatible with stable discharge operation, high 'C-A' gain (~ 1%/cm), and a controllable gain level on the XeF(B-X) transition, represents a considerable challenge, we see no fundamental reasons precluding the possibility.**

7.0 REFERENCES

1. Nighan, W. L., F. K. Tittel, W. L. Wilson, Jr., N. Nishida, Y. Zhu, and R. Sauerbrey, *Synthesis of rare-gas halide mixtures resulting in efficient Xef (C-A) laser oscillation*, Appl. Phys. Lett., Vol. 45, pp. 947-949, 1984.

2. Marowsky, G., N.Nishida, F.K.Tittel, W.L.Wilson, Y.Zhu, and W.L.Nighan, *Efficient narrow spectral output in the blue-green region from an injection-controlled electron beam pumped XeF(C-A) laser*, Appl. Phys. Lett., Vol.47, p. 657, 1985.

3. Henshaw, P. D., and D.E.B.Lees, *Electronically agile multiple aperture imager receiver*, Optical Engineering, Vol. 27, p. 793, 1988.

4. *Tunable Blue-Green Lidar Transmitter Demonstration*, ONR Contract N00014-86-K-0698. (Rice University).

5. *Tunable Blue-Green Lidar Transmitter Demonstration-Injection Laser Development*, ONR Contract N00014-87-C-0371. (UTRC).

6. Bigio, I. J., and M.Slatline, *Injection locking unstable resonator excimer lasers*, IEEE J. Quantum Electron., Vol. QE-19, p. 1426, 1983.

7. Hamada, N., R.Sauerbrey, W.L.Wilson, F.K.Tittel, and W.L.Nighan, *Performance characteristics of an injection-controlled electron beam pumped XeF(C-A) laser system*, IEEE J. Quantum Electron., Vol. 24, p.1571, 1988.

8. Hirst, G. J., C. B. Dane, W. L. Wilson, R. Sauerbrey, F. K. Tittel, and W. L. Nighan, *Scaling of an injection-controlled XeF (C-A) laser pumped by a repetitively pulsed, high current density electron beam*, Appl. Phys. Lett. Vol. 54, pp. 1851-1853, 1989.

9. Dane, C. B., G. J. Hirst, S. Yamaguchi, T. Hofmann, W. L. Wilson, R. Sauerbrey, F. K. Tittel, W. L. Nighan and M. C. Fowler, *Scaling Characteristics of the XeF(C-A) Excimer Laser*, IEEE J. Quantum Electron, Vol. 31, 1990.

10. Snyder, J. J., *Laser wavelength meters*, Laser Focus, Vol. 18, p. 55, 1982.

11. Reiser, C., and R.B.Lopert, *Laser wavemeter with solid Fizeau wedge interferometer*, Appl. Optics, Vol. 27, p. 3656, 1988.

12. Morris, M. B., T.J.McIlrath and J.J.Snyder, *Fizeau wavemeter for pulsed laser wavelength measurement*, Appl. Optics, Vol. 23, p. 3826, 1984.

13. The authors would like to express their appreciation to Dr. W. L. Nighan, Jr. of Princeton University for suggesting the use of diamond pinholes.

14. Chung, Y. C., and T.M.Shay, *Atomic resonance filters*, IEEE J. Quantum Electron., Vol. 24, p. 709, 1988.

15. Yamaguchi, S., T. Hoffman, C. B. Dane, R. Sauerbrey. W. L. Wilson, and F. K. Tittel, *Respectively pulsed operation of an injection controlled high power XeF(C–A) excimer laser,* Applied Physics Letters, 1990 (in press).

16. Chen, C. (Fujian Institute), and Y.X. Fan, R.C. Eckardt, R.L. Byer (Stanford): *Recent developments in barium borate*, Soc. Photo.-Opt. Instrum. Eng. (SPIE), Vol. 681 (Laser and Nonlinear Optical Materials), pp. 12–19 (1986)

17. Adhav, R.S., S.R. Adhav and J.M. Pelaprat: *BBO's nonlinear optical phase–matching properties*, Laser Focus/Electro–Optics, September 1987, pp. 88–100.

18. Komine, H.: *Optical parametric oscillation in a beta–barium borate crystal pumped by an XeCl excimer laser,* Opt. Lett., Vol. 13, pp. 643–645 (1988).

19. Fan, Y.X., R.C. Eckardt, R.L. Byer (Stanford) and J. Nolting, R. Wallenstein (Hannover): *Visible BaB_2O_4 optical parametric oscillator pumped at 355 nm by a single–axial–mode pulsed source*, Appl. Phys. Lett., Vol. 53, pp. 2014–2016 (1988).

20. Chen, C.: *Chinese lab grows new nonlinear optical borate materials*, Laser Focus World, pp. 129–137, November 1989.

21. Nighan, W. L., R. A. Sauerbrey, Y. Zhu, F. K. Tittel, and W. L. Wilson, Jr., *Kinetically tailored properties of electron–beam excited XeF(C–A) and XeF(B–X) laser media using an Ar–Kr buffer mixture*, IEEE J. Quantum Electron., Vol. QE-23, pp. 253–261, 1987.

22. Smith, R.G.: *Optical parametric oscillators*, in Lasers (Vol. 4), A.K. Levine and A.J. DeMaria, Eds. (Dekker, New York, 1976).

23. Nolting, J., R. Wallenstein, Y.X. Fan, R.C. Eckardt, and R.L. Byer: *High power BaB_2O_4 visible optical parametric oscillator pumped by single–axial–mode 355–nm pulses*, figures from a talk given at the EQEC'88 Conference at Hannover (September 15, 1988). Supplied courtesy of R.C. Eckardt.

24. Mandl, A. and L. H. Litzenberger, *Efficient, long pulse XeF(C–A) laser at moderate electron beam pump rate*, Appl. Phys. Lett., Vol. 53, pp. 1690–1692, 1989; OE/LASE '90, Los Angeles, California, January 1990.

8.0 REPRINTS OF PUBLISHED PAPERS

- *Wavelength-Agile Operation of an Injection-Controlled XeF(C-A) Laser System:* Th. Hofmann, S.Yamaguchi, C.B.Dane, W.L.Wilson, R.Sauerbrey, F.K. Tittel, R.A.Rubino and W.L.Nighan, Applied Physics Letters (in press).

- *Scaling Characteristics of the XeF(C-A) Laser:* C.B.Dane, G.J.Hirst, S. Yamaguchi, Th. Hofmann, W.L.Wilson, R.Sauerbrey, F.K.Tittel, W.L.Nighan and M.C.Fowler, IEEE Journal of Quantum Electronics, Vol. 26, pp.xxx, September 1990.

- *Kinetic Processes in Electron Beam Excited XeF(C-A) Laser Media:* W.L. Nighan and M.C.Fowler, IEEE Journal of Quantum Electronics, Vol. 25, pp. 791-802, April 1989.

Wavelength-Agile Operation of an Injection-Controlled XeF(C→A) Laser System

Th. Hofmann, S. Yamaguchi, C. B. Dane, W. L. Wilson,
R. Sauerbrey, and F. K. Tittel

Department of Electrical and Computer Engineering
Rice University
Houston, TX 77251-1892

R. A. Rubino, and W. L. Nighan

United Technologies Research Center
East Hartford, CT 06108

Abstract

The performance of a pulsed laser system consisting of an electron beam pumped XeF(C→A) amplifier which is injection-controlled by a wavelength-agile dye laser is reported. Random sequence tuning over a 27 nm spectral region, centered at 478.5 nm, with 1 Hz pulse repetition frequency was demonstrated. Laser output energies of 0.8 J with pulse durations of 10 ns were measured.

Wavelength-Agile Operation of an Injection-Controlled XeF(C→A) Laser System

Th. Hofmann, S. Yamaguchi, C. B. Dane, W. L. Wilson,
R. Sauerbrey, and F. K. Tittel

Department of Electrical and Computer Engineering
Rice University
Houston, TX 77251-1892

R. A. Rubino, and W. L. Nighan

United Technologies Research Center
East Hartford, CT 06108

Since its first demonstration more than a decade ago the electron beam pumped XeF(C→A) excimer laser has been developed into an efficient, scalable gas laser system[1,2,3,4]. It is continuously tunable between 450 and 530 nm[5], covering the entire blue-green region of the spectrum. Output energy densities exceeding 1.0 J/l have been obtained for wavelengths between 470 and 510 nm. A maximum laser energy of 1.2 J was observed at 487 nm, using a large, square aperture resonator[6]. Scaling studies indicate potential for even higher output energies[1,2,3].

A five component gas mixture, tailored through kinetic modeling[7], along with injection control by a pulsed dye laser enable the XeF(C→A) laser to achieve a high intrinsic efficiency of 1.3 %[2]. Optimization of the unstable resonator, guided by numerical modeling[8] contributed to the high energy extraction efficiency. Beam quality of better than three times the diffraction limit was demonstrated. Narrow linewidth output of 0.001 nm was achieved[5], limited only by the bandwidth of the injection laser. Recently a transverse flow system was developed, that permits pulse repetition frequencies of up to 1 Hz with no decrease in output energy[6].

For remote sensing, spectroscopic, and other applications it is desirable to combine the characteristic features, that have so far only been demonstrated separately, into one integrated laser system. In this letter we report for the first time the performance of a XeF(C→A) laser amplifier, controlled by a wavelength-agile dye laser[9]. Laser operation with high pulse energies at 1 Hz pulse repetition frequency (PRF), with shot-to-shot tunability over a wide bandwidth is described.

Figure 1 shows a schematic of the integrated wavelength-agile, high energy laser system. The injection beam travels first through a delay line which optically isolates the dye injection laser from the XeF(C→A) laser amplifier. After collimation by a telescope of magnification M=5, the dye laser beam enters the amplifier resonator through an injection hole and is subsequently amplified and expanded in the excimer cell. The delay time between triggering the dye laser and firing the electron beam was carefully adjusted to yield maximum laser output energy.

A comprehensive computer-based data acquisition system[2] was used to monitor the performance of the dye laser and excimer amplifier for every individual shot. The temporal profile of the injected and amplified beams is recorded by calibrated photodiodes. The pulse energy and the spectral profile of the output beam are measured by a pyroelectric energy meter and an optical multichannel analyzer (OMA), respectively. The electron beam generator was characterized by monitoring the electron energy, the beam current, the voltage on the final output switch and the pressure jump inside the gas cell due to the energy deposition.

The XeF(C→A) excimer gas mixture is transversely excited by a short (10 ns FWHM), high energy (650 keV) electron beam with a peak current of 85 kA. An energy density of ~120 J/l is deposited into the gas resulting in a pumping rate of ~12 MW/cm^3. The electron beam generator can be operated at a PRF of up to 1 Hz. The optimized gas mixture consisted of 12 Torr NF_3, 1 Torr F_2, 15 Torr Xe, and 750 Torr Kr, completed with Ar to a total pressure of 6.5 bar. The spatially averaged

peak gain was measured to be 0.03 cm^{-1}. A detailed description of the excimer system can be found in Ref. 2.

A positive branch confocal unstable resonator geometry was used for the amplifier cavity. The dye laser pulse was injected through a hole centered in the concave end mirror. The magnification of the resonator was M=1.33 corresponding to 23 single passes of the injected pulse through the gain medium. Mirrors with high reflective coatings for the wavelength region from 465 to 505 nm, covered the entire tuning range of the injection laser. The active gain region was 50 cm long and 35 mm in diameter, limited by the aperture of the resonator.

A transverse flow system allowed repetitive operation of the excimer amplifier without energy degradation due to thermally induced turbulence in the gas cell. Interferomertric measurements have shown complete relaxation of the laser gas within 40 ms after electron beam excitation[6].

The dye laser was especially designed for use as an injection source for the XeF(C→A) amplifier[9]. The main criterion for the injection laser was to provide precise and rapid wavelength tunability on a shot-to-shot basis for any preselected random list of wavelengths over the entire gain band of the dye laser. In spite of the 1 Hz limit of the present electron-beam facility, a maximum pulse repetition frequency of the dye laser greater than 50 Hz was desired for the purpose of demonstrating compatibility with future development of electron-beam technology. A commercial excimer pumped dye laser incorporating a modified oscillator section provided the lowest risk approach to achieve these performance characteristics. The Hansch oscillator section of the commercial unit was replaced by one based on a grazing incidence grating as the primary wavelength dispersive element. Wavelength agility is achieved by using a beam reducing telescope between the grating and a galvonometer driven mirror. In this way, a large portion of the grating can be illuminated for excellent wavelength discrimination while at the same time the tuning mirror can be made quite small allowing for high speed tuning.

An equally important inovation of the injection laser system is the integration of on-line wavelength and energy diagnostics. A Fizeau wavemeter permits absolute wavelength calibration of the galvonometer driven tuning mirror as well as monitoring of the wavelength on a shot-to-shot basis. The output energy of every shot of the injection source is measured by a pyroelectric energy meter. The entire dye laser system is operated and monitored with a PC-AT micro computer.

The dye laser is tunable at a PRF of up to 50 Hz with a wavelength accuracy of 0.01 nm in its present configuration. The tuning range, using Courmarin 480 laser dye is 27 nm, centered at 478.5 nm. The maximum output energy, when pumped by a 65 ns, 150 mJ XeCl excimer pulse is 7 mJ with a pulse length of 25 ns and a linewidth of 0.015 nm.

The experiments reported in this paper were designed to demonstrate the performance of the wavelength-agile injection-controlled XeF(C→A) laser. In a first experiment the excimer laser system was tuned over 27 nm, which corresponds to the entire bandwidth of the Courmarin 480 dye laser at a PRF of 1 Hz. The wavelength of the injection laser was changed in each shot in a pre-programmed random sequence. Figure 2a shows the output energy trace, measured by a pyroelectric energy meter together with arbitrarily selected wavelengths for each shot. The energy values have an error of +10%/-0% due to a limited number of sampling points of the recording digital oscilloscope. Figure 2b depicts the corresponding spectrum, recorded by the OMA system. Pulse energies of several hundred millijoules were obtained over the whole tuning range. The measured wavelength of the amplified pulse is equal to the selected dye wavelength within the OMA resolution of 0.1 nm.

In another experiment, four atomic rubidium transition wavelengths were selected in two consecutive runs at 1 Hz PRF. Special interest in rubidium wavelengths arises from the potential use of the XeF(C→A) laser as an illuminator for remote sensing which would require an atomic resonance filtered (ARF) detection system[10]. Output energies around 700 mJ were obtained for the wavelengths 489.7 nm, 489.2 nm, and 487.4 nm

(figure 3). The smaller output energy at 492.0 nm results from the reduced injection energy of the dye laser at this wavelength and is not a limitation of the XeF(C→A) amplifier. In both runs the desired wavelengths were obtained.

Wavelength-agile tuning of the XeF(C→A) amplifier at 1 Hz was demonstrated with excellent wavelength accuracy. The entire bandwidth of the dye laser of 27 nm can be accessed with wavelength-agility and output energies of > 800 mJ with a 10 ns pulse duration are obtainable. To our knowledge this is the only laser system to date that is capable of producing pulse energies in the 1 J range in the blue-green spectral region, and simultaneously being randomly tunable at 1 Hz over a broad bandwidth. A modification of the dye laser oscillator will make the entire bandwidth of the Courmarin 480 dye of about 40 nm available to XeF(C→A) amplification, while still maintaining wavelength-agile operation at 1 Hz.

The authors wish to thank J. Hooten and M. Roman for their valuable technical assistance. This work was supported by the Office of Naval Research and the Welch Foundation.

References

1. G. J. Hirst, C. B. Dane, W. L. Wilson, R. Sauerbrey, F. K. Tittel, and W. L. Nighan, Appl. Phys. Lett. **54**, 1851 (1989)

2. C. B. Dane, G. J. Hirst, S. Yamaguchi, Th. Hofmann, W. L. Wilson, R. A. Sauerbrey, F. K. Tittel, W. L. Nighan, and M. C. Fowler to be published in IEEE J.Quantum Electron., Special Issue on Electronic Transition Gas Lasers (1990)

3. A. Mandl, and L. H. Litzenberger, Appl. Phys. Lett., **53** 1690 (1989)

4. V. S. Zuev, G. N. Kashnikov, N. P. Kozlov, S.B. Mamaev, V. K. Olrov, Y. S. Protasov, and V. A. Sorokin, Sov. J. Quantum Electron., **16**, 1665 (1986).

5. C. B. Dane, S. Yamaguchi, Th. Hofmann, R. Sauerbrey, W. L. Wilson, and F. K. Tittel, Appl. Phys. Lett., ? ?? (1990)

6. S. Yamaguchi, Th. Hofmann, C.B.Dane, R. Sauerbrey, W. L. Wilson, and F. K. Tittel, to be published in IEEE J. Quantum. Electron.

7. W. L. Nighan and M. C. Fowler, IEEE J. Quantum Electron. **25**, 791, (1989).

8. N. Hamada, R. Sauerbrey, and F. K. Tittel, IEEE J. Quantum Electron. **24**, 2458 (1988) also: modeling paper revision

9. R. A. Rubino, W. L. Nighan, W. H. Glenn, A. J. Cantor and M. J. Roman p160, UV2.3, Conference digest of the 1989 LEOS annual meeting Orlando, FL (1989)

10. J. A. Gelbwachs, IEEE J. Quantum. Electron. **24**, 1266 (1988).

11. N.Hamada, R. Sauerbrey, W. L. Wilson, F. K. Tittel, and W. L. Nighan, IEEE J. Quantum. Electron. **24**, 1571 (1988).

Figure captions

Fig. 1: Schematic diagram of the experimental arrangement. The NDFs are the neutral density filters, PD1 and PD2 are the vacuum photodiodes, and OMA is the optical multichannel analyzer

Fig. 2 Temporal and spectral dependence of laser output of a randomly wavelength tuned 1 Hz shot sequence.

(a): Pulse energy versus time. The wavelength of each shot is indicated.

(b): Spectrum of the same shot sequence shown in figure 2a recorded by an OMA. The elevated base line is due to a summation of pedestals of the single shot recordings. The numbers at the top of the figure represent the order in which the shots were taken

Fig. 3: Temporal scan of laser output energy of four rubidium transitions at 1 Hz. The wavelength of each shot is indicated.

Fig. 4: Wavelength scan over the 483.2 nm absorption line in the free running XeF(C→A) laser spectrum. The scan speed was 1 Hz, the wavelength steps were 0.05 nm. The insert shows the position of the absorption line in the free running laser spectrum.

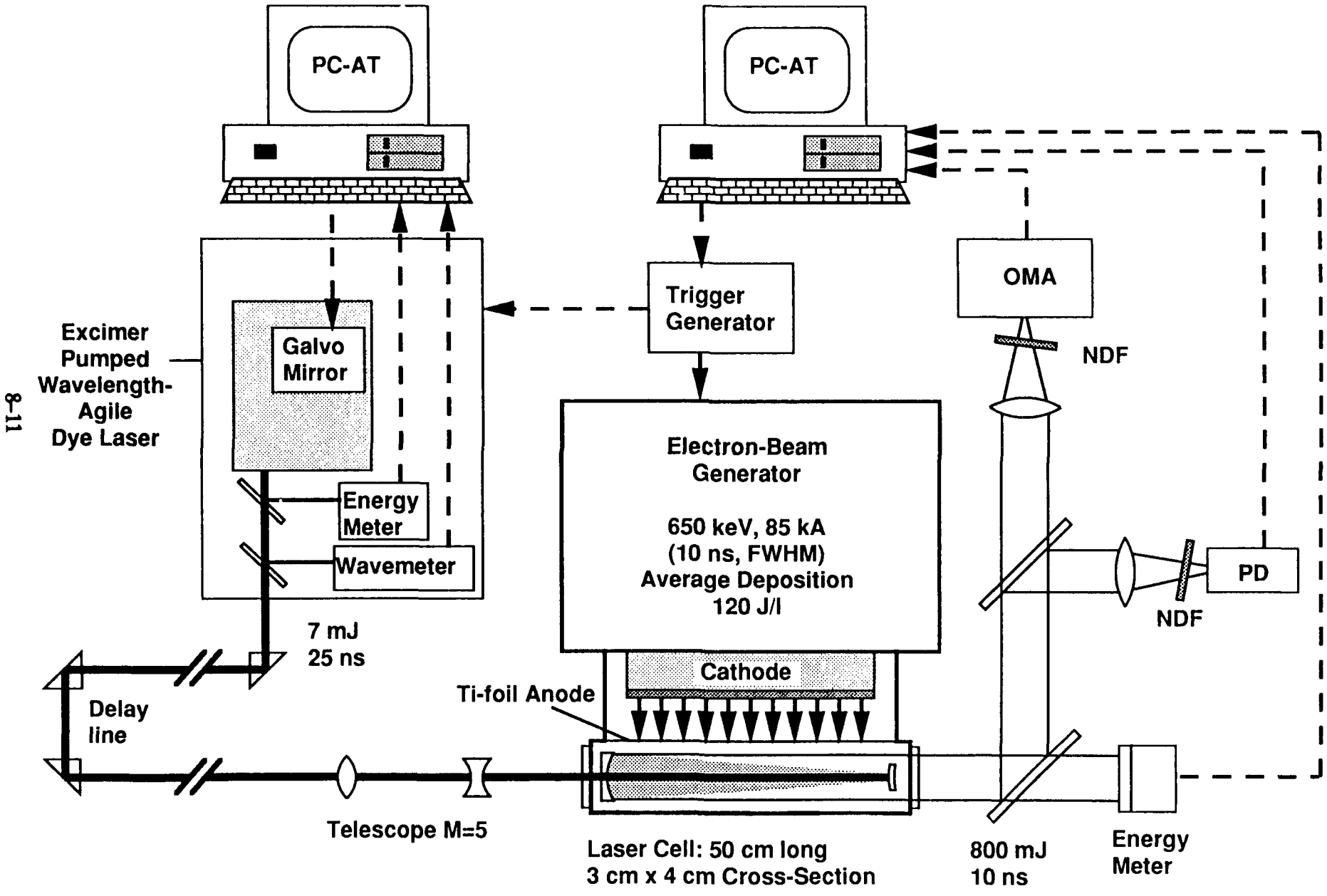
PC-AT
PC-AT
Trigger Generator
OMA
NDF
Excimer Pumped Wavelength-Agile Dye Laser
Galvo Mirror
Energy Meter
Wavemeter
Electron-Beam Generator
650 keV, 85 kA
(10 ns, FWHM)
Average Deposition
120 J/l
PD
NDF
7 mJ
25 ns
Cathode
Ti-foil Anode
Delay line
Telescope M=5
Laser Cell: 50 cm long
3 cm x 4 cm Cross-Section
800 mJ
10 ns
Energy Meter

Fig. 1

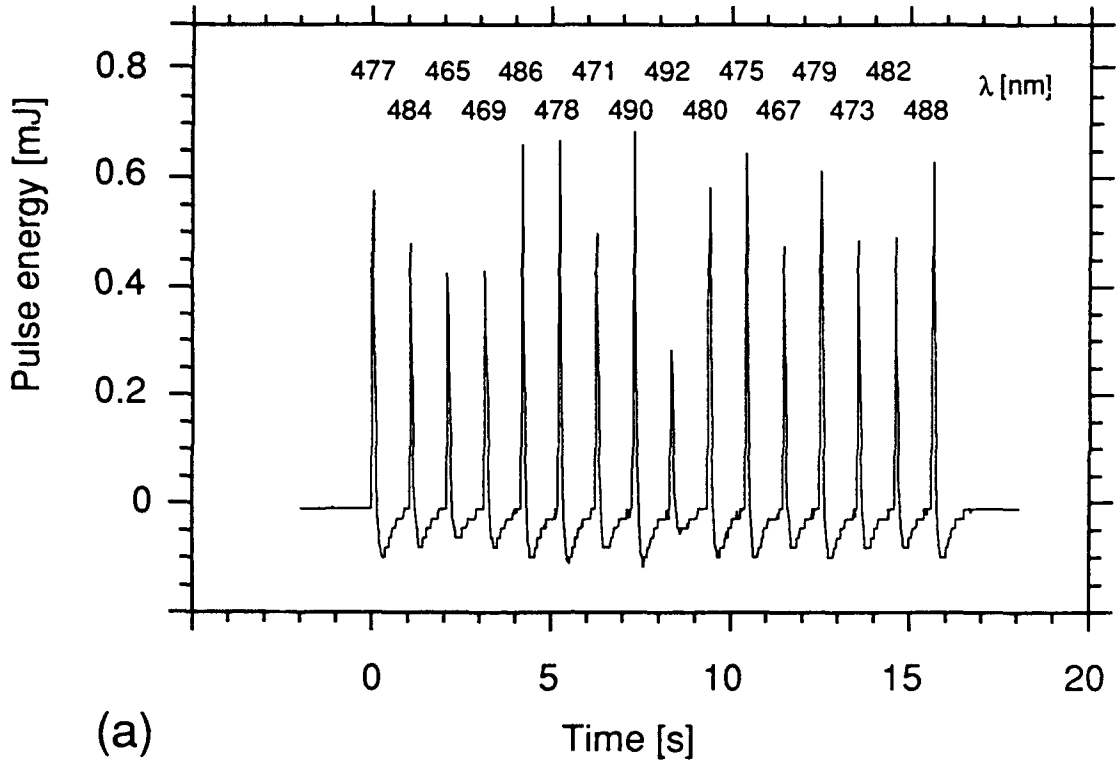
Pulse energy [mJ]
0.8
0.6
0.4
0.2
0
477 465 486 471 492 475 479 482
484 469 478 490 480 467 473 488
λ [nm]
0
5
10
15
20
Time [s]

(a)

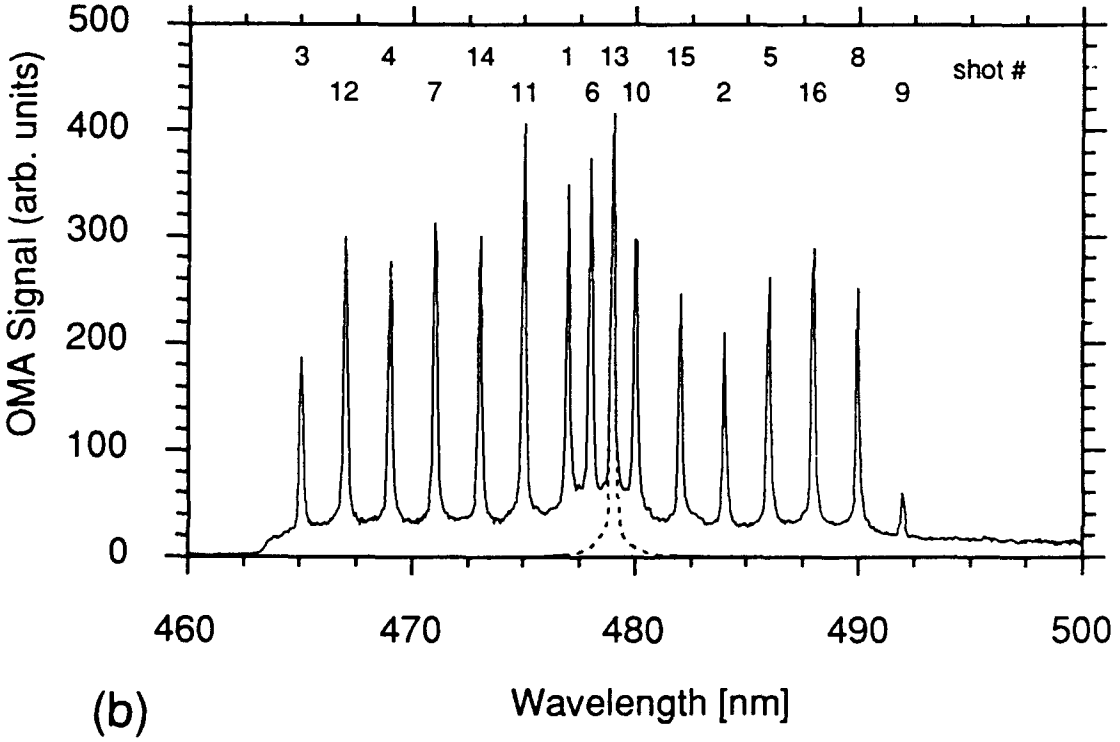
OMA Signal (arb. units)
500
400
300
200
100
0
3 4 14 1 13 15 5 8
12 7 11 6 10 2 16 9
shot #
460
470
480
490
500
Wavelength [nm]

(b)

Fig. 2

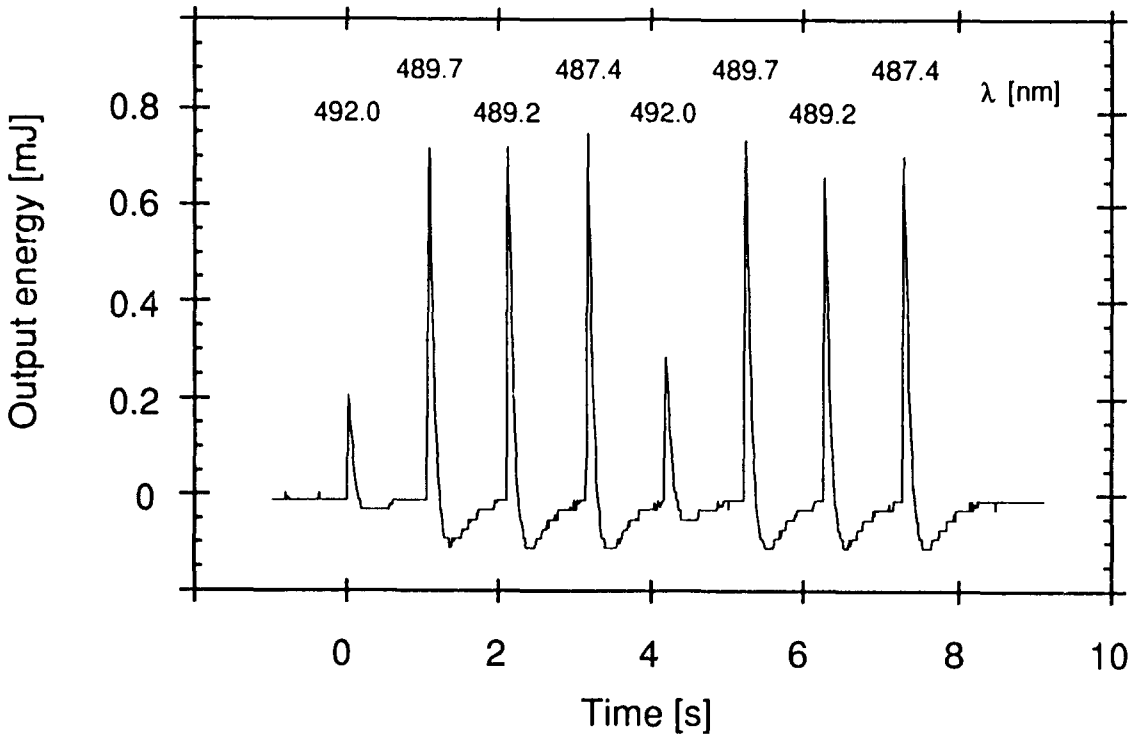
Output energy [mJ]
0.8
0.6
0.4
0.2
0
0
2
4
6
8
10
Time [s]
λ [nm]
492.0
489.7
489.2
487.4
492.0
489.7
489.2
487.4

Fig. 3

Scaling Characteristics of the XeF(C→A) Excimer Laser

C. B. Dane, G. J. Hirst, S. Yamaguchi, Th. Hofmann,

W. L. Wilson, R. Sauerbrey, and F. K. Tittel

Rice University

Department of Electrical and Computer Engineering

Houston, TX 77251-1892

W. L. Nighan and M. C. Fowler

United Technologies Research Center

East Hartford, CT 06108

Abstract: The scaling characteristics and medium properties of an injection controlled XeF(C→A) laser pumped by a 10 ns high current density electron beam have been investigated. A five component laser gas mixture consisting of F_2, NF_3, Xe, Kr, and Ar was optimized for the scaled laser conditions resulting in 0.8 J output pulses at 486.8 nm, corresponding to an energy density of 1.7 J/ℓ and an intrinsic efficiency of 1.3 %. Detailed small signal gain measurements combined with kinetic modeling permitted the characterization of the dependence of net gain on the electron beam energy deposition and gas mixture composition, resulting in an improved understanding of XeF(C→A) laser operation.

Scaling Characteristics of the XeF(C→A) Excimer Laser

C. B. Dane, G. J. Hirst, S. Yamaguchi, Th. Hofmann,

W. L. Wilson, R. Sauerbrey, and F. K. Tittel

Rice University

Department of Electrical and Computer Engineering

Houston, TX 77251-1892

W. L. Nighan and M. C. Fowler

United Technologies Research Center

East Hartford, CT 06108

I. Introduction

There is increasing interest in the XeF(C→A) excimer laser as an efficient, tunable source of radiation in the blue-green region of the spectrum. Using an electron beam as an excitation source and a *kinetically tailored* five component gas mixture [1], efficient operation of this laser system has been demonstrated for short pulse 10 ns, ~10 MW/cm^3 [2], intermediate pulse 250 ns, ~1 MW/cm^3 [3], and long pulse 700ns. ~250 kW/cm^3 [4] electron beam pumping durations. When the short pulse, high current density electron beam excitation technique is employed, peak values of small signal gain exceed 3 %/cm permitting efficient injection controlled operation using a low power injection beam. This results in narrow-band, high beam quality operation and provides a very effective method

for wavelength tuning. Continuous tuning between 450 and 530 nm has been demonstrated, and an output energy density of >1 J/ℓ has been achieved for wavelengths between 470 and 510 nm [5].

With its gaseous active medium, the XeF(C→A) excimer laser is readily scalable to the high energy and power required for applications in remote sensing, materials processing, optical communications, and the amplification of ultrashort laser pulses. Experiments are described here that characterize the successful scaling of a high current density electron beam pumped XeF(C→A) laser from an active volume of ~0.02 ℓ [6] to one of ~0.5 ℓ. The effect of the scaled volume on the optimum laser gas mixture composition is considered in detail. Through a careful mapping of the spatial distribution of electron beam energy deposition, the relationship between kinetic processes, small signal gain, and laser performance has been determined in order to identify optimum pumping conditions.

II. Experimental apparatus

A. Electron beam pumping

The XeF(C→A) excimer laser was transversely pumped by a pulsed (10 ns FWHM), high current density electron beam customized for this application [7]. Electrons were emitted from a 50 cm x 2 cm carbon felt cathode through a 25 μm titanium foil window into the laser gas mixture as illustrated in Fig. 1. Typical diode peak voltage and current were 650 kV and 80 kA, respectively. Using a Faraday probe, a peak current density of ~150 A/cm^2 was measured on the optical axis when the laser cell was filled with 6.5 bar of Ar (Fig. 2). The electron beam system is capable of repetitive operation at up to 1 Hz.

The spatial distribution of the electron beam energy deposition in the gas was measured using chlorostyrene film [8]. For a typical laser gas mixture, an average of 150 J/ℓ was deposited on the optical axis of the laser cell with ±15% variations from this average along the 50 cm pumped length (Fig. 3). The slight roll-off in energy deposition away from the center of the cell was due in part to a ~1° rotation of the electron beam caused by a 0.2 tesla magnetic field used to guide the electron beam. The use of this guide field resulted in a three-fold increase in the electron current delivered at the optical axis.

As expected, the energy deposition varied significantly in the direction of the electron beam propagation due to electron energy loss and scattering in the 6.5 bar laser gas mixture. The deposition ranged from over 200 J/ℓ near the foil to less than 100 J/ℓ at the back wall of the laser cell. A contour plot of the measured energy deposition through a cross section near the center of the cell, as experimentally measured with chlorostyrene film, is shown in Fig. 4. For an active laser volume 3.5 cm in diameter and 50 cm long (0.48 ℓ), the electron beam energy deposition was typically ~125±10 J/ℓ, averaged over this volume. A pressure transducer installed in the laser cell was used to measure the transient pressure rise following an electron beam pumping pulse, resulting in energy depositions consistent (±10 %) with the integrated chlorostyrene film measurements [9].

B. Laser cell and resonator

The laser cell and gas handling system were constructed entirely of stainless steel using Viton and Teflon vacuum seals. The surface of the titanium foil in contact with the laser gas was coated with a 5 μm thick layer of aluminum using ion vapor deposition. This coating prevented interaction between the

titanium and the fluorine and was found to significantly increase the lifetime of the gas mixtures. The laser gas mixture components were introduced into the cell sequentially, and then mixed by circulating them through an external loop at 1 ℓ/min using a small high pressure bellows pump. The cell, electron beam foil, and gas handling systems were initially passivated by filling the system with 3 bar of a 10% F_2 in Ar gas mixture for a period of 24 h.

The optical cavity configuration used in these experiments was a positive branch confocal unstable resonator. The back reflector was a plano-concave lens with the concave surface (radius of curvature = R_1) coated to achieve maximum reflectivity from 465 to 505 nm. This coating was also designed to allow greater than 80% transmission near the ~350 nm wavelength of the competing XeF(B→X) transition. A 1.5 mm injection aperture, centered on the back reflector, was formed either by drilling a hole through the optical substrate or by masking a 1.5 mm spot during the coating process. The latter method was found to provide the most well defined aperture and became the preferred technique The output coupler was a double meniscus lens (radii of curvature = R_2, $-R_2$) with a round maximum reflectivity spot centered on the convex surface. For each cavity magnification (R_1/R_2), the size of this spot was chosen such that the outer diameter of the laser beam, given by the product of the spot diameter and the magnification, was ~35 mm. The distance between the mirrors was adjusted to the confocal spacing of $(R_1 - R_2)/2$.

Two resonator configurations were used in these experiments. In the first, the cavity mirrors were located inside the laser cell in contact with the gas mixture on externally adjustable mounts. The optical coatings were protected from the corrosive laser gases by an aluminum oxide overcoating. In the second configuration, the mirrors were located *outside* the laser cell which was sealed

with anti-reflection coated fused silica windows tilted by 3°. The internal resonator had a magnification of 1.7 (R_1 = 2.73 m, R_2 = 1.61 m), an output coupler spot diameter of 21 mm, and a mirror spacing of 56 cm. This magnification was chosen to optimize the peak power and near field output energy of the scaled XeF(C→A) laser [10]. Gas mixture optimization experiments were performed using a 75 cm long *external* resonator with a magnification of 2.0 (R_1 = 3.00 m, R_2 = 1.50 m) and an output coupler spot diameter of 17.5 mm.

C. Injection source

A dye laser pumped by a 60 ns FWHM XeCl excimer laser provided a 45 ns FWHM injection pulse with a linewidth of ~0.005 nm as measured using a monitor etalon with a finesse of 30 and a free spectral range of 30 GHz [5]. The relatively long pulsewidth allowed the unstable resonator to be completely filled with injected photons before the onset of gain resulting in quasi-CW injection. The beam diameter was adjusted with a telescope so that the 1.5 mm injection hole was uniformly illuminated, transmitting approximately 60% of the injection pulse into the optical cavity. The injection intensity was varied using neutral density filters at the dye laser output. With no attenuation, it was possible to deliver ~2 mJ through the unstable resonator injection hole corresponding to a peak intensity of ~3 MW/cm^2, a value close to the ~5-6 MW/cm^2 saturation intensity of the XeF(C→A) transition.

For an well aligned system, a portion of the injection beam was backreflected through the injection aperture along the same path as the incoming beam. The amplification of this backreflected pulse in the dye laser gain cell resulted in the truncation of the outgoing injection pulse as well as damage to optical components of the dye laser. To avoid this difficulty, an optical delay line

was used to increase the round trip transit time between the injection source and the electron beam pumped amplifier to 40 ns.

D. System diagnostics

The diagnostics system was designed to extensively characterize the operation of both the XeF(C→A) laser and the electron beam generator on each laser shot. As depicted in Fig. 5, the laser output temporal profile was measured by a vacuum biplanar photodiode, the spectral profile by an optical multichannel analyzer (O.M.A.) spectrometer, and the energy by a pyroelectric energy meter. A second photodiode was used to monitor the dye laser injection control pulse. Electron beam diagnostics consisted of voltage and current monitors in the diode and a Marx bank charging voltage monitor. The shot-to-shot energy deposition in the laser gas was monitored using the signal from the pressure transducer which was calibrated against the chlorostyrene film measurements. The signal from the photodiode monitoring the XeF(C→A) output was recorded using a 500 MHz scan-converting transient digitizer and the remaining temporal signals were collected using a 4-channel 400 Msample/s and a 2-channel 10 Msample/s digital oscilloscope. A single computer system configured the instruments and collected each of the diagnostic signals for each laser shot.

III. Gas mixture optimization

The first experiments with the scaled injection controlled XeF(C→A) laser system were performed using a five-component gas mixture which had been previously optimized for a small-scale laser having a similar electron beam pumping rate but with a 10 cm active length and a volume of only 0.02 ℓ [6]. That gas mixture was comprised of 8 Torr NF_3, 1 Torr F_2, 8 Torr Xe, 300 Torr Kr, and Ar, with a total pressure of 6.5 bar. In our prior work, the dual halogen donor, dual

rare gas buffer composition was found to result in a significant reduction in transient blue-green absorption and the suppression of the competing XeF(B→X) transition [1]. Detailed kinetic modeling successfully described this performance enhancement and accurately predicted small signal gain profiles for a variety of laser gas mixtures and electron beam pumping conditions [11]. However, the scaling of the active medium length from 10 cm to 50 cm introduced an additional factor affecting the optimum XeF(C→A) laser gas mixture.

A. KrF(B→X) competition

The presence of Kr as a buffer in the laser gas results in the formation of the KrF excimer. Indeed, modeling indicates a KrF(B→X) gain on the order of 10 %/cm for mixture conditions otherwise optimum for XeF(C→A) laser operation. Nonetheless, for the short 10 cm single pass gain length and resonator optics having low reflectivities at 248 nm, no KrF lasing was observed for conditions typical of the earlier small-scale experiments [6]. However, when the gain length was scaled by a factor of five to 50 cm, oscillation on the KrF(B→X) laser transition occurred, using the mixture optimized for the small scale experiment. This resulted in significant laser output at 248 nm and a reduction in the XeF(C→A) gain. The primary adverse effect of KrF oscillation on XeF(C→A) laser output is the reduction in the population of Kr_2F, a major XeF(C) precursor [1], [11]. Since KrF is the precursor of Kr_2F, strong stimulated emission on the KrF(B→X) transition results in lower KrF, Kr_2F, and XeF(C) populations.

Using the gas mixture optimized for the small scale experiments, along with the internally mounted M = 1.7 resonator and an injection intensity of ~2 MW/cm^2 at 486.8 nm, 0.6 J laser output pulses were measured in the first tests of the scaled laser system. Spectral analysis revealed that the laser output consisted of

output at the amplified injection wavelength as well as at the 248 nm wavelength of the KrF transition. Using a Corning 3-74 filter to block the UV portion of the output (cut off at ~420 nm), it was determined that ~0.45 J was emitted at 486.8 nm and ~0.15 J at 248 nm. An examination of the temporal profiles depicted in Fig. 6 shows that the KrF gain and laser output occurs much earlier than those of the XeF(C→A) transition. As might be expected from this fact, the energy of the UV pulse was independent of the performance of the XeF(C→A) laser. If the visible injection was omitted, the XeF(C→A) laser produced only ~0.03 J free-running output but the UV output was unaffected. For the conditions of Fig. 6, the 248 nm pulse and the free-running blue-green pulse were collected during the same shot and the injection controlled pulse was recorded on a subsequent laser shot.

Figure 7 shows the measured Kr pressure dependence of the output of the injection controlled XeF(C→A) amplifier at 486.8 nm, along with the XeF(B→X) and KrF(B→X) lasers at 351 and 248 nm, respectively. At the 300 Torr Kr pressure found to be optimum for XeF(C→A) laser operation in our earlier small scale experiments, the KrF laser output reaches its maximum value and the scaled XeF(C→A) output exhibits a pronounced dip. However, the data of Fig. 7 show that the laser output from the KrF transition is easily suppressed by increasing the partial pressure of Kr in the gas mixture above 300 Torr, with a maximum in XeF(C→A) output occurring at a Kr pressure of 1200 Torr. For Kr pressures greater than 1000 Torr, the UV output is almost completely suppressed. Using a gas mixture comprised of 8 Torr NF_3, 1 Torr F_2, 8 Torr Xe, and 1200 Torr Kr, completed to 6.5 bar with Ar, injection controlled pulses were obtained with energies of 0.7 J [2]. The injection laser was tuned to 486.8 nm, a wavelength near the peak of the spectral gain profile. For the 0.48 ℓ active laser

volume and a measured spatially averaged energy deposition of 120 J/ℓ, this corresponded to an energy density of 1.5 J/ℓ and an intrinsic efficiency of 1.2%, respectively [2].

B. Scanning of gas mixture components

Although the competing KrF laser oscillation was suppressed by increasing the Kr pressure to 1200 Torr, the NF_3, F_2, and Xe partial pressures were not reoptimized. Thus a systematic optimization of the laser gas mixture was undertaken in order to maximize the XeF(C→A) laser extraction efficiency. A second requirement, of course, was the continued suppression of the KrF(B→X) laser. Pyroelectric energy meters were chosen to monitor the laser output at the injected and UV wavelengths since quantitative measurements using the O.M.A. spectrometer were complicated by the spectral response of the detector array and by differences in beam size and collimation between the blue-green and UV laser output. A schematic of the measurement system using two pyroelectric energy meters, one of which was equipped with a filter to block 248 nm is shown in Fig. 8. The signal from detector *A* was corrected for losses from the uncoated fused silica beamsplitter and the UV filter. By removing the UV filter the signal from detector *B* was then calibrated against that from *A* . In this manner, the visible (*A*) and UV (*B* - *A*) were measured for each laser shot. Since the UV measurement was the difference of two larger measurements, small negative values sometimes resulted for UV output energies near zero.

For the purpose of these measurements, the *external* unstable cavity was used in order to ensure long term stability of the resonator coatings. However, the intracavity losses introduced by the laser cell windows and increased unpumped cavity length resulted in XeF(C→A) laser energies somewhat smaller

than those observed with the internal resonator, as predicted [10]. An injection pulse at 486.8 nm with a peak intensity of ~2 MW/cm^2 was used in all cases. Although the laser output was much more sensitive to small changes in the net gain for the linear, unsaturated amplification regime resulting from smaller injection intensities, this intensity was chosen for these experiments to ensure that the laser system was optimized under the conditions for which saturation of both gain and absorber species occurred. The partial pressure of each gas component was scanned, leaving the other component pressures fixed, to determine the value for which the XeF(C→A) laser energy was optimized. The concentration of that constituent was then fixed at a value near the measured optimum before the next gas component was scanned. In this manner, two iterations were made through the NF_3, F_2, Xe, and Kr mixture components, always maintaining a total laser gas pressure of 6.5 bar with the Ar buffer. Small variations were then made from the final gas mixture by simultaneously changing the concentration of two or more components to verify that a performance peak had been achieved.

Figures 9 to 12 show the measured XeF(C→A) laser energy at 486.8 nm and the total UV laser energy for variations in Xe, Kr, NF_3, and F_2, respectively. Five to six measurements using the same laser gas fill were averaged for each data point shown. The error bars represent the standard deviation of the relative scatter of the measured energies for a given set of conditions. This scatter was largely a result of small differences in injection laser synchronization, resonator alignment, and gas mixture lifetime. For this reason more representative values probably lie nearer the top of each bar than the center. The absolute accuracy of the measurements was limited in most cases by the pyroelectric energy meter calibration of ±10%, an uncertainty not represented in the error bars.

The KrF(B→X) laser output was easily quenched by increasing the partial pressure of Xe in the gas mixture as shown in Fig. 9. However, an increase in the Xe concentration beyond a level at which the UV output is almost completely suppressed results in reduced blue-green output from the XeF(C→A) laser due to the increased quenching of XeF by Xe and broadband absorption from the photoionization of Xe(5d) and (6p) [1], [11]. When the Xe partial pressure was fixed at the observed performance maximum of 14 Torr, the optimum Kr pressure (Fig. 10) decreased to ~750 Torr from 1200 Torr [2]. The optimum XeF(C→A) laser output was found at higher NF_3 pressures (Fig. 11) than used on the small scale system [6] resulting in less sensitivity to the F_2 concentration (Fig. 12). However, improved laser output continued to result from the addition of ~1 Torr of F_2. The findings of the gas constituent scanning experiments are consistent with the small signal gain computed using our XeF(C→A) laser kinetics model, described in detail elsewhere [11]. Figure 13 shows the computed peak value of the XeF(C→A) net gain at 490 nm for variations in the Xe and fluorine donor partial pressures. Broad maxima in the computed gain are observed for Xe and fluorine donor pressures in the 10-20 Torr range, a result consistent with the experimental data of Figs. 9, 11, and 12.

Figure 14 shows the computed dependence of peak XeF(C→A) net gain on Kr partial pressure. In earlier work [1], analysis of the dependence of XeF(C→A) fluorescence decay and laser energy on Kr pressure resulted in an inferred rate coefficient of ~1.0×10^{-32} $s^{-1}cm^6$ for the three body quenching reaction, XeF(C) + Kr + Ar → products. This rate coefficient is parameterized in the presentation of Fig. 14. Clearly, a rate coefficient very nearly equal to the ~1.0×10^{-32} $s^{-1}cm^6$ value inferred earlier is consistent with the experimental observation of a broad

maximum in XeF(C→A) laser energy for Kr partial pressure in the 450-900 Torr range (Fig. 10).

C. Results of mixture optimization

On the basis of the constituent scanning experiments, an optimized gas mixture consisting of 12 ± 2 Torr NF_3, 1 ± 0.5 Torr F_2, 12 ± 2 Torr Xe, and 750 ± 150 Torr Kr, completed with Ar to a total pressure of 6.5 bar, was determined for the scaled XeF(C→A) electron beam pumped laser system. Using this mixture, laser output energies in excess of 0.8 J at 486.8 nm were measured from the system with the *internal* resonator, corresponding to an intrinsic efficiency of 1.3% and an energy density of 1.7 J/ℓ. The most significant aspect of the laser gas mixture modification performed upon scaling from a 0.02 to a 0.5 ℓ active laser volume was the competition by the KrF(B→X) laser which was suppressed in a straightforward manner by the described mixture adjustments. The basic composition of the laser gas mixture remained very similar to those of previous laser experiments, and the behavior of the scaled system continued to be consistent with the current understanding of the kinetics of the XeF(C→A) multi-component gas mixture [11].

IV. Gain measurements

A. Gain measurement technique

The scaled electron beam pumped laser system with its uniformly excited 50 cm active length provided the opportunity for more accurate small signal gain measurements than were possible using the small scale apparatus [6]. The interpretation of previous measurements was complicated by the small 10 cm pumped length over which the electron beam energy deposition varied by more

than a factor of three from each end to the center. Aside from the need for detailed gain measurements for use as input data for analytical modeling of the injection control process [10], [12], a careful study of the dependence of gain on energy deposition into the laser gas mixture is required to investigate the optimum electron beam pumping intensity.

A flashlamp pumped dye laser with a pulsewidth of ~200 ns was used as a gain probe in these experiments. The output was tuned to 486.8 nm and the peak intensity was attenuated to ~50 W/cm^2 using neutral density filters to avoid saturation effects in the gain medium. The diameter of the probe was adjusted to 2 mm and was aligned on the vertical center of the gain region, parallel to the titanium foil electron beam window. As described previously, an energy deposition gradient existed from the foil to the back of the laser cell due to the attenuation of the electron beam as it propagated through the high pressure gas (Fig. 4). This was used to advantage since, by translating the probe beam along the direction of electron beam propagation, gain could be measured as a function of electron beam energy deposition. The gain signals were measured using a vacuum photodiode and consisted of the temporally broad dye laser probe background onto which was superimposed the net gain profile. The largest source of uncertainty in the measurement of the peak net gain was in the estimation of the shape of the dye laser profile during the XeF(C→A) gain pulse.

B. Temporal profiles

The measured net gain curves were found to be very similar to those obtained using the small previously reported 0.02 ℓ device [6], exhibiting peak gains of ~3 %/cm with a ~25 ns FWHM. Figure 15 illustrates typical temporal profiles and the significant reduction of the transient absorption that occurs during

the electron beam pumping pulse as Kr is added to the mixture. The XeF(C→A) peak gain was observed to be much less sensitive to the Kr partial pressure than the output energy of the injection controlled laser (Fig. 10). This, it is believed, can be attributed to two effects. First, although the dye laser injection pulse is *much longer (~40 ns) than the gain pulse, when there is strong absorption* during electron beam pumping (low Kr partial pressure), essentially all of the injected photons are removed from the cavity. Since the unstable resonator cannot be refilled with injection flux before the net gain reaches its peak, the extraction efficiency is reduced. Secondly, during the small signal gain measurements, the absence of a laser resonator resulted in reduced oscillation on the KrF(B→X) and XeF(B→X) transitions. As described in the previous section, these are in direct competition with the XeF(C→A) laser output (Fig. 7) and are effectively suppressed by the use of higher Kr partial pressures.

Figure 16 shows computed temporal gain profiles for conditions similar to those of Fig. 15. Generally, the agreement between the measured and computed temporal profiles is very good. However, modeling indicates a larger reduction in the strong absorption during the electron beam beam pulse with increasing pressures of Kr. The absorption with no Kr in the mixture is believed to be due primarily to photodissociation of Ar_3^+ [1], [11]. The addition of Kr reduces the concentration of Ar_3^+ and its Ar_2^+ precursor by charge exchange. Since there is practically no rate coefficient data for Ar_3^+, known rate coefficients for Ar_2^+ were used in the modeling of Ar_3^+ [11], *including the rate coefficient for* Ar_3^+ - Kr charge exchange. This is one possibility for the discrepancy. Also, in the region of initial absorption, the computed *net* gain is the difference between two larger quantities, the XeF(C) contribution to gain and the absorption due to Ar_3^+ and other species. Thus, the computed net gain is subject to larger errors during the

electron beam pumping than those typical in the afterglow region for which agreement between theory and experiment is very good.

C. Gain and laser energy dependence on pumping intensity

Using the gas mixture optimized for the scaled XeF(C→A) amplifier as described in the previous section, gain measurements were made along the direction of the optical axis at distances between 2 and 40 mm from the foil electron beam window where each position corresponded to a different energy deposition level. With spatially resolved deposition measurements, such as those presented in Fig. 4, it was then possible to plot the peak net gain versus energy deposition. Figure 17 shows measurements for two different laser gas mixtures. Also shown in the figure are calculated values of gain versus energy deposition. Clearly, the qualitative and quantitative agreement between theory and experiment is good, with the differences between the two within the uncertainty of each. Previous measurements on the small scale electron beam device indicated the onset of gain saturation for a volume averaged deposition level of ~80 J/ℓ with a peak in the intrinsic laser efficiency occurring at ~90 J/ℓ [6]. However, interpretation of the earlier measurements was complicated by highly nonuniform electron beam pumping. For the scaled device described here, little evidence of gain saturation was observed as the gain continued to increase up to an energy deposition of 200 J/ℓ corresponding to a pumping rate of 20 MW/cm^3. To verify that the injection controlled laser output reflected the trend in the measured gain, the charging voltage of the Marx bank capacitors of the electron beam machine was varied between 65 and 95 kV in order to adjust the energy deposition throughout the gas volume. As shown in Fig. 18, over a spatially averaged energy deposition range from 75 to 125 J/ℓ a nearly linear

dependence of laser energy was observed, with no apparent indication of saturation or the occurrence of a peak in the intrinsic efficiency.

V. Summary and discussion

Scaling of the high current density electron beam pumped XeF(C→A) excimer laser from an active volume of ~0.02 ℓ to one of ~0.5 ℓ has been successfully demonstrated. Using an internal resonator with a magnification of 1.7, an optimized five-component gas mixture, and an injection intensity of ~3 MW/cm^2 (~2 mJ), laser output energies in the range of 0.75 - 0.85 J were measured at 486.8 nm, a wavelength near the maximum of the XeF(C→A) gain spectrum. This corresponds to an energy density of 1.7 J/ℓ and an intrinsic efficiency of 1.3 %, compared to maximum values of 1.6 J/ℓ and 1.5 % for similar average energy deposition and injection intensity using the 0.02 ℓ laser system [6]. Moreover, the increased single pass gain of the scaled laser permitted the use of *external* optics with only a small penalty in energy extraction efficiency. We believe that this is the first operation of a XeF(C→A) laser with an *external* resonator.

A. Scaling

A significant aspect in the scaling of the XeF(C→A) laser to larger active volumes was an increased level of competition by oscillation on the KrF(B→X) 248 nm transition. With the increased dimensions of the laser resonator, the spectral properties of the reflective coatings became less effective in the suppression of this competition. However, relatively minor adjustments in gas mixture composition, specifically increases in the partial pressure of Xe and Kr as well as an increase in the ratio of NF_3 to F_2, effectively quenched laser action at 248 nm. This resulted in energy extraction efficiencies at the level that had been

demonstrated previously for the small scale device. Further scaling of the laser length may require additional mixture adjustments to maintain the kinetic suppression of KrF.

Detailed mapping of the spatial distribution of electron beam energy deposition through the pumped gas volume in the direction of electron propagation and an increased uniformity in energy deposition along the direction of the optical axis permitted accurate determination of the dependence of small signal gain on energy deposition. The results of these experiments have led to a revised understanding of XeF electron quenching. Electron quenching was formerly believed to limit efficient electron beam pumping of the XeF(C→A) laser to deposition levels of ~100 J/ℓ using a short (~10 ns), high current density excitation pulse. However, the present measurements (Fig. 17) indicate that the onset of saturation in the small signal gain does not occur until the deposition levels reach ~200 J/ℓ (~20 MW/cm^3). Thus, it can be concluded that further increases in the specific energy density of the XeF(C→A) laser could be obtained by increasing the electron pumping current densities to values even higher than those available in the current apparatus. This is a significant finding with regard to future scaling of the XeF(C→A) laser beyond the levels we have presently demonstrated.

B. Electron beam excitation

The recent reports of efficient XeF(C→A) laser energy extraction using low power density, ~250 kW/cm^3 in ~700 ns [4], and intermediate power density, ~1 MW/cm^3 in 250 ns [3], electron beam pumping demonstrate that efficient XeF(C→A) laser operation is *relatively* insensitive to the electron beam excitation conditions. Indeed, the values of intrinsic laser efficiency and volumetric energy

density reported for long pulse excitation are comparable to those reported here for which the electron beam power density and temporal duration were nearly two orders of magnitude larger and smaller, respectively. Moreover, since the technology is well developed for both *high* and *low* power electron beam excitation (short and long pulse durations), scaling considerations should not influence the excitation format to a significant degree. Rather, the choice between short pulse and long pulse XeF(C→A) lasers will in most cases be determined by the application. The high power pumping format presented here results in net gains which are large over a ~50 nm bandwidth (>2 %/cm) and is therefore ideally suited for applications that require efficient, high beam quality, narrowband operation which is continuously tunable over a wide wavelength range.

Acknowledgements

We would like to acknowledge the valuable technical assistance of J. R. Hooten of Rice University. This work was supported by the Office of Naval Research, the Robert Welch Foundation, and the National Science Foundation.

References

1. W. L. Nighan, R. Sauerbrey, Y. Zhu, F. K. Tittel, and W. L. Wilson, "Kinetically Tailored Properties of Electron beam Excited XeF(C→A) and XeF(B→X) Laser Media Using an Ar-Kr Buffer Mixture," *IEEE J. Quantum Electron.*, Vol. 23, pp. 253-261, 1987.

2. G. J. Hirst, C. B. Dane, W. L. Wilson, R. Sauerbrey, F. K. Tittel, and W. L. Nighan, "Scaling of an injection-controlled XeF(C→A) laser pumped by a repetitively pulsed, high current density electron beam," *Appl. Phys. Lett.*, Vol. 54, pp. 1851-1853, 1989.

3. P. J. M. Peters, H. M. J. Bastiaens, W. J. Witteman, R. Sauerbrey, C. B. Dane, and F. K. Tittel, "Efficient XeF(C→A) Laser Excited by a Coaxial E-beam at Intermediate Pumping Rates," to appear in *IEEE J. Quantum Electron*, September, 1990.

4. A. Mandl and L. H. Litzenberger, "Efficient, long pulse XeF(C→A) laser at moderate electron beam pump rate," *Appl. Phys. Lett.*, Vol. 53, pp. 1690-1692, 1989; OE/LASE '90, Los Angeles, California, January, 1990.

5. C. B. Dane, S. Yamaguchi, Th. Hofmann, R. Sauerbrey, W. L. Wilson, and F. K. Tittel, "Spectral Characteristics of an Injection Controlled XeF(C→A) Excimer Laser," submitted to *Appl. Phys. Lett.*

6. N. Hamada, R. Sauerbrey, W. L. Wilson, F. K. Tittel, and W. L. Nighan, "Performance Characteristics of an Injection-Controlled Electron-Beam Pumped XeF(C→A) Laser System," *IEEE J. Quantum Electron.*, Vol. 24, pp. 1571-1578, 1988.

7. S. Lloyd, Y. G. Chen, G. McAllister, M. Montgomery, T. Olson, J. Shannon, B. Dane, G. Hirst, R. Sauerbrey, F. Tittel, and W. Wilson, "A 500 kV Rep-Rate Electron Beam Generator," Proceedings of the Seventh IEEE Pulsed Power Conference, Monterey, California, 1989.

8. W. P. Bishop, K. C. Humpherys, and P. T. Randike, "Poly(halo)styrene Thin-Film Dosimeters for High Doses," *Rev. Sci. Instrum.*, vol. 44, pp. 443-452, 1973.

9. G. J. Hirst, C. B. Dane, R. Sauerbrey, W. L. Wilson, and F. K. Tittel, "Scaling Demonstration of the XeF(C→A) Laser," *Metal Vapor, Deep Blue, and Ultraviolet Lasers*, Proc. SPIE 1041, pp. 149-154 (1989).

10. C. B. Dane, Th. Hofmann, G. J. Hirst, S. Yamaguchi, R. Sauerbrey, and F. K. Tittel, "Optimization of an Injection Controlled Excimer Laser Guided by Analytical Modeling," to be published.

11. W. L. Nighan and M. C. Fowler, "Kinetic Processes in XeF(C→A) Laser Media Excited by a High Current Density Electron Beam," *IEEE J. Quantum Electron.*, Vol. 25, pp. 791-802, 1989.

12. N. Hamada, R. Sauerbrey, and F. K. Tittel, "Analytical Model for Injection-Controlled Excimer Laser Amplifiers," *IEEE J. Quantum Electron.*, Vol. 24, pp. 2458-2466, 1988.

Figures

1. Cross-sectional view of the electron beam pumped laser cell. Electrons are emitted from the 2 cm wide by 50 cm long carbon felt cathode across the 2.2 cm anode-cathode gap. The hibachi support ribs and the back of the titanium foil serve as the anode. For these experiments, the optical resonator diameters were 3.5 cm resulting in an active laser volume of 0.48 ℓ.

2. Temporal current density profiles measured inside the laser cell using a Faraday probe with a diameter of 3.8 mm. The probe was positioned 10, 20, and 30 mm from the foil. Attenuation was the result of scattering and energy deposition in the 6.5 bar gas mixture. Peak values of ~150 A/cm^2 were observed on the optical axis (20 mm) with a FWHM of 10 ns.

3. Energy deposition profile along the optical axis (20 mm from the titanium foil) as measured by chlorostyrene film. Typically, ±15% variations were observed from an average value (denoted by a dashed line) of ~150 J/ℓ. The slight roll off in energy deposition from the center of the laser cell was due in part to a ~1° rotation of the electron beam by the 0.2 tesla magnetic guide field.

4. Constant energy deposition contours through a cross section near the center of the laser cell measured using chlorostyrene film. An average deposition of 142 J/ℓ was measured for this cross section of the optical resonator corresponding to an average of ~125 J/ℓ for the entire 0.48 ℓ resonator volume. This resulted in a total deposited energy of ~60 J in the active laser medium.

5. A schematic of the experimental layout showing energy, temporal, and spectral diagnostics. The laser cell in this case is shown with *external*

resonator optics. OMA: optical multichannel analyzer, PD: vacuum photodiode, NDF: neutral density filter, BS: uncoated fused silica beamsplitter.

6. (a). Output pulses observed from the XeF(C→A) laser using an M = 1.7 internal resonator and the gas mixture previously optimized for the small scale laser [6]. The mixture was comprised of 8 Torr NF_3, 1 Torr F_2, 8 Torr Xe, 300 Torr Kr, and completed to 6.5 bar using an Ar buffer. The pulses are displayed on an arbitrary vertical scale; their relative sizes do not reflect actual relative intensities. An energy of ~0.15 J was measured for the KrF(B→X) pulse and ~0.45 J for the injection controlled XeF(C→A) pulse. For the purpose of comparison, the temporal evolution of the ~0.03 J broadband free-running XeF(C→A) laser is also shown. The KrF(B→X) and XeF(C→A) free-running laser temporal profiles were measured for the same electron beam shot. The injection controlled output and the Faraday probe signal were measured on separate shots. Temporal synchronization was ensured by triggering the transient digitizer with the signal from the diode voltage monitor of the electron beam generator.

   (b). Computed temporal evolution of the KrF(B→X) and XeF(C→A) small signal gain profiles for typical experimental conditions.

7. Laser output energies at the XeF(C→A), XeF(B→X), and KrF(B→X) wavelengths for the injection controlled laser using an internal M = 1.7 resonator. The gas mixture, optimized for the small scale experiments, consisted of 8 Torr NF_3, 1 Torr F_2, 8 Torr Xe, and was completed to 6.5 bar using an Ar buffer. An obvious decrease occurs in the XeF(C→A) output at the Kr pressure for which peak in KrF(B→X) oscillation is observed. A Kr

pressure of ~300 Torr was found to be optimum in the small scale apparatus in which KrF(B→X) competition was not significant [6]. Modeling shows that for this mixture both the XeF(C→A) and KrF(B→X) gain reach their maximum value for this Kr pressure. The dashed line represents an estimated projection of XeF(C→A) laser performance in the *absence* of the KrF(B→X) laser competition.

8. Schematic of the two pyroelectric energy meter setup for measuring the blue-green and UV output of the laser system. A Corning CS 3-74 color glass filter with a cutoff at 420 nm and 88% transmission at 486.8 nm was used to filter out the UV from the light reaching detector *A*. The signal from *A* was corrected for losses from the beamsplitter and UV filter. The signal from *B* was then cross calibrated against that from *A* with the UV filter removed. The sensitivity of the energy meters at 248 nm differed by less than 10% from that in the blue-green.

9. Laser output energies at 486.8 nm (open circles) and in the UV (filled circles) as a function of Xe partial pressure measured as described in Fig. 8. The gas mixture consisted of 8 Torr NF_3, 1 Torr F_2, 300 Torr Kr, and was completed to 6.5 bar using an Ar buffer. The *external* M = 2 resonator was used with a ~2 MW/cm^2 injection pulse at 486.8 nm. The error bars denote the standard deviation of the measured scatter for a given set of experimental conditions and do not include the ±10% absolute uncertainty in the calibration of the energy meters. The arrow indicates the optimum Xe pressure for the small scale laser.

10. Laser output energies at 486.8 nm (open circles) and in the UV (filled circles) as a function of Kr partial pressure. The Xe partial pressure was set at 14 Torr,

the observed maximum from Fig. 9. The remaining gas mixture consisted of 8 Torr NF_3, 1 Torr F_2, and was completed to 6.5 bar using an Ar buffer. The increase in Xe pressure from 8 to 14 Torr reduced the Kr pressure required to completely suppress the KrF(B→X) output from 1200 Torr [2] to ~500 Torr. The arrow indicates the optimum Kr pressure for the small scale laser.

11. Laser output energies at 486.8 nm (open circles) and in the UV (filled circles) as a function of NF_3 partial pressure. The gas mixture consisted of 1 Torr F_2, 14 Torr Xe, 450 Torr Kr, and was completed to 6.5 bar using an Ar buffer. The arrow indicates the optimum NF_3 pressure for the small scale laser.

12. Laser output energies at 486.8 nm (open circles) and in the UV (filled circles) as a function of F_2 partial pressure. The gas mixture consisted of 12 Torr NF_3, 14 Torr Xe, 450 Torr Kr, and was completed to 6.5 bar using an Ar buffer. The increased optimum NF_3 pressure for the scaled XeF(C→A) laser system over that of Ref. [6] reduced the sensitivity of laser performance to the F_2 partial pressure but a measurable improvement was still observed at ~1 Torr. The arrow indicates the optimum F_2 pressure for the small scale laser.

13. Computed dependence of the peak XeF(C→A) gain at 490 nm with variation of either the fluorine donor or Xe partial pressure. The gas mixtures were comprised of: (a) 12 Torr Xe, 750 Torr Kr, Ar to complete the mixture to a total pressure of 6.5 bar, with the total fluorine donor pressure varied while maintaining an 8:1 NF_3 - F_2 ratio; and (b), 9 Torr fluorine donor pressure with an 8:1 NF_3 - F_2 ratio, 750 Torr Kr, Ar to complete the mixture to 6.5 bar, with the Xe pressure varied. The electron beam pumping conditions were similar to those of Figs. 9-12.

14. Computed variation of the peak XeF(C→A) gain at 490 nm as a function of Kr pressure. The mixture was comprised of 12 Torr Xe, 12 Torr fluorine donor (8:1 NF_3 - F_2 ratio), with Ar to complete the 6.5 bar mixture. The rate coefficient for Kr three-body quenching of XeF(C) is parameterized as described in the text. Also shown is the effect of Kr addition on the electron beam energy deposition (125 J/ℓ at ~750 Torr Kr).

15. Typical net gain temporal profiles measured using the 200 ns flashlamp pumped dye laser probe tuned to 486.8 nm and directed along the optical axis of the laser cell. A strong absorption exists during the electron beam pumping pulse which is significantly reduced by the addition of Kr [1], [11]. For these measurements, the gas mixture consisted of 8 Torr NF_3, 1 Torr F_2, 8 Torr Xe, and was completed to 6.5 bar using an Ar buffer.

16. Computed temporal variation of the net gain at 490 nm. The mixture was comprised of 12 Torr fluorine donor (8:1 NF_3 - F_2 ratio), Kr, and Ar for a total pressure of 6.5 bar. The electron beam pumping conditions were similar to those of Figs. 9-15.

17. Measured and computed XeF(C→A) peak gain at 486.8 nm as a function of electron beam energy deposition. The gain probe was translated parallel to the optical axis and the corresponding energy deposition was determined using measurements such as those presented in Fig. 4.

18. Injection controlled XeF(C→A) laser output energies measured using an internal M = 1.7 unstable resonator and the gas mixture conditions given for Fig. 17 (curve a). The spatially averaged energy deposition in the laser volume, as measured with chlorostyrene film, was varied by adjusting the charging voltage on the electron beam generator Marx capacitors. The four

measured points correspond to charging voltages of 65, 75, 85, and 95 kV. A linear relationship was observed with no indication of saturation. This suggests that an increase in the observed specific energy density could be achieved using even higher electron beam pumping rates than available with the current apparatus.

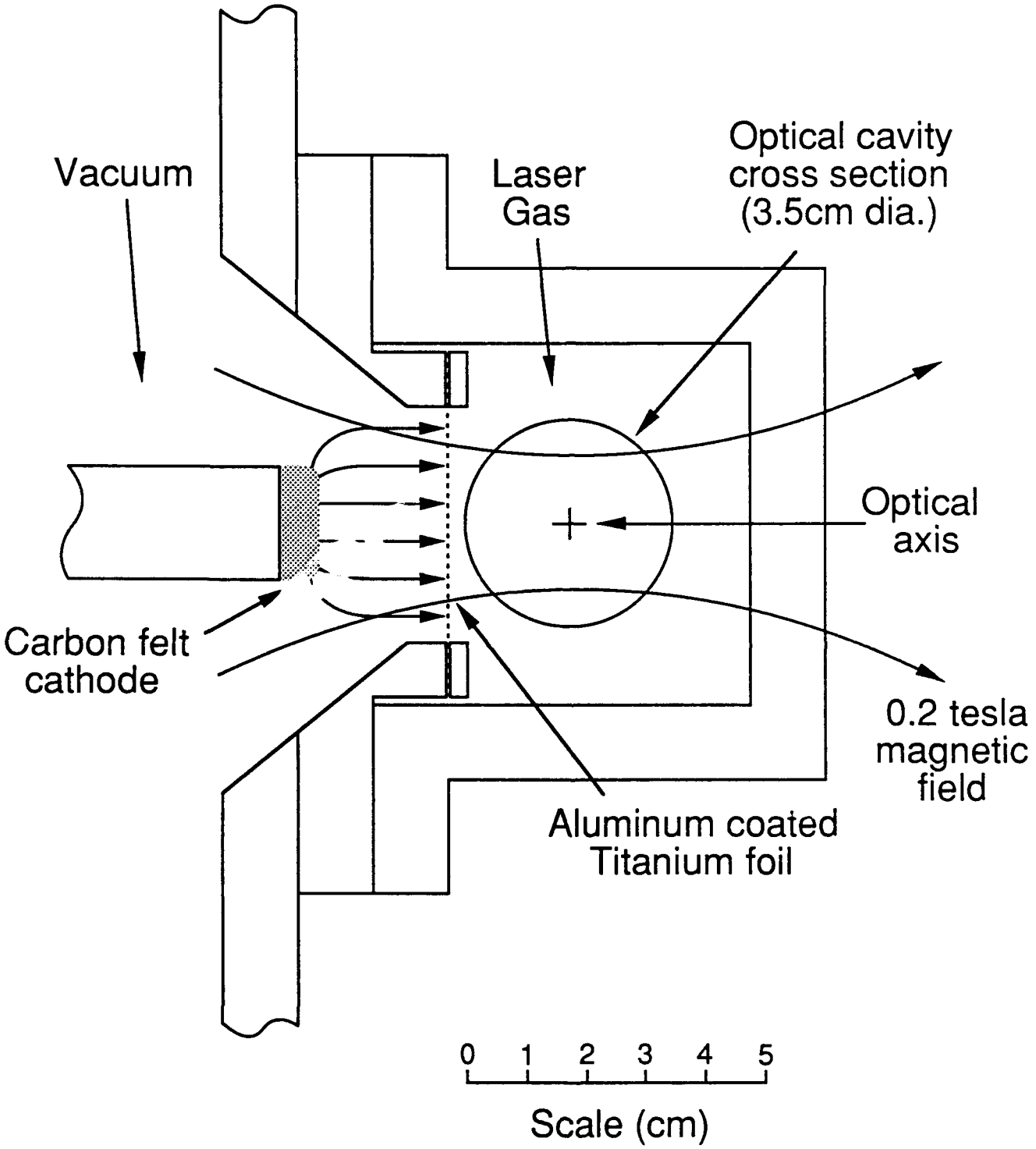
Vacuum
Laser
Gas
Optical cavity
cross section
(3.5cm dia.)
Optical
axis
Carbon felt
cathode
0.2 tesla
magnetic
field
Aluminum coated
Titanium foil
0 1 2 3 4 5
Scale (cm)

Fig. 1

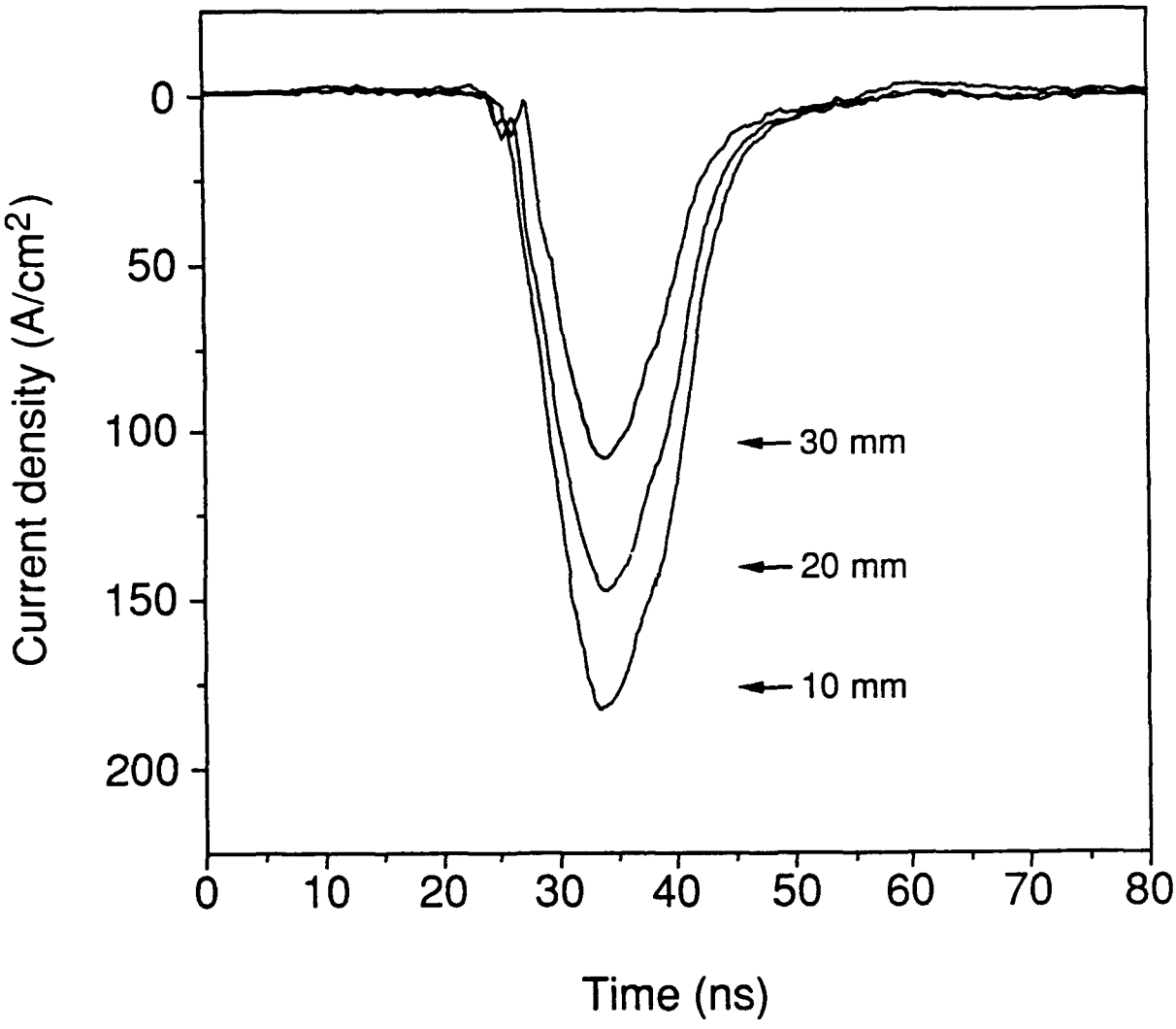
Current density (A/cm^2)
0
50
100
150
200
0
10
20
30
40
50
60
70
80
Time (ns)
30 mm
20 mm
10 mm

Fig. 2

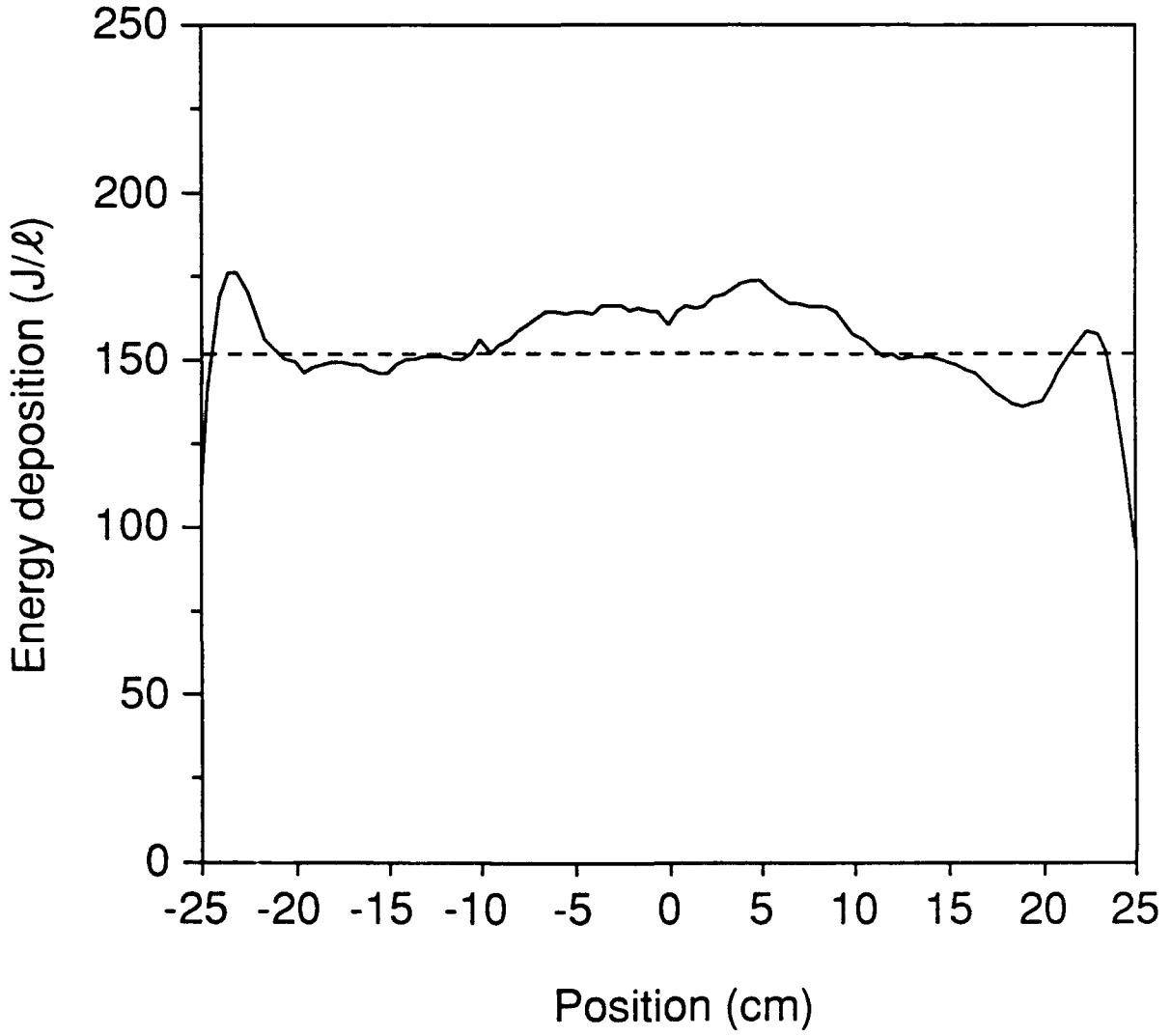
250
200
150
100
50
0
Energy deposition (J/ℓ)
-25
-20
-15
-10
-5
0
5
10
15
20
25
Position (cm)

Fig. 3

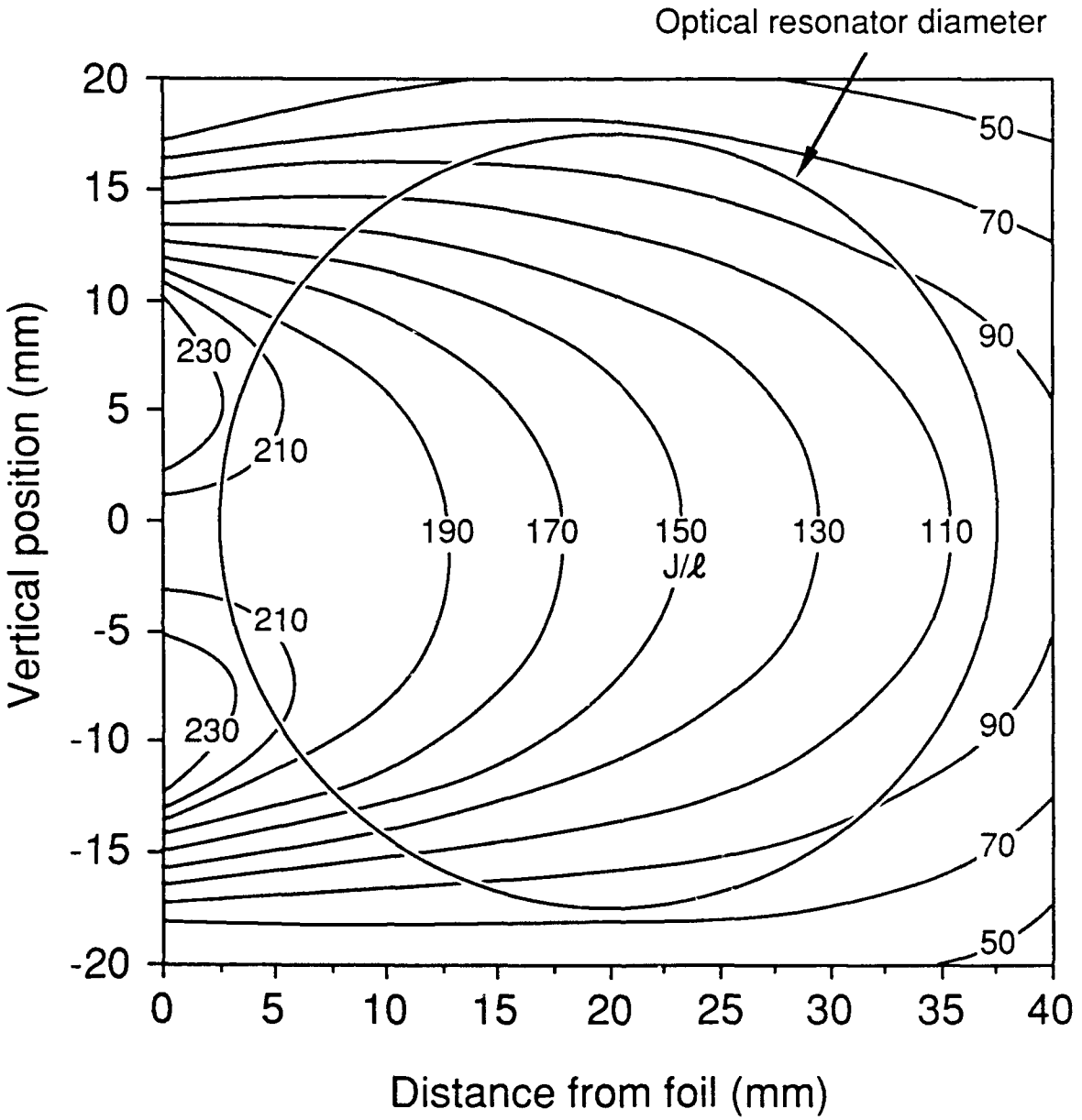
Optical resonator diameter
20
15
10
5
0
-5
-10
-15
-20
Vertical position (mm)
0
5
10
15
20
25
30
35
40
Distance from foil (mm)
50
70
90
230
210
190
170
150
J/ℓ
130
110
210
230
90
70
50

Fig. 4

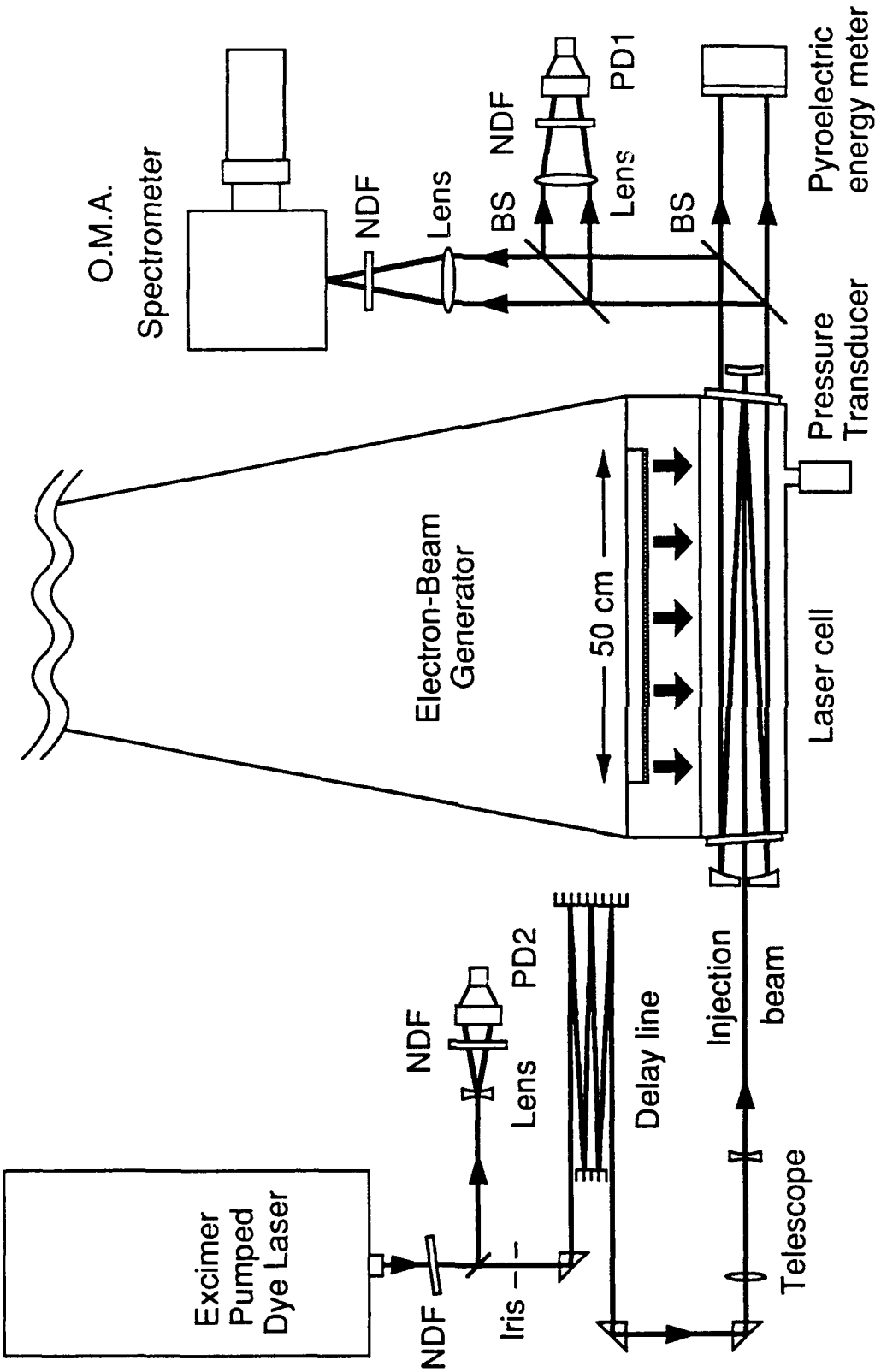
Excimer Pumped Dye Laser
NDF
Iris
NDF
Lens
PD2
Delay line
Injection beam
Telescope
Electron-Beam Generator
50 cm
Laser cell
Pressure Transducer
BS
Lens
PD1
NDF
BS
Pyroelectric energy meter
NDF
Lens
O.M.A. Spectrometer

Fig. 5

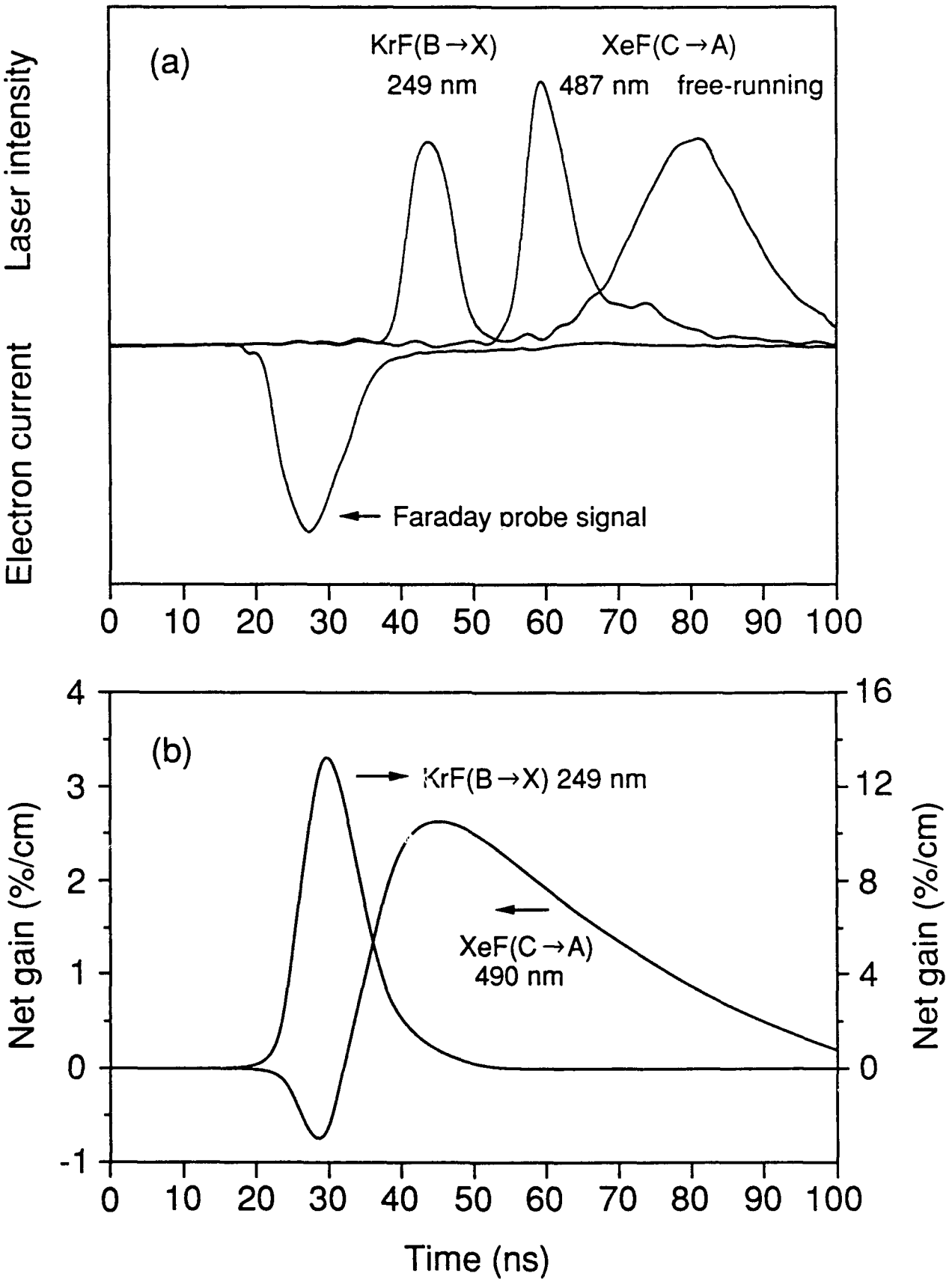
(a)
KrF(B→X)
249 nm
XeF(C→A)
487 nm free-running
Laser intensity
Electron current
Faraday probe signal
0 10 20 30 40 50 60 70 80 90 100
(b)
KrF(B→X) 249 nm
XeF(C→A)
490 nm
Net gain (%/cm)
Net gain (%/cm)
4 3 2 1 0 -1
16 12 8 4 0
0 10 20 30 40 50 60 70 80 90 100
Time (ns)

Fig. 6

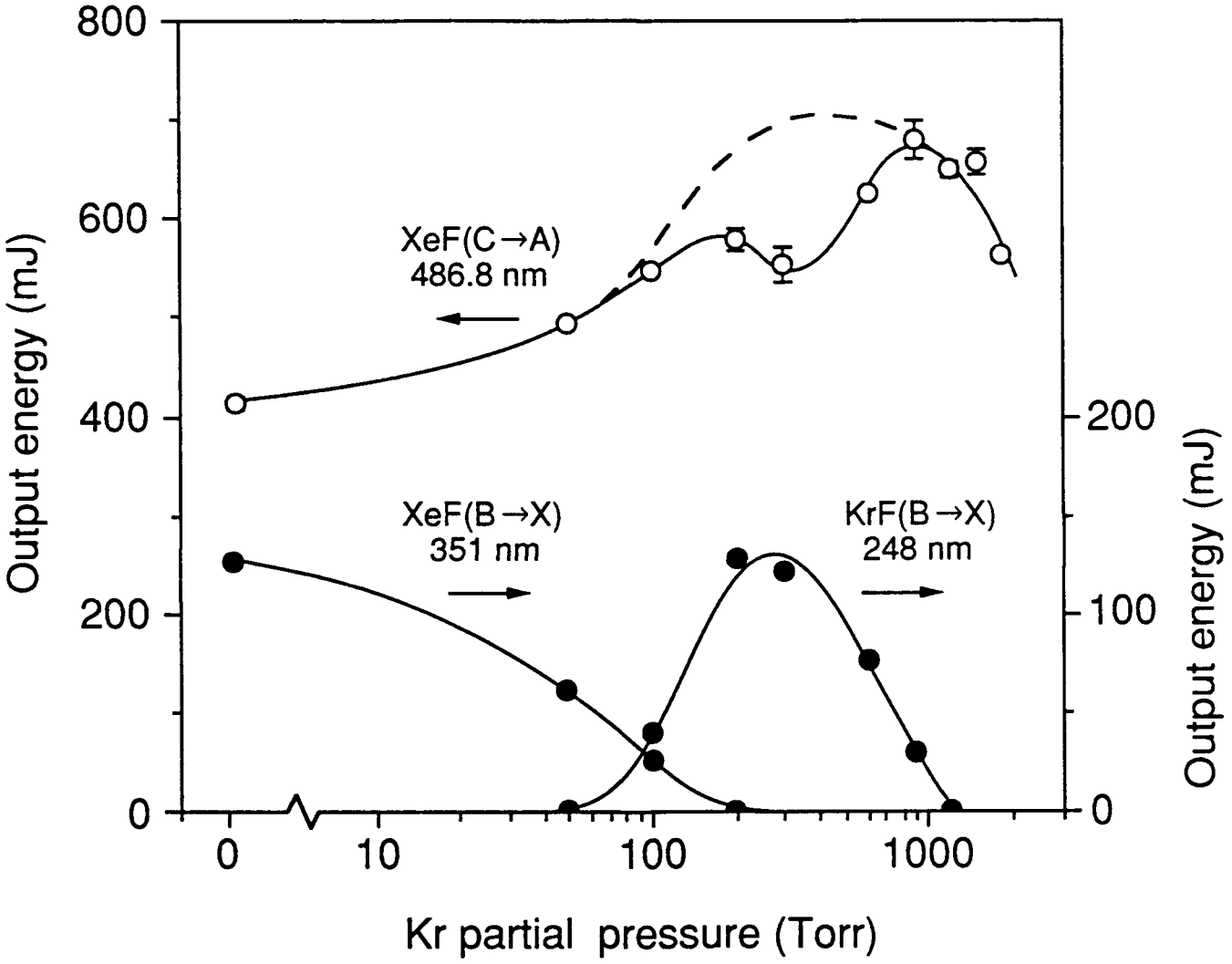
800
600
400
200
0
Output energy (mJ)
XeF(C→A)
486.8 nm
XeF(B→X)
351 nm
KrF(B→X)
248 nm
200
100
0
Output energy (mJ)
0
10
100
1000
Kr partial pressure (Torr)

Fig. 7

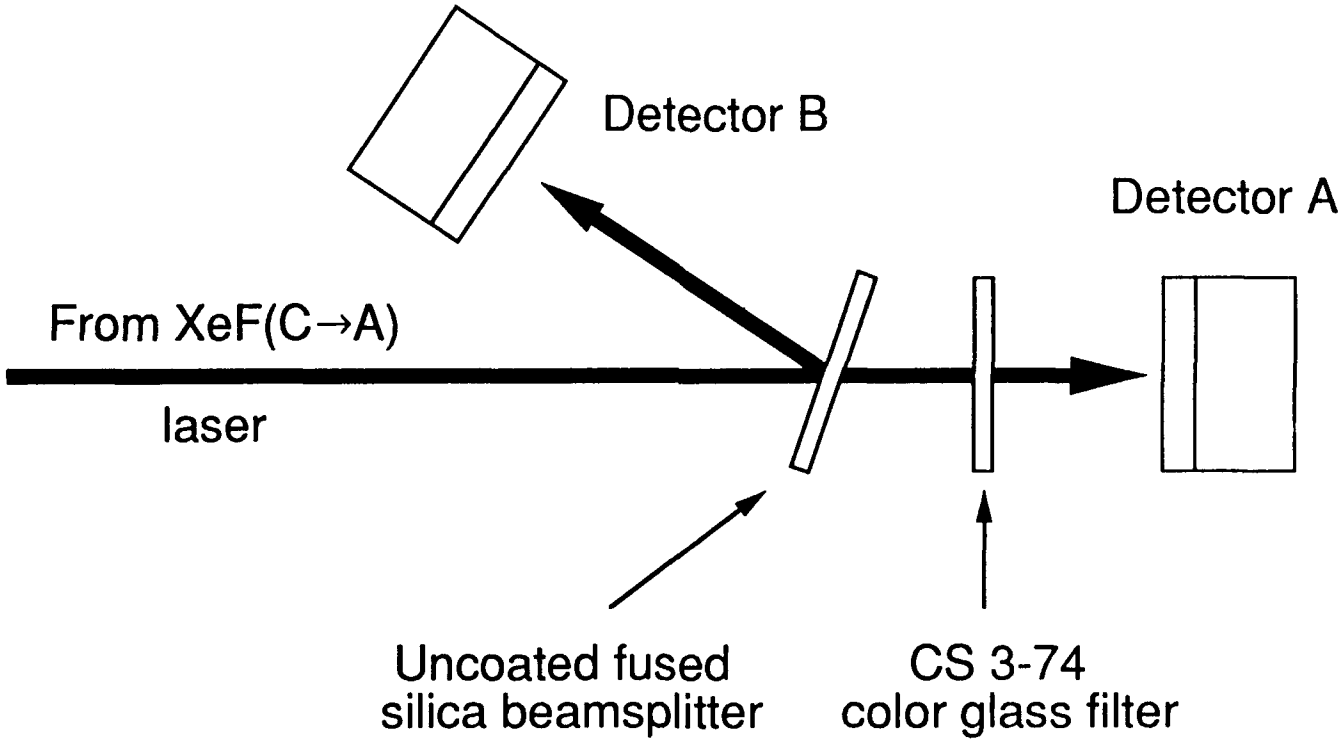
Detector B
Detector A
From XeF(C→A)
laser
Uncoated fused
silica beamsplitter
CS 3-74
color glass filter

Fig. 8

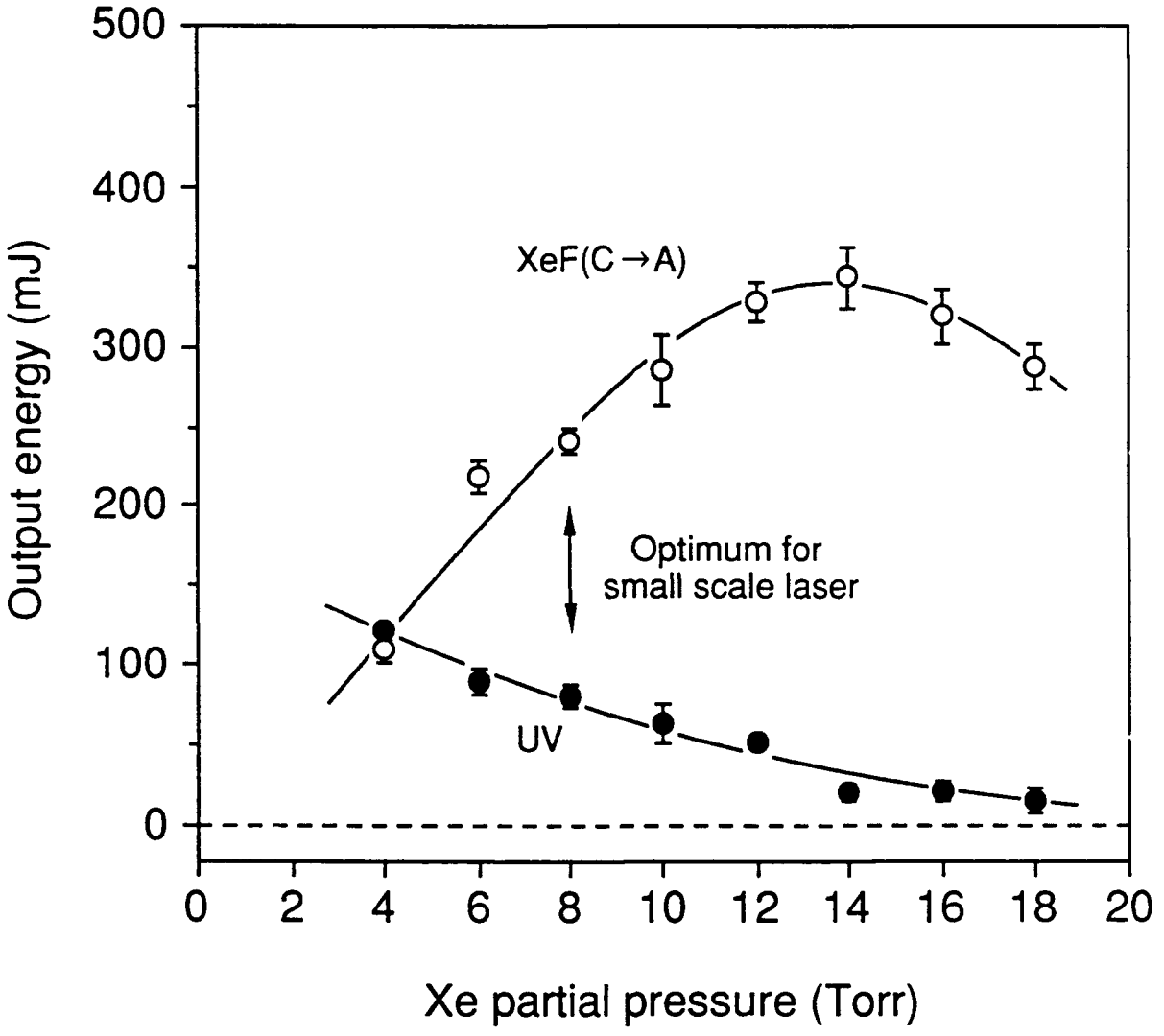
500
400
300
200
100
0
Output energy (mJ)
XeF(C→A)
Optimum for
small scale laser
UV
0
2
4
6
8
10
12
14
16
18
20
Xe partial pressure (Torr)

Fig. 9

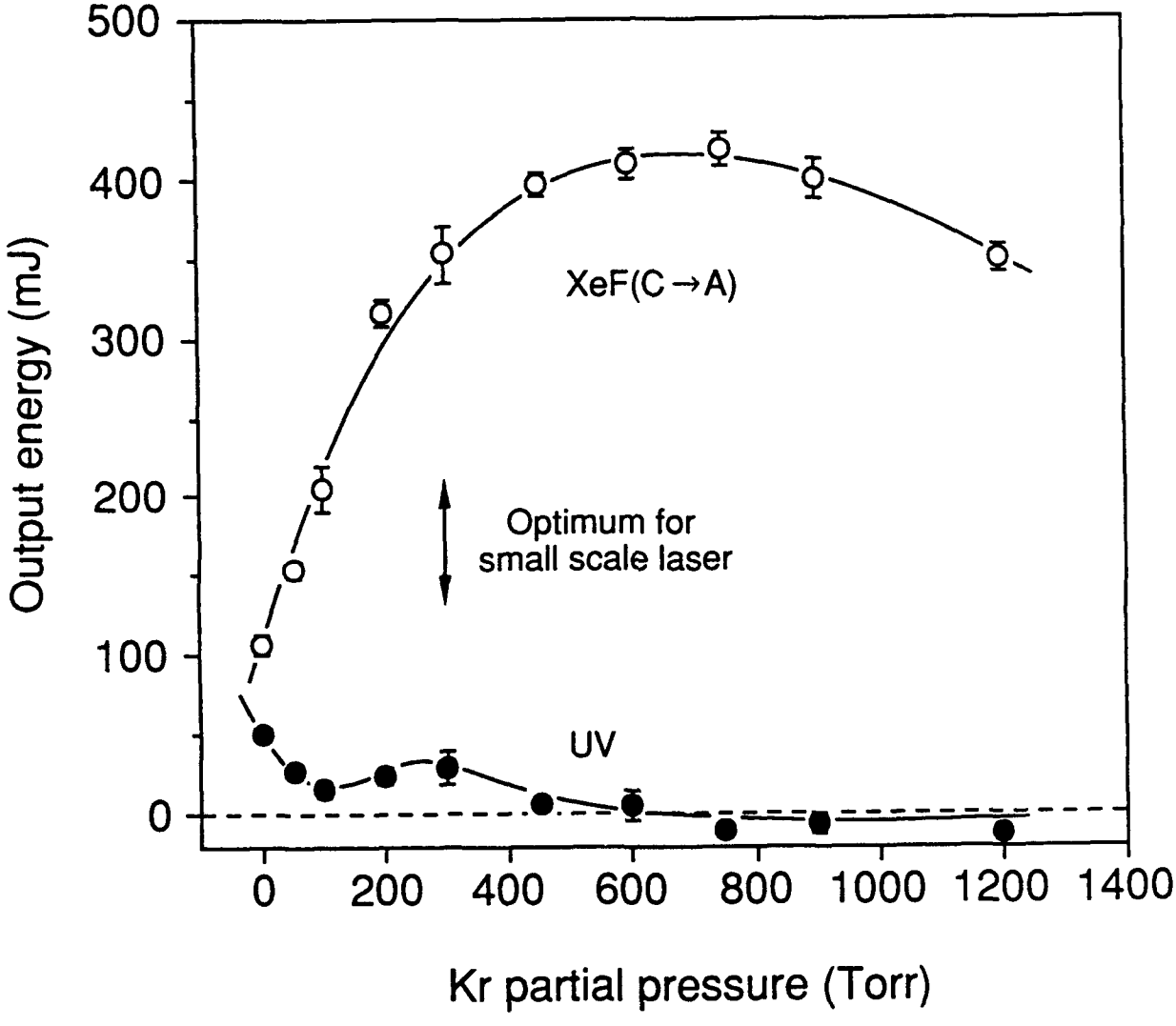
500
400
300
200
100
0
Output energy (mJ)
XeF(C→A)
Optimum for
small scale laser
UV
0
200
400
600
800
1000
1200
1400
Kr partial pressure (Torr)

Fig. 10

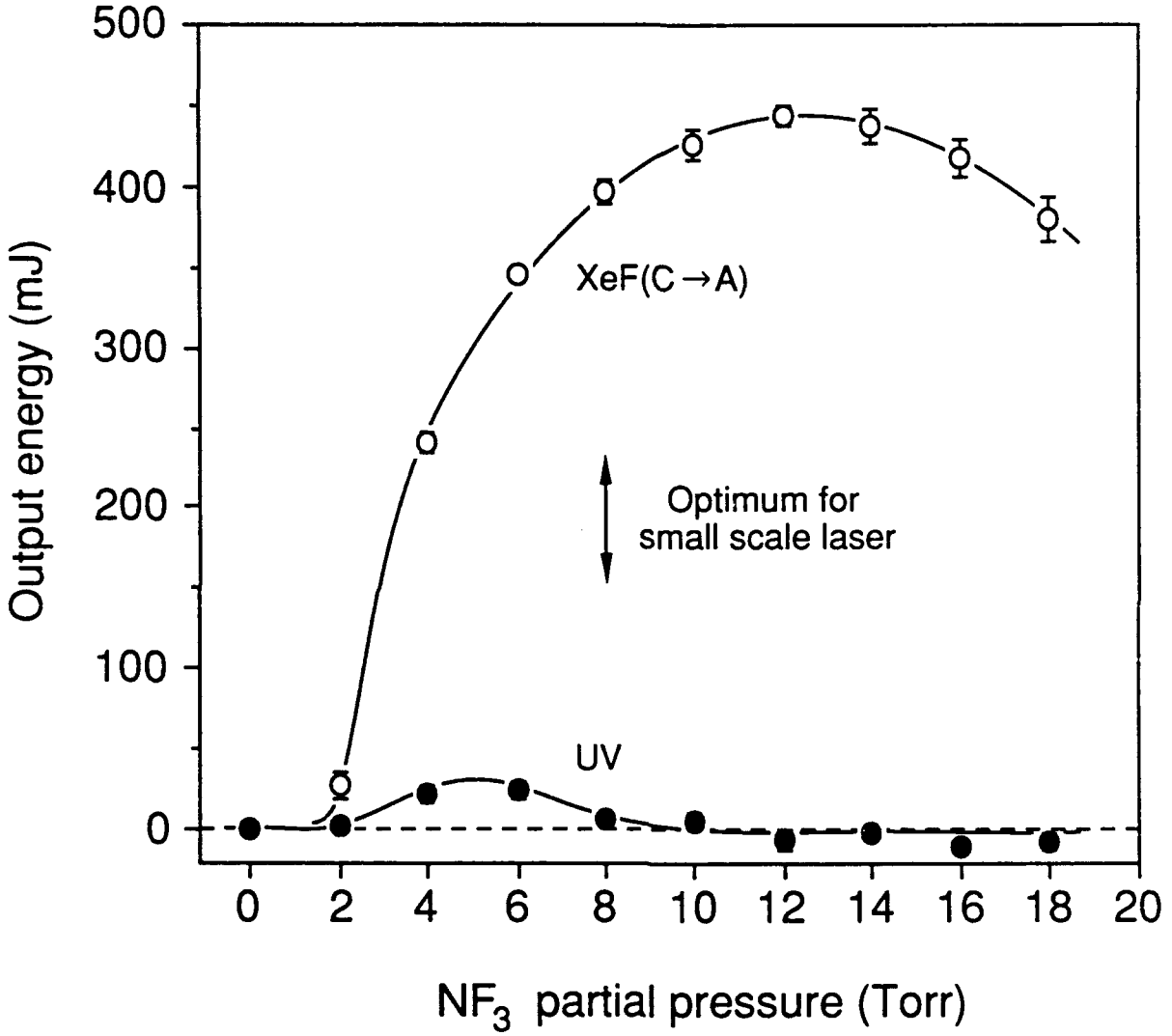
500
400
300
200
100
0
Output energy (mJ)
XeF(C → A)
Optimum for
small scale laser
UV
0
2
4
6
8
10
12
14
16
18
20
NF3 partial pressure (Torr)

Fig. 11

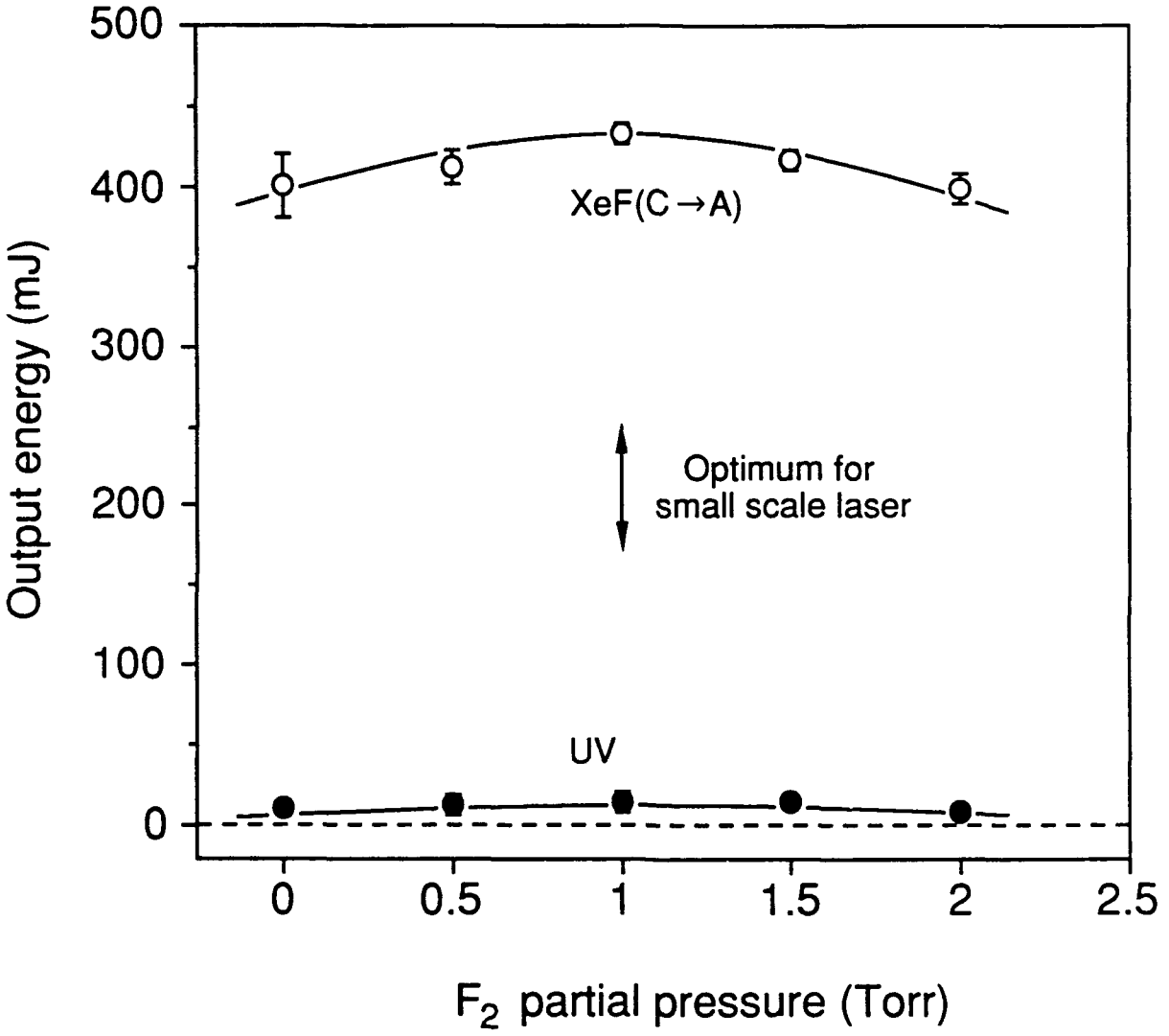
500
400
300
200
100
0
Output energy (mJ)
XeF(C→A)
Optimum for
small scale laser
UV
0
0.5
1
1.5
2
2.5
F2 partial pressure (Torr)

Fig. 12

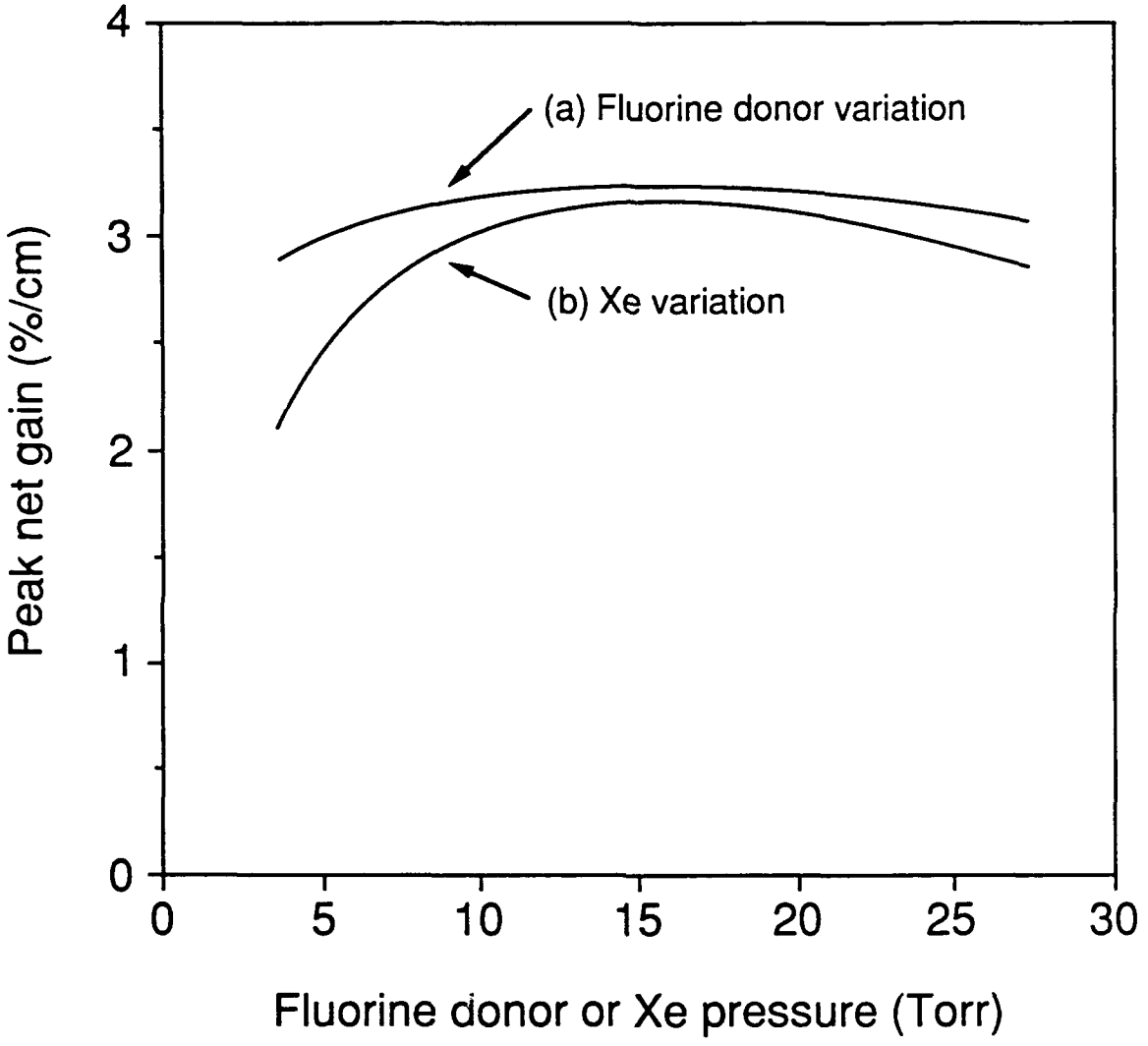
4
3
2
1
0
Peak net gain (%/cm)
(a) Fluorine donor variation
(b) Xe variation
0
5
10
15
20
25
30
Fluorine donor or Xe pressure (Torr)

Fig. 13

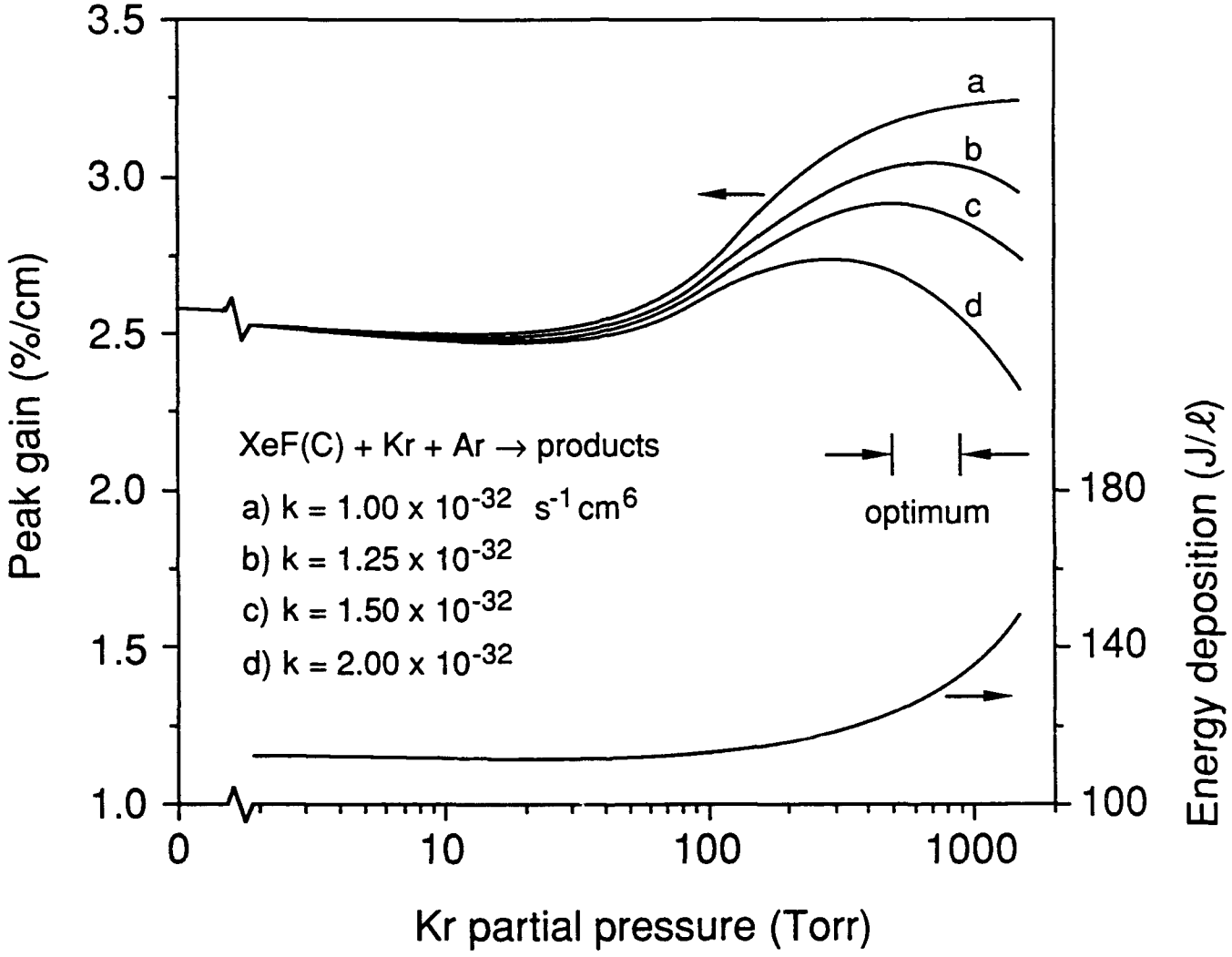
3.5
3.0
2.5
2.0
1.5
1.0
Peak gain (%/cm)
a
b
c
d
XeF(C) + Kr + Ar → products
a) k = 1.00 x 10-32 s-1 cm6
b) k = 1.25 x 10-32
c) k = 1.50 x 10-32
d) k = 2.00 x 10-32
optimum
180
140
100
Energy deposition (J/ℓ)
0
10
100
1000
Kr partial pressure (Torr)

Fig. 14

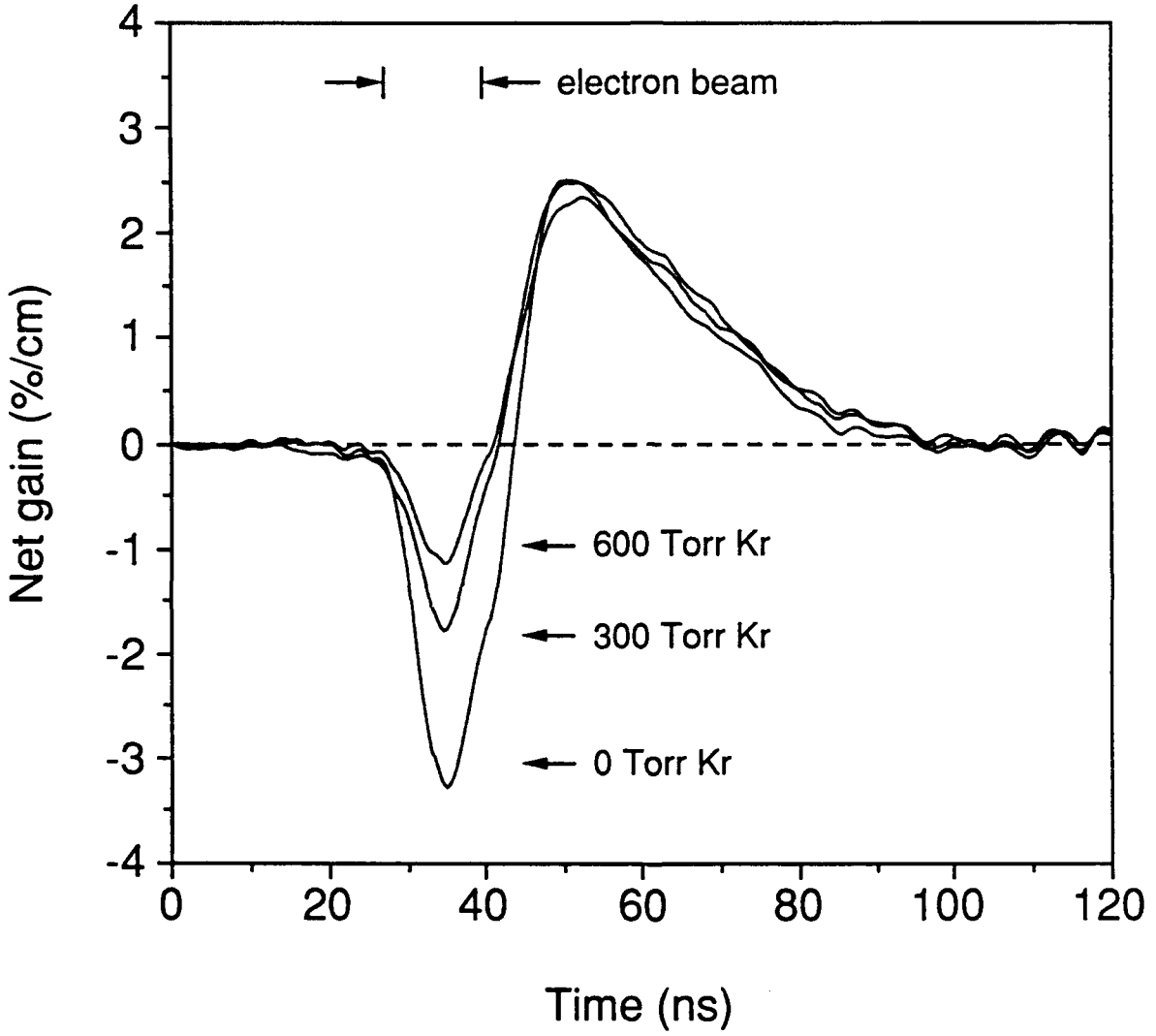
electron beam
600 Torr Kr
300 Torr Kr
0 Torr Kr
Net gain (%/cm)
Time (ns)
4
3
2
1
0
-1
-2
-3
-4
0
20
40
60
80
100
120

Fig. 15

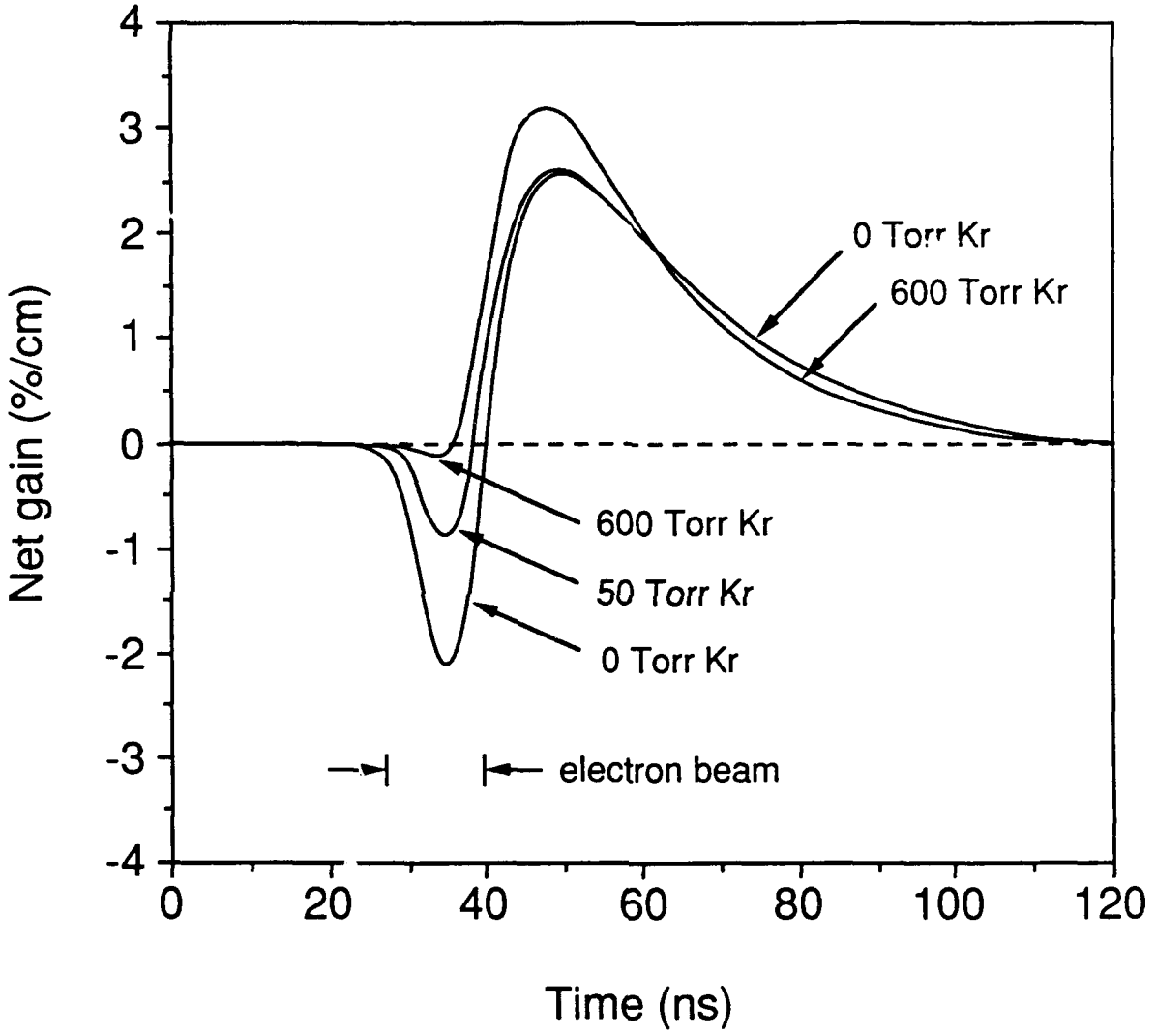
Net gain (%/cm)
Time (ns)
0 Torr Kr
600 Torr Kr
600 Torr Kr
50 Torr Kr
0 Torr Kr
electron beam
4
3
2
1
0
-1
-2
-3
-4
0
20
40
60
80
100
120

Fig. 16

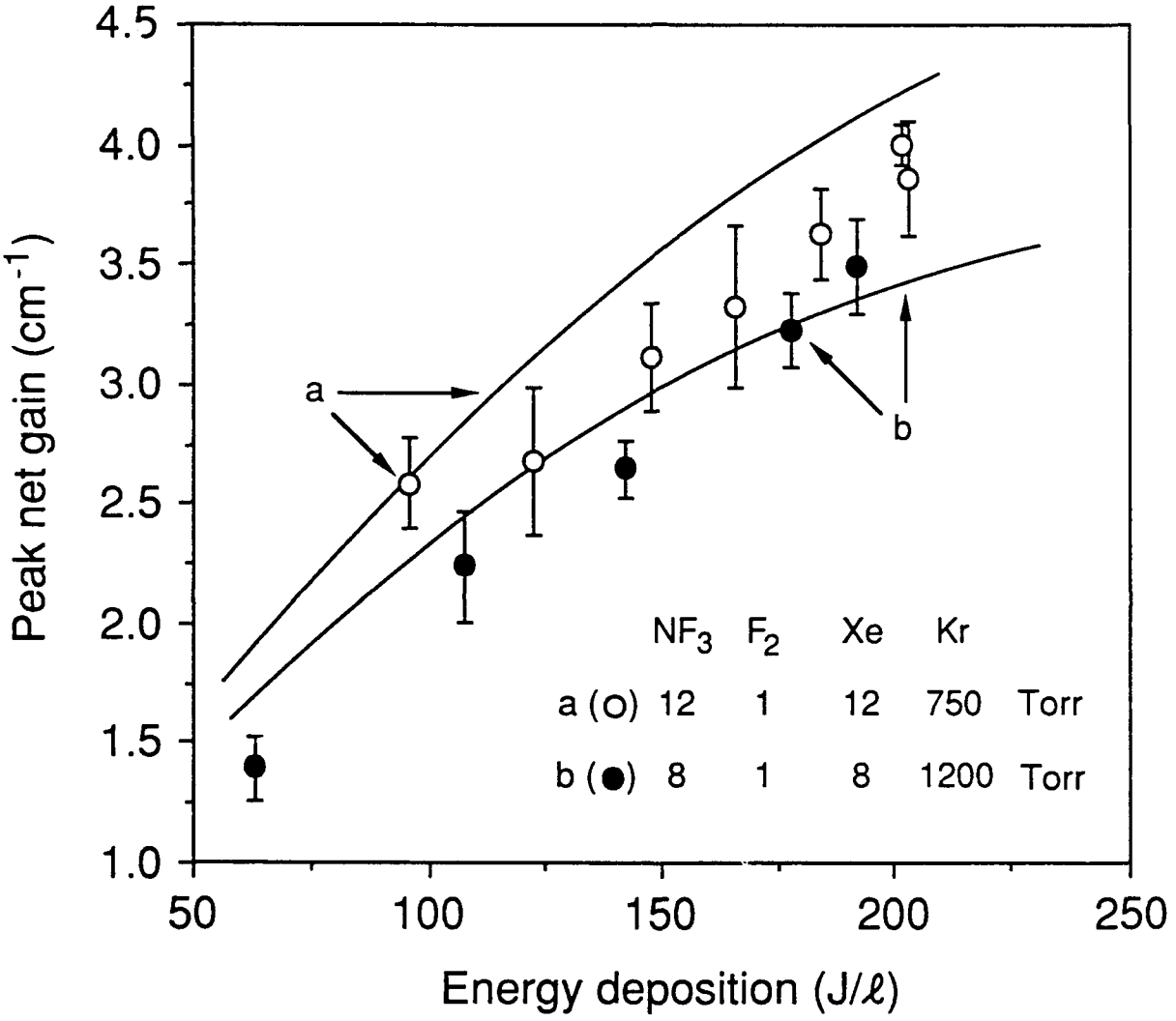
4.5
4.0
3.5
3.0
2.5
2.0
1.5
1.0
Peak net gain (cm^{-1})
50
100
150
200
250
Energy deposition (J/ℓ)
a
b
NF3 F2 Xe Kr
a (O) 12 1 12 750 Torr
b (●) 8 1 8 1200 Torr

Fig. 17

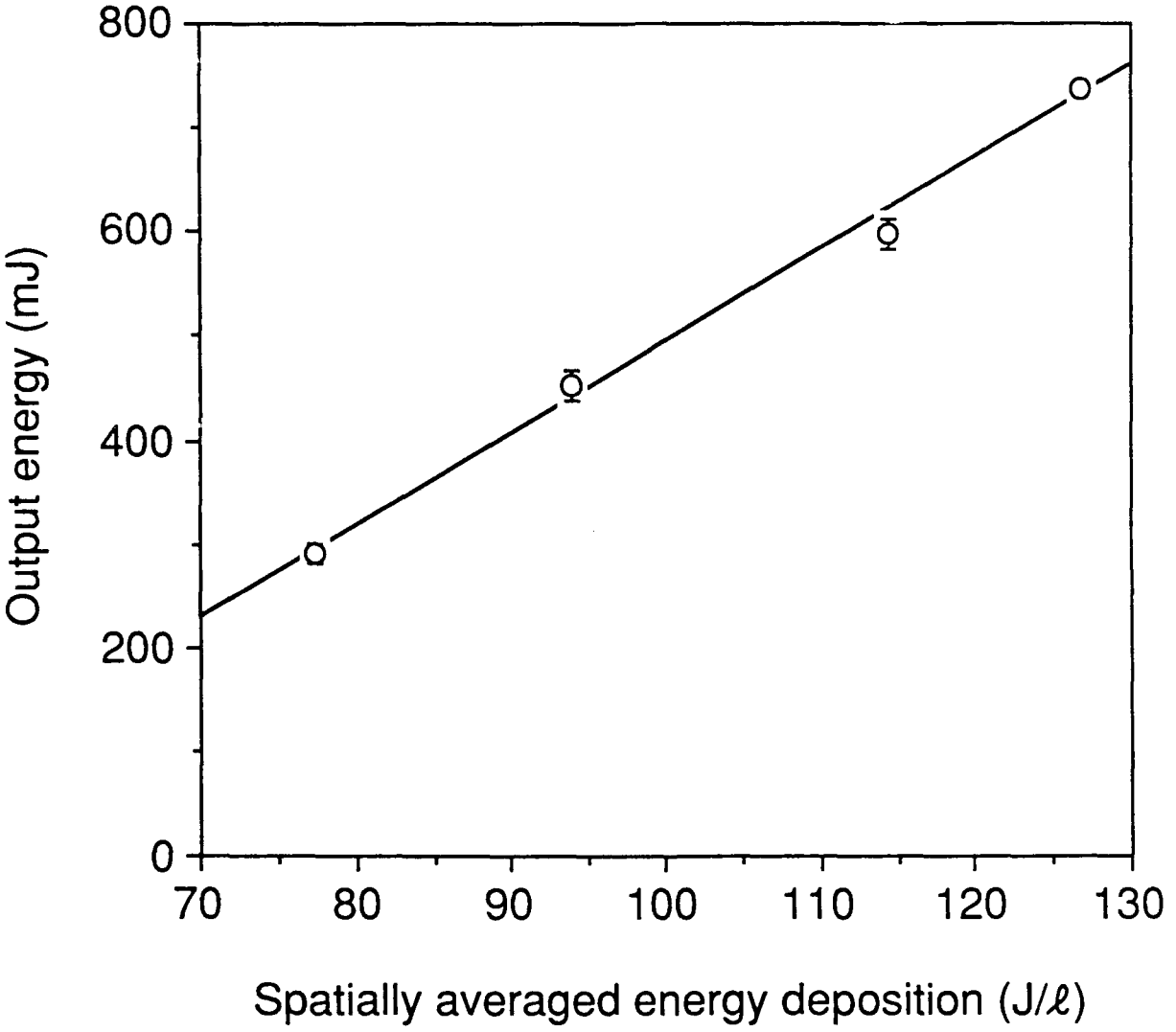
800
600
400
200
0
Output energy (mJ)
70
80
90
100
110
120
130
Spatially averaged energy deposition (J/ℓ)

Fig. 18

Kinetic Processes in Electron Beam-Excited XeF($C \rightarrow A$) Laser Media

WILLIAM L. NIGHAN, SENIOR MEMBER, AND MICHAEL C. FOWLER

Abstract—Fundamental processes affecting the operation and performance of electron beam-excited XeF($C \rightarrow A$) laser media have been analyzed and modeled. Emphasis has been placed on conditions typical of high current density (~ 250 A cm^{-2}), short pulse (~ 10 ns FWHM) e-beam excitation of high pressure (~ 6 atm) multicomponent mixtures comprised of Ar-Kr-Xe-NF_3-F_2. Computation of the temporal evolution of excited and ionized species for such circumstances has permitted identification of the factors controlling XeF(C) formation and loss, and has resulted in the identification of the primary transient species that absorb radiation in the blue-green spectral region. The data so obtained serve to explain measured XeF($C \rightarrow A$)properties, particularly net gain, under conditions for which the $C \rightarrow A$ laser energy density and efficiency values are comparable to those of the UV XeF($B \rightarrow X$) laser.

I. Introduction

OVER the past few years the performance of the electron beam-excited XeF($C \rightarrow A$) laser has improved significantly. The broadband $C \rightarrow A$ transition of XeF is centered at 480 nm in the blue-green region and, in marked contrast with the UV $B \rightarrow X$ transition, has a spectral width of nearly 100 nm. Thus, the XeF($C \rightarrow A$) laser has great potential as an optical source tunable over a broad bandwidth. Recently, extracted energy density and intrinsic efficiency values of 1-2 J/liter and 1-2 percent, respectively, have been demonstrated [1], [2] representing a level of performance approaching that typical of UV XeF($B \rightarrow X$) lasers [3], [4]. The improved XeF($C \rightarrow A$) laser performance results from the use of a high pressure (~ 6 atm) multicomponent gas mixture comprised of Ar-Kr-Xe-NF_3-F_2 [2] excited by a high current density (~ 250 A $\cdot$ cm^{-2}) electron beam of short temporal duration (~ 10 ns FWHM). For these conditions the ($C \rightarrow A$) gain has a maximum value of approximately 3 percent cm^{-1} and a duration of about 35 ns (FWHM) [1], [2], properties permitting efficient energy extraction using either a free running oscillator [1], or an injection controlled amplifier [2].

The multicomponent mixtures resulting in the best XeF($C \rightarrow A$) laser performance represent a particularly complex kinetics problem for a number of reasons. 1) Use of a high pressure, two-component buffer comprised of heavy rare gas species (Ar + Kr) introduces numerous reactions not usually important for rare gas halide $B \rightarrow X$ lasers, a circumstance exacerbated by weaknesses in the data base of fundamental reaction rate coefficients. 2) Because the stimulated emission cross section for the XeF $C \rightarrow A$ transition is ~ 30 times smaller than that of the $B \rightarrow X$ transition, transient absorption is of exceptional importance. Thus, identification and quantitative modeling of absorbing excited and ionized species is an even more compelling requirement than is the case for the $B \rightarrow X$ rare gas halide lasers. Additionally, consideration of XeF B and C state collisional transfer, and quantitative calculation of both state population densities is necessary.

In a prior work [5], a comprehensive spectroscopic investigation of XeF($C \rightarrow A$) laser mixtures was carried out, focusing particularly on the role of Kr. As part of that activity, a *qualitative* analysis of the effect of Kr on transient absorption and on XeF formation and loss was conducted. This paper reports the results of an analysis of XeF($C \rightarrow A$) laser medium properties in which the kinetics of the (Ar + Kr)-Xe-(NF_3 + F_2) mixture are modeled in detail. The pertinent features of the kinetics model are discussed in Section II, in which particular attention is focused on those aspects of the problem found to be of particular importance: 1) $Ar_2^+ \rightleftarrows Ar_3^+$ quasi-equilibrium reactions, 2) halogen-rare gas excited state reactions and products, 3) neutral reactions affecting the populations of high energy rare gas excited states, and 4) transient absorption in the blue-green spectral region. The properties of an XeF($C \rightarrow A$) gain medium excited by a high current density electron beam of short duration are presented in Section III where a comparison is made with experimental results. Therein, factors controlling *net* gain on the $C \rightarrow A$ transition are emphasized, and the effects of Kr and the processes dominating XeF formation and loss are discussed. Additionally, Section III presents a brief discussion of XeF($C \rightarrow A$) gain medium properties when the excitation is provided by a low current density electron-beam pulse having a temporal duration on the order of 1 μs.

II. Kinetics

Over the past ten years kinetic processes controlling the rare gas halide population in laser media have been the subject of considerable attention. Consequently, *relatively* complete rate coefficient data are available for most processes of importance to the present investigation, including:

Manuscript received June 20, 1988, revised October 27, 1988. This work was supported by the Office of Naval Research.

The authors are with United Technologies Research Center, East Hartford, CT 06108.

IEEE Log Number 8826297.

0018-9197/89/0400-0791$01.00 © 1989 IEEE

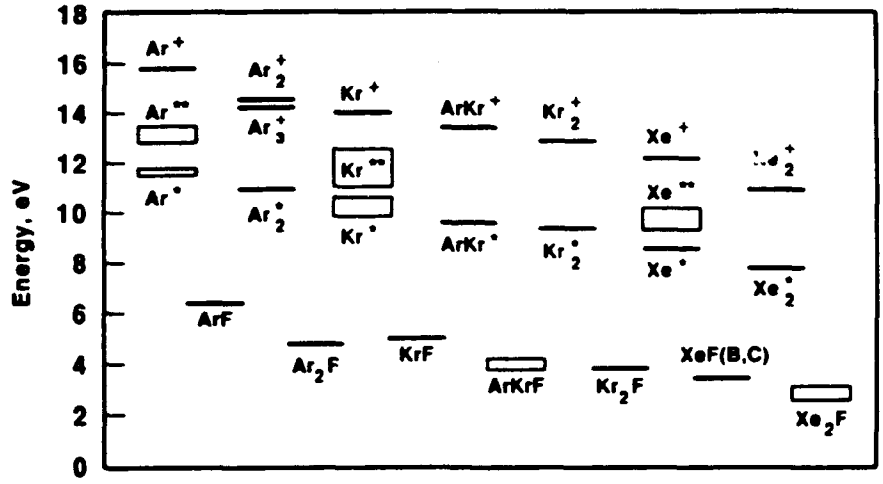

Fig. 1. Ionized and excited species which, along with electrons, F^-, and the neutral halogens, are considered in the XeF($C \rightarrow A$) laser model.

1) XeF(B, C) formation processes such as positive ion–negative ion recombination [6]–[8] and halogen reactive quenching of rare gas *metastable* states [9], [10];

2) mixing and quenching of low vibrational levels of the XeF B and C states [11], [12];

3) two-body [13], [14] and three-body [15]–[17] rare gas molecular ion charge exchange and rearrangement [18];

4) excited state processes in rare gases and their mixtures [19]–[21];

5) electron-halogen dissociative attachment [22]; and dissociative electron-ion recombination [23]–[25].

The body of data for these and related processes continues to grow, albeit slowly, in response to the importance of rare gas-halide lasers and other similar applications. In the present investigation, data from such sources [6]–[25] have been used in a self-consistent model of XeF(B, C) processes for the experimental conditions described in our previous work [2], [5]. Analytical and numerical procedures of the type untilized are well developed [26]–[29]. Thus, the discussion to follow will concentrate only on those aspects of the kinetics and modeling having special significance in the present context, with little emphasis on general methods and procedures, and/or on processes that are well understood for which data are readily available in the literature.

A. Ionized and Excited Species

Presented in Fig. 1 are the energy-ordered positive ions and excited species that, on the basis of our prior investigations, we conclude are important to the problem at hand. The indicated species, along with electrons F^- and the neutral halogens, comprise the present model. We compute the temporal evolution of the concentrations of the indicated species in response to high current density (~ 250 A $\cdot$ cm^{-2}) e-beam excitation (~ 10 ns FWHM) of a gas mixture typically comprised of Ar(6.1 atm) - Kr(300 Torr) -Xe(8 Torr) -NF_3(8 Torr) -F_2(1 Torr). These mixture conditions have been found to be optimum for the XeF($C \rightarrow A$) laser e-beam excitation scheme utilized, and result in an energy deposition of 100-150 J/liter in the optically active region [2].

The rare gas excited states are represented as two groups of coupled levels (Fig. 1); RG* referring to the lowest energy s states (e.g., Ar($4s$, $4s'$), and RG** referring to all higher energy states, but primarily the p states [e.g., Ar($4p$)]. The "boxes" in Fig. 1 indicate the approximate energy spread of the four low lying s states and several of the lowest energy p states. Specific details of rare gas excited state reactions are discussed in a section to follow.

B. Positive Ion Kinetics

1) $Ar_2^+ \rightleftarrows Ar_3^+$ Quasi-Equilibrium: Electron beam excitation of laser mixtures using several atmospheres of argon as the buffer result in the production of Ar^+ which is converted to Ar_2^+ on a subnanosecond time scale, the latter usually thought to be the only argon molecular ion of consequence. However, for pressures ≥ 1 atm formation of the weakly bound ($D_e \sim 0.2$ eV) trimer ion Ar_3^+ [30] becomes appreciable, and its effect can be significant as regards photo-absorption in XeF($C \rightarrow A$) laser media [31]. In this work, we have used the $Ar_2^+ \rightleftarrows Ar_3^+$ forward and reverse rate coefficients reported by Turner and Conway [32]. Those data indicate that for a pressure of only *one* atmosphere at equilibrium, approximately 20 percent of the Ar_2^+ ions are converted to Ar_3^+. Here we are interested in pressures of ~ 6 atm.

Based on the work of MacDonald, Biondi, and Johnsen [33], showing that the rate coefficient for electron recombination with Ne_3^+ is five times larger than that of Ne_2^+, we have assumed that the electron recombination coefficients for Ar_2^+ [23] and Ar_3^+ are in the same ratio. As regards the more important charge transfer and positive ion-negative ion recombination reactions, there are no data available for Ar_3^+. For that reason we have assumed that the rate coefficients for Ar_3^+ are the same as those for Ar_2^+.

2) Charge Exchange: The two-body charge exchange ractions $Ar_2^+ + Kr \rightarrow Kr^+ + 2Ar$, and $Ar_2^+ + Xe \rightarrow Xe^+ + 2Ar$ are very important for the XeF($C \rightarrow A$) mixtures

under consideration. The rate coefficients for these reactions are large ($\sim 5 \rightarrow 10 \times 10^{-10}$ s^{-1} cm^3), [13], [14]. In addition, rate coefficients for the *termolecular* reactions $Ar_2^+ + Kr + M \rightarrow$ products, and $Ar_2^+ + Xe + M \rightarrow$ products have been found to be $\geq 10^{-30}$ s^{-1} cm^6 [15]. Thus, for pressures typical of rare gas halide lasers, the *effective* two-body rate coefficients for the indicated three body reactions are comparable to those of the corresponding two-body charge exchange reactions. The effect of such termolecular reactions is not usually considered in rare gas halide laser modeling.

Unfortunately, the products of the indicated termolecular reactions have not been identified. In the present paper, we have assumed that the *products* of the two- and three-body molecular ion reactions are the same, and that the corresponding rate coefficients for Kr molecular ions, for which there are little or no data, are the same as the corresponding Ar molecular ion reactions.

The dominant processes affecting $Ar_2^+ \rightleftarrows Ar_3^+$ quasi-equilibrium and related Ar molecular ion reactions are summarized in Table I along with the corresponding rate coefficients used in our model.

TABLE I
ARGON MOLECULAR ION PROCESSES

Reaction[a]	Rate Coefficient[b]	Reference
1) $Ar_2^+ + 2Ar \leftrightarrows Ar_3^+ + Ar$	7.0(−32), 9.0(−12)	32
2) $Ar_2^+ + e \rightarrow Ar^{**} + Ar$	6.5(−8)	23
3) $Ar_3^+ + e \rightarrow Ar^{**} + 2Ar$	3.25(−7)	see text
4) $Ar_2^+ + F^- \rightarrow ArF + Ar$	1.5(−6)	7, 8
5) $Ar_2^+ + Kr \rightarrow Kr^+ + 2Ar$	7.5(−10)	13
6) $Ar_2^+ + Kr + Ar \rightarrow Kr^+ + 3Ar$	1.7(−30)	15
7) $Ar_2^+ + Xe \rightarrow Xe^+ + 2Ar$	7.5(−10)	14, 15
8) $Ar_2^+ + Xe + Ar \rightarrow Xe^+ + 2Ar$	5.0(−30)	15

[a]For the Ar_3^+ reactions corresponding to 4 → 8 the indicated Ar_2^+ rate coefficients were used.
[b]The units for two-body and three-body rate coefficients are s^{-1} cm^3 and s^{-1} cm^6, respectively.

C. Halogen Kinetics

1) Dissociative Attachment: It has been shown that use of an optimized combination of NF_3 and F_2 results in XeF($C \rightarrow A$) laser performance that is better than that obtained using either F_2 or NF_3 individually [1], [5], [34]. Since the rate coefficients for electron dissociative attachment of NF_3 and F_2 differ significantly, each exhibiting a strong dependence on electron energy [22], combination of these two chemically compatible fluorine donors permits optimization of the attachment process (F^- production) over a broad range of electron energy, and also provides an added degree of control over the electron density.

Presented in Fig. 2 are the electron rate coefficients for dissociative attachment of NF_3 and F_2; F^- is the negative ion product in both cases [22]. Also, shown for comparison is the *effective* rate coefficient for mixtures of NF_3 and F_2 combined in the ratios 8:1 and 4:1. During the *e*-beam excitation pulse (10 ns for the conditions of present interest) the secondary electron energy is a few eV, relaxing rapidly toward the translational temperature of the neutrals upon termination of the *e* beam [35], [36]. The data of Fig. 2 show that for certain NF_3-F_2 combinations the effective attachment coefficient for the mixture is large ($> 10^{-9}$ s^{-1} cm^3) over the entire energy range of the secondary (i.e., low energy) electrons produced by the electron beam. Therefore, since dissociative attachment results in production of F^- and loss of electrons, the production of F^-, a primary XeF precursor, and the loss of electrons, which quench XeF, will both be large and essentially independent of electron energy throughout the temporal duration of the *e*-beam excitation pulse (~ 10 nsec FWHM) and the much longer afterglow (~ 50–100 ns), [2], [5], [31].

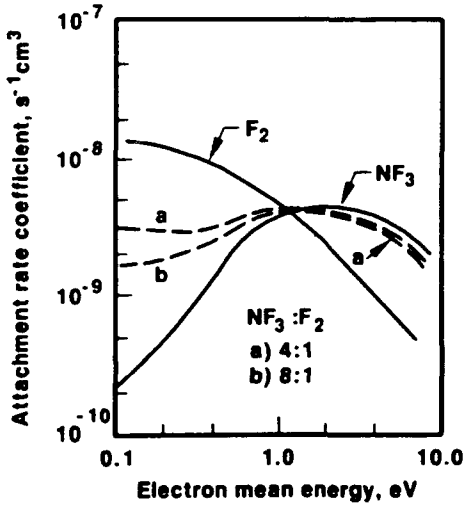

Fig. 2. Rate coefficients for electron dissociative attachment of NF_3 and F_2 adapted from the work of Chantry [22]. Also shown are the *effective* rate coefficients for NF_3 and F_2 mixtures having the indicated NF_3:F_2 proportions.

2) Reactive Quenching: The reactive quenching of rare gas excited states by NF_3 and F_2 and the branching to XeF are of particular importance. The rate coefficients and branching fractions for the rare gas *metastable* levels have been measured for practically all useful rare gas halide halogen donors [10]. The data obtained for the metastable levels are usually used in the modeling of *higher energy* rare gas excited states. However, the measurements of Ku and Setser [37] show that the halogen quenching rate coefficients for the Xe(6*p*) states are significantly *larger* than for the Xe(6*s*) *metastable* state, and that the differences between the individual levels of the Xe(6*p*) manifold are also large. Table II shows an adaptation of the NF_3 and F_2 data of Ku and Setser, for which we have averaged their measurements of the individual Xe(6*p*) levels. The average rate constant for Xe(6*p*) quenching by NF_3 is about an *order-of-magnitude* larger than that for Xe(6*s*). Even the rate constant for F_2 as the reagent is increased by nearly 30 percent.

In our modeling we have used the data of Table II and have assumed that the NF_3 and F_2 quenching rate constants of the higher excited states of *argon* and *krypton* (Ar** and Kr** in Figs. 1 and 3) are larger than those of the metastable levels of those species by the same factors indicated by the Xe data of Table II.

TABLE II
TOTAL QUENCHING RATE CONSTANTS AND XeF BRANCHING FRACTIONS

	Xe**		Xe***	
	k_Q[b]	Γ_{XeF}	k_Q[b]	Γ_{XeF}
NF_3	0.9(−10)	0.27	8.9(−10)	0.35
F_2	7.5(−10)	1.0	9.6(−10)	1.0

[a]Xe* and Xe** refer to the species designations shown in Figs. 1 and 3 and described in Section II-D.

[b]The rate constants (units of s^{-1} cm^3) and branching fractions indicated for Xe* refer to values measured for the Xe(6s[3/2]$_2$) metastable state [9], [10], while those shown for Xe** are averages of values measured for the Xe 6p[1/2]$_0$, 6p[3/2]$_2$ and 6p[5/2]$_2$ states as reported in [37]. The relative differences between the Xe* and Xe** rate coefficients and branching fractions for NF_3 and F_2 as the reagents were applied to the corresponding reactions involving Ar and Kr excited states.

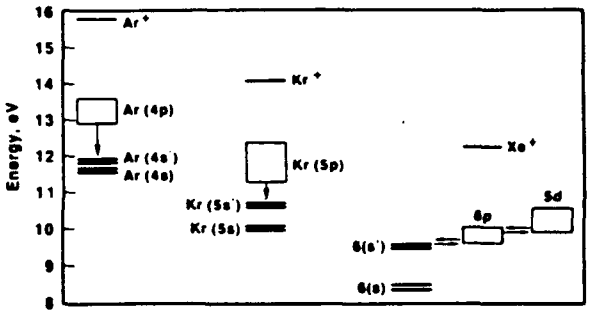

Fig. 3. Rare gas excited states considered in the present model. In this work the designation Ar* and Kr* refers to the indicated s and s', states while Ar** and Kr** refer to the p and higher energy states. In contrast, Xe* refers only to the Xe(6s) states, while Xe** refers to the coupled 6s', 6p, and 5d (and higher energy) states as described in the text.

D. RG*-RG** Kinetics

In addition to their role as rare gas-halide precursors, the higher excited rare gas states exhibit broad-band absorption extending throughout the UV/visible spectral region [38]. Knowledge and control of broad-band transient absorption is important for $B \rightarrow X$ rare gas halide laser applications, and is absolutely essential for the XeF($C \rightarrow A$) laser which typically will have a smaller gain.

1) Ar and Kr Excited States: Fig. 3 shows in more detail those elements of Fig. 1 relevant to the present treatment of RG*-RG** kinetics. In our model we consider Ar* to be comprised of the four Ar 4s and 4s' states, and Kr* to be comprised of the corresponding Kr 5s and 5s' states. The species designation Ar** refers to ten Ar 4p levels, the energy range of which is illustrated by the box in Fig. 3, and all higher energy argon excited states. For the pressures of interest (6 atm), the latter can be expected to relax to the Ar p-state manifold with a subnanosecond time constant. The species Kr** is defined in a similar way, and the statements made about Ar are also applicable.

When e-beam excitation is used the energy flow is, for the most part, downward toward the p states; and the collisional coupling between the p and s manifolds becomes an important issue, particularly as regards transient absorption by the p states [31]. While there is considerable energy overlap among the higher energy rare gas excited states, a factor facilitating relaxation, the energy gap between p and s' states is rather large, i.e., ~1 eV, for Ar and ~0.5 eV for Kr (Fig. 3). Nevertheless, Setser and co-workers have shown for Ar and Kr that $p \rightarrow s$ intermultiplet relaxation proceeds at a rapid rate by way of complex mechanisms involving curve crossings, in which attractive bound RG_2^{**} potential curves from RG(p) and RG interact with the repulsive curves from RG(s') and RG and RG(s) and RG [39], [40].

This sequence of events is illustrated in simplified form by Fig. 4. For Ar, the *average* two body rate coefficient for intermultiplet relaxation between the ten p levels and s', s (Ar** → Ar*, Fig. 3) is ~3 × 10^{-11} s^{-1} cm^3, with practically all Ar(4p) levels participating [39]. Relaxation of the Kr(5p) manifold in Ar proceeds in the same general way, except that quenching of ony a few low energy levels of Kr(5p), particularly $2p_{10}$, results in intermultiplet transfer to Kr(5s', 5s) [40]. Since our treatment of Kr** refers to the entire Kr (5p) manifold (and higher energy states as well), we have used a level-weighted value of 2.0 × 10^{-11} s^{-1} cm^3 for Kr** → Kr* two body quenching, a value significantly less than the 1.2 × 10^{-10} s^{-1} cm^3 measured for the Kr($2p_{10}$) level alone. Thus, for either Ar** or Kr** relaxing to Ar* or Kr* in an Ar buffer at a pressure of several atm, the time constant is ≤ 1 ns.

2) Xe Excited States: Xenon excited state relaxation differs from that of either Ar or Kr, and we believe substantially so. The illustration of Fig. 4 indicates that two-body relaxation of RG(p) results in the formation of RG(s') rather than RG(s). As far as Ar and Kr are concerned, it doesn't matter whether the s' or s state is the exit channel for p state relaxation (Fig. 4), because both the s' and s levels lie ≥ 0.5 eV below the $2p_{10}$ level of the p state manifold. Thus, once relaxation has occurred the p states cannot be repopulated by neutral collisions. However, in Xe the upper 6s' level ($1s_2$) is nearly coincident in energy with the $2p_{10}$ level of the p state manifold. Experimental evidence [41]–[43] indicates that the primary product of intermultiplet relaxation of the Xe($2p_5 \rightarrow 2p_{10}$) levels is Xe(6s', i.e., $1s_2$ and $1s_3$), as illustrated in Fig. 4, with little or no coupling to the low lying Xe(6s) states. The energy coincidence of Xe(6s') and lower Xe(6p) levels, combined with the energy overlap between the Xe(6p) and Xe(5d) manifolds, results in an energy pool, the levels of which can be mixed by neutral collisions. For this reason, the relaxation mechanism that effectively depopulates the p (and higher) states of Ar and Kr (Fig. 4), is relatively ineffective at collisional deactivation of the coupled Xe 6s', 6p, and 5d energy reservoir. The result is that the concentration of higher energy Xe excited states is much larger and longer lived than is typical of either Ar or Kr under similar circumstances, the consequences of which have been discussed in detail previously [31] and will be summarized in subsequent paragraphs.

For these reasons, in the present model we take Xe* to mean the two 6s levels, with Xe** referring to the collisionally coupled 6s', 6p, and 5d manifolds of states. Reflecting this grouping of excited states, we assume that Xe** is *not* coupled to Xe* by collisions with neutrals (i.e., Ar).

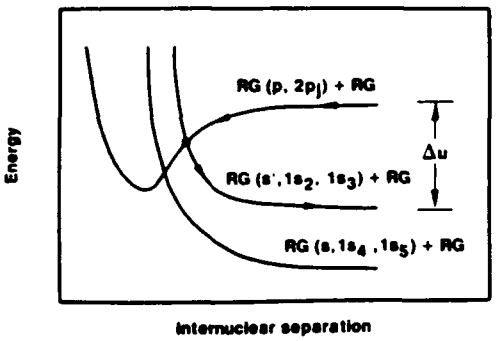

Fig. 4. Potential energy diagram illustrating two-body rare gas $p \rightarrow s'$ collisional deactivation, where RG refers to Ar, Kr, or Xe.

The dominant collision processes coupling RG** and RG* are summarized in Table III along with corresponding rate coefficients.

TABLE III
RG* ⇆ RG** PROCESSES

Reaction	Rate Coefficient[a]	Reference
1) Ar** + Ar → Ar* + Ar	3.0(−11)	39
2) Kr** + Ar → Kr* + Ar	2.0(−11)	40
3) Xe** + Ar → Xe* + Ar	nil	see text
4) RG** → RG* + hν	3.0(7)	39–42
5) RG* + e → RG** + e	5.0(−7)	26
6) RG** + e → RG* + e	1.4(−6)	26

[a]The units for two-body rate coefficients are s^{-1} cm^3 and for radiative transitions the units are s^{-1}.

E. Broad-band and Absorption

It is well known that broad-band transient absorption has a significant adverse effect on the optical extraction efficiency of the UV rare gas halide $B \rightarrow X$ lasers, usually limiting extraction efficiency to a value ≤ 50 percent of the intrinsic rare gas halide formation efficiency. For the XeF($C \rightarrow A$) laser, absorption is an even more important issue because the stimulated emission cross section for the $C \rightarrow A$ transition is approximately thirty times smaller than that of the $B \rightarrow X$ transistion. Thus, transient absorption can be of the same order as the gain resulting from the XeF(C) molecule, with the result that the *net* gain usually is significantly less than the simple product of the $C \rightarrow A$ gain cross section and the C state population [31]. Indeed, identification of the transient species absorbing in the blue-green spectral region and control of their concentration by way of mixture optimization are responsible for the dramatic improvement in XeF($C \rightarrow A$) laser performance [1], [2], [5], [31], [34].

1) UV/Visible Photoabsorption Cross Sections: Presented in Fig. 5 are the *broad-band* absorption cross sections [38], [44], [45], [46], [47], [48] for the species known to be important absorbers of and visible radiation for rare gas halide laser conditions. Also, shown for comparison are the stimulated emission cross sections for the $B \rightarrow X$ transitions of KrF and XeF and the XeF($C \rightarrow A$) transition [49].

Fig. 5 shows that broad-band absorption in the UV region is more complex than in the blue-green region, largely a reflection of the higher photon energy. Of significance is the fact that photoionization of the rare gas excited states [38] (our RG** species, Fig. 1) is important throughout the entire UV/visible spectral region. That process will be shown to dominate transient absorption for the XeF($C \rightarrow A$) laser conditions under investigation. Also of importance is the fact that the recently measured [44] Kr_2F absorption cross section has a magnitude and shape very different from that of Kr_2^+ [45], contrary to earlier expectations [50]. Evidence of an Ar_2F absorption cross section much less than Ar_2^+ is also becoming available; there are no data available for ArKrF. The concentrations of such rare gas halide trimers can be very large

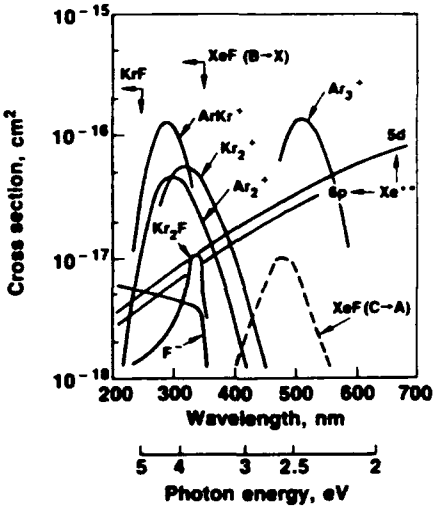

Fig. 5. Photoabsorption cross sections for species known to be broadband transient absorbers for typical rare gas halide laser conditions: Xe** [38]; Kr_2F [44]; Ar_2^+ and Kr_2^+ [45]; $ArKr^+$ [46]; Ar_3^+ [47]; F^- [48]. The photoabsorption cross sections for Ar** and Kr** [38] are not shown for the sake of clarity, but are very similar to those of Xe**. Also shown for comparison are the stimulated emission cross sections for the $B \rightarrow X$ transition of KrF and for the XeF($C \rightarrow A$) transition [49].

for XeF($C \rightarrow A$) laser conditions. Except for Kr_2F, they do not affect the $C \rightarrow A$ laser directly; but their presence can have a very significant effect on gain in the UV [5].

2) Ar_3^+ photoabsorption: Recently Lineberger and coworkers [47] measured the magnitude and spectral shape of the Ar_3^+ photoabsorption cross section (Fig. 5). Over the 440–520 nm effective tuning range [2] of the $C \rightarrow A$ laser, the measured Ar_3^+ photoabsorption cross section is very large, confirming our earlier conclusion [31] that Ar_3^+ is an important absorber in Ar-buffered XeF($C \rightarrow A$) laser mixtures *not* containing Kr.

3) Absorber Bleaching in the Blue-Green Region: It is important to note that because the blue-green photoabsorption cross sections for the primary absorbing species are significantly larger than the XeF($C \rightarrow A$) stimulated emission cross section (Fig. 5), the saturation fluxes for broadband transient absorbers such as Ar**, Kr**, and particularly Xe**, are comparable to those of the $C \rightarrow A$ laser transition, in striking contrast to the situation typical of the $B \rightarrow X$ lasers. Thus, optical bleaching of transient absorption can be significant in XeF($C \rightarrow A$) lasers [31], [51], particularly when the laser is tuned off the peak of the gain cross section or at wavelengths for which narrow discrete absorption is known to occur [2]. We are unaware

of any significant nonsaturable absorption in the blue-green region under the conditions for which good XeF ($C \rightarrow A$) laser performance has been obtained. Thus, although the low $C \rightarrow A$ gain cross section results in a lower net gain than is possible for the $B \rightarrow X$ transitions, higher energy extraction efficiency may be possible for optimized XeF($C \rightarrow A$) lasers.

III. XeF($C \rightarrow A$) Laser Medium Properties

As mentioned previously, the primary focus of our analysis is short pulse (10 ns FWHM), electron-beam excitation of high pressure multicomponent XeF($C \rightarrow A$) laser mixtures. Specific experimental conditions and a complete description of the laser cell used are reported elsewhere [2]. For those conditions, the energy deposition on the optical axis was on in the 100–150 J/liter range (~ 12.5 MW cm^{-3}). To first order the energy deposition is proportional to the Ar pressure. Since the gain is sensitive to energy deposition, changes in the Ar pressure are very significant. With the Ar pressure fixed at ~ 6 atm, the other constituent fractions have been optimized to maximize the gain. However, *both* experiment and theory show that the following constituent variations have only a small effect on the gain and laser performance: Kr-300 Torr ± 75 Torr; Xe-8 Torr ± 2 Torr; NF_3-8 Torr ± 4 Torr; F_2-1 Torr ± 0.5 Torr. Although the following discussion will focus on the specific mixture of [2], the indicated allowable variations should be understood.

A. Species Concentrations

Presented in Figs. 6–8 is the computed temporal variation of selected species concentrations. The rare gas species Ar**, Kr**, and Xe** (Fig. 6) will be shown to be the dominant source of broadband absorption in the blue-green region. Each of these species contributes significantly to absorption during the *e*-beam excitation pulse, but Xe** absorption persists for a much longer time reflecting the relatively long time required for collisional deactivation of Xe** as described in Section II-D.

As expected, the XeF(C) population (Fig. 7) is the largest by far and, were it not for absorption, would result in a gain of about 4 percent cm^{-1} for a wavelength of ~ 480 nm at the $\sim 10^{-17}$ cm^2 maximum of the $C \rightarrow A$ gain cross section [49], (Fig. 5). The KrF and XeF(B) populations are also substantial for a short time, and the computed peak gain at 248 nm and 351/353 nm is on the order of a few percent per cm. Indeed, relatively *efficient* simultaneous laser oscillation on the $B \rightarrow X$ and $C \rightarrow A$ transitions of XeF has been demonstrated for a gas mixture similar to that of Fig. 6 using a special cavity design [5].

1) Kr_2F: Of the rare gas halide trimers shown in Fig. 8, the populations of ArKrF and Kr_2F are very high, particularly the latter. In fact, except for the presence of Xe, the mixture conditions of Fig. 8 are very close to those found to be optimum for Kr_2 F laser oscillation [52]. The presence of the Kr_2F trimer causes significant absorption at ~ 350 nm and, along with Kr** and Kr_2^+ (Fig. 5), tends to suppress oscillation on the XeF($B \rightarrow X$) transition [5]. In addition, Xe has been shown to be a very strong

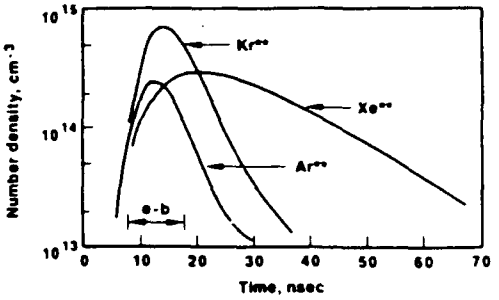

Fig. 6. Computed temporal variation of Ar**, Kr**, and Xe** for a mixture comprised of Ar(6 atm)-Kr(300 Torr)-Xe(8 Torr)-NF_3(8 Torr)-F_2(1 Torr), excited by a ~ 1 MeV electron beam pulse having a duration of 10 nsec (FWHM) and a peak current density of ~ 250 Acm^{-2}. For these conditions the volumetric energy deposition is ~ 130 J/liter (13 MWcm^{-3}).

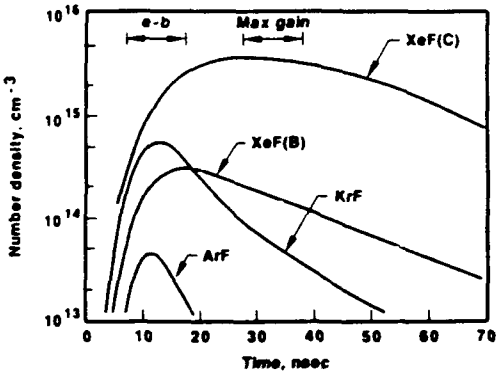

Fig. 7. Computed temporal variation of ArF, KrF, XeF(B) and XeF(C) for the conditions of Fig. 6. The temporal region of maximum XeF(C → A) net gain is indicated.

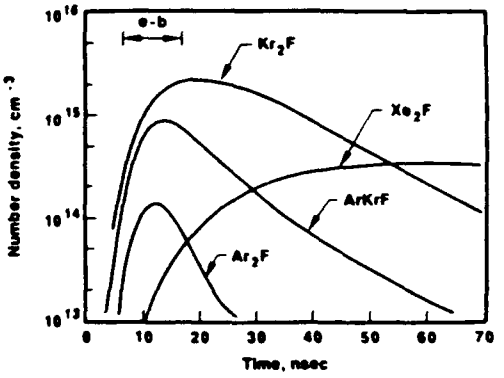

Fig. 8. Computed temporal variation of Ar_2F, ArKrF, Kr_2F, and Xe_2F for the conditions of Fig. 6.

quencher of Kr_2F [5]. Based on our analysis of the dependence of the Kr_2F and XeF($C \rightarrow A$) fluorescence as Xe is added to the mixture, we infer a rate coefficient of $\sim 4.5 \times 10^{-10}$ s^{-1} cm^3 for the reaction, $Kr_2F + Xe \rightarrow XeF(B, C) + 2Kr$. Because of the limited energy available (Fig. 1), XeF sc formed must be in a very low vibrational levels, in contrast to ion-ion recombination and harpooning reactions which result in rare gas halides in very high vibrational levels.

B. XeF($C \rightarrow A$) Net Gain

Presented in Fig. 9 are the measured [2] and computed $C \rightarrow A$ net gain at ~ 480 nm. The gain measurement is a

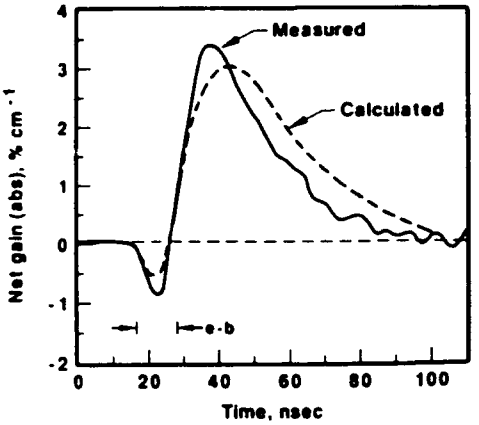

Fig. 9. Measured [2] and computed XeF(C → A) net gain at −480 nm, a wavelength corresponding to the maximum in the $C \rightarrow A$ gain cross section (Fig. 5). Measurements of e-beam energy deposition show it to be nonuniform along the optical axis, having a maximum value in the center of ~150 J/liter and an average value of ~100 J/liter [2]. As described in the text, analysis of the net gain measurement for these conditions shows that the *effective* energy deposition for a uniform medium would be ~130 J/liter. For this reason the comparison was made for the conditions of Fig. 6 (~130 J/liter deposited energy).

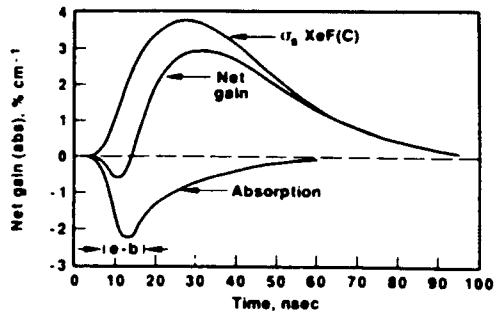

Fig. 10. Computed net gain profile of Fig. 9, along with the individual contributions of XeF(C) and the total transient absorption.

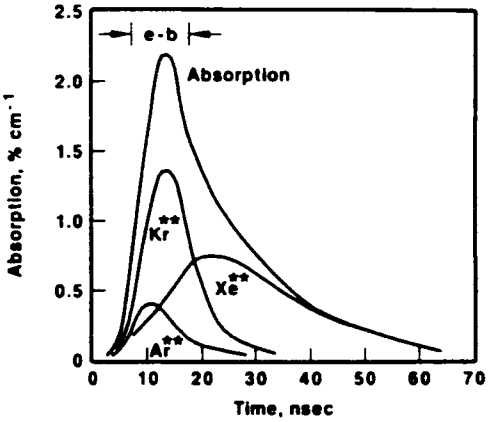

Fig. 11. Primary individual contributions to the transient absorption for the conditions of Figs. 9 and 10.

spatial average of a double pass through a 10 cm long medium. Measurements of the e-beam energy deposition show it to be nonuniform [2], having a maximum value of ~150 J/liter in the center of the active region, tapering off in each direction along with the optical axis. We have computed the gain as a function of energy deposition (position) along the optical axis and have analyzed the effect of the gain spatial nonuniformity on the measured *average* gain. The aveage value so measured corresponds to a uniform *effective* energy deposition value of ~130 J/liter, and the *computed* gain curve shown in Fig. 9 corresponds to that value. Considering the complexity of both the measurement and the kinetics model, the agreement between the measured and computed gain is considered to be good.

1) Broad-band Transient Absorption: Presented in Fig. 10 is the computed net gain of Fig. 9, along with the individual contributions of XeF(C) and the total broadband transient absorption. During the period of initial absorption (~5-15 ns) both the XeF(C) gain and the transient absorption are comparable in magnitude and are significantly larger than the actual net *absorption*. Obviously, in that temporal region the demands on the accuracy of the kinetics model are severe as regards quantitative computation of the net absorption. After termination of the e-beam the absorption decays while the XeF(C) population continues to rise. In the temporal region for which the net gain maximum occurs, the XeF(C) contribution is ~6 times larger than the broadband absorption.

2) Rare Gas Excited State Absorption: Fig. 11 shows the individual contributions to the broad-band transient absorption at 480 nm. For these conditions our analysis indicates that the absorption in the blue-green region is dominated by photoionization [38] of the rare gas excited states Ar**, Kr**, Xe**, the modeling of which is described in Section II-D.

XeF($C \rightarrow A$) laser spectra always exhibit evidence of very narrow discrete absorption [2] attributable to bound-bound phototransitions between low energy rare gas excited states and Rydberg levels. Cross sections for these processes are not known. However, except when tuning the laser to a specific wavelength corresponding to a Rydberg transition, discrete absorption is insignificant compared to broadband transient absorption. Thus, in the present analysis only broad-band transient absorption processes have been considered.

3) Wavelength Dependence of Peak Gain: By far the most unique feature of the XeF($C \rightarrow A$) laser is its potential for continuous, broadband tunability. Indeed, this laser is the only UV/visible gas laser that is broadly tunable and scalable. Fig. 12 shows the computed wavelength dependence of the maximum gain. Also shown for comparison are experimental data [53] obtained under similar but somewhat different conditions than those of Fig. 9. The data points shown correspond to wavelengths for which discrete absorption does *not* occur. Thus, the measured wavelength dependence of the peak gain can be compared directly with the computed curve. Referring to the *calculated* curve, the maximum gain exceeds 2 percent cm^{-1} over a ~40 nm spectral range and it exceeds 1 percent cm^{-1} over a ~70 nm range. Indeed, this laser has been tuned with efficient (1-1.5 percent) energy extraction between 470 and 500 nm with nearly constant output [2].

Although the agreement between the computed curve and the data points shown is satisfactory, the difference above ~490 nm is obviously larger than at other wavelengths and appears to be systematic. The difference may

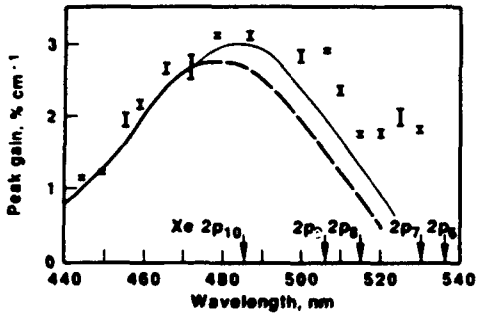

Fig. 12. Calculated wavelength dependence of the maximum XeF($C \rightarrow A$) net gain (occurring at -30 ns, Figs. 9 and 10). Also shown for comparative purposes are experimental points obtained under generally similar conditions for wavelengths at which discrete absorption does not occur [53]. The upper curve ($\lambda \leq 470$ nm) was obtained by subtracting the effect of absorption due to the Xe ($2P_6 \rightarrow 2P_{10}$) states, having wavelength thresholds as indicated, see Section III-B.

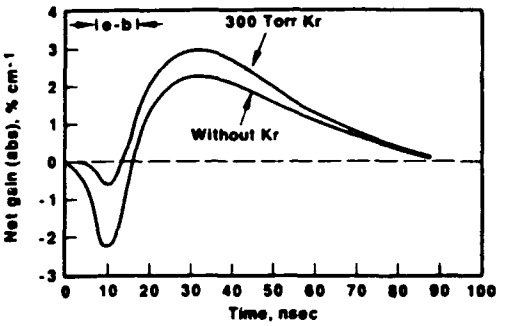

Fig. 13. Comparison of the temporal gain profiles (480 nm) for the mixture of Fig. 6, and the same mixture without Kr.

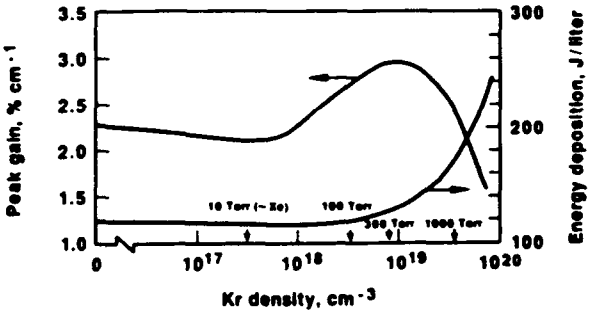

Fig. 14. Effect of Kr variation on the maximum gain (480 nm), (occurring at -30 ns, Fig. 13), and on the volumetric e beam energy deposition.

be real and due, at least in part, to the fact that the Xe($2p_{10}$) level, the lowest energy level of Xe($6p$) manifold, requires a photon energy of at least 2.5 eV (i.e., $\lambda \leq 490$ nm) for photoionization. The $2p_{10}$ level is the one in quasiequilibrium with Xe($1s_2$), the combination likely to be the dominant contributor to our Xe**, particularly after termination of the e-beam excitation pulse. Thus, our procedure for modeling Xe** is most likely semiquantitative at best as regards calculation of absorption for wavelengths ≥ 500 nm. In any case, the measured gain for wavelength >500 nm suggests an even larger tuning range than the computed gain curve.

C. Effect of Kr on Absorption

As reported previously [5] and discussed herein, the presence of Kr in the XeF($C \rightarrow A$) laser mixture affects practically all aspects of gas kinetics. However, the most striking effect, and the first observed [31], is a significant reduction in the transient absorption during the e-beam excitation pulse when Kr is added to the gas mixture. Presented in Fig. 13 is a comparison of the temporal gain profile discussed previously (Fig. 9) with a gain profile computed for exactly the same conditions, but with no Kr in the mixture. The much larger initial absorption when Kr is omitted is in very good agreement with experimental observations [53]. Analysis shows that the reduced absorption is due almost entirely to a reduced Ar_3^+ concentration, which is approximately an order-of-magnitude lower in the Ar–Kr buffered mixture, a reflection of the strong $Ar_2^+(Ar_3^+) \rightarrow Kr^+$ charge exchange reactions (Table I). Fig. 5 shows that the cross section for Ar_3^+ photoabsorption is exceptionally high for blue-green photons. Thus, the reduction in the population of Ar_2^+ and Ar_3^+ as a consequence of charge exchange with Kr results in a very significant decrease in the *initial* absorption when Kr is combined with Ar to form the buffer.

1) Kr variation: Fig. 14 illustrates the effect of Kr variation on the peak XeF($C \rightarrow A$) gain, which occurs at the -30 ns point in Fig. 13. As Kr is added, initially there is a slight decrease in the $C \rightarrow A$ peak gain as the Kr and Xe compete. In fact, a slight gain minimum is observed when the Kr and Xe pressures are approximately equal. This is consistent with experimental observations which show that for Kr ~ Xe, the $C \rightarrow A$ laser output actually decreases [53]. However, as the Kr pressure is increased further (Kr >> Xe), the $C \rightarrow A$ gain rises dramatically, reaching a broad maximum at a Kr pressure of ~ 300 Torr, a value shown by experiment to be optimum for the conditions of Fig. 9 [1], [2]. For Kr pressures above ~ 500 Torr the $C \rightarrow A$ gain decreases rapidly, even though the energy deposition is increasing, also in accord with experimental observations [1].

Throughout a four order-of-magnitude variation in Kr pressure (Fig. 14), the computed XeF(C) population changes by no more than ± 20 percent, even though Kr significantly effects all aspects of the kinetics. This rather remarkable result is entirely consistent with the experimental observation that the time integrated $C \rightarrow A$ fluorescence is essentially independent of Kr pressure [5]. In fact, the undulating nature of the $C \rightarrow A$ gain for the conditions of Fig. 14 is due almost entirely to the effect of Kr on transient absorption. In the 30–300 Torr range of Kr pressure the concentrations of transient absorbers (Ar_3^+ in particular) decrease. Above 300 Torr, absorption due to Kr** and Xe** increases reflecting in part the increased energy deposition level. In that connection, it should be pointed out that for every value of total pressure and e-beam temporal duration there is an optimum combination of mixture constituents and e-beam pumping intensity. However, experimental constraints and/or procedures usually limit the range of accessible parameter space. Thus, the presentation of Fig. 14 reflects the usual experimental procedure [1] for which the total pressure,

minority mixture fractions and *e*-beam parameters are fixed while the Kr pressure is varied.

D. XeF(B, C) Formation and Loss

Figs. 15 and 16 present the temporal variation of the *primary* individual contributions to XeF(B, C) formation and loss for the conditions of Figs. 6–14.

1) XeF Formation: As regards XeF formation, the indicated ion–ion recombination and harpooning reactions are more important at lower Kr concentrations. However, the increasing importance of the $Kr_2F + Xe \rightarrow XeF$ displacement reaction as the Kr pressure is increased compensates for the decreasing importance of those reactions, with the result that the XeF formation rate is sensibly constant over a very large range of Kr pressure. As mentioned previously, we infer a value of $\sim 4.5 \times 10^{-10}$ s^{-1} cm^3 for the indicated Kr_2F-Xe displacement reaction. Displacement reactions involving ArF and/or KrF are not important sources of XeF because these species are rapidly converted to rare gas halide triatomics at a pressure of six atm and, therefore, are present in relatively low concentrations (Fig. 7).

For the conditions of Fig. 15 the calculated XeF formation efficiency is ~6 percent, a value which is affected by the ~2.5 eV photon energy of the C → A transition. Numerical experimentation indicates that the XeF(C) formation efficiency may be as high as ~10 percent for certain combinations of pressure, mixture, and *e*-beam pump intensity/duration.

2) XeF Quenching: Quenching of XeF is dominated by three-body processes, reflecting the 6 atm Ar buffer pressure, and by two-body collisions with Xe (Fig. 16). For the present conditions, Ar, Kr, and Xe contribute approximately equally to three-body quenching of XeF. Our modeling shows that the peak gain increases slightly as the pressure is reduced below 6 atm, *provided* that the electron-beam current density is increased to maintain the pump energy density level constant. This trend is due to the reduced importance of three-body quenching of XeF (Fig. 16) as the pressure is reduced. Table IV shows the dominant XeF quenching processes considered in our model along with the corresponding rate coefficients.

3) Electron Quenching: Fig. 16 shows that the effect of electron quenching is significant. Rate coefficients for electron quenching of rare gas halide diatomics and triatomics are highly uncertain. Such data are never determined directly, and their inference requires accurate knowledge of the halogen concentration, the electron density, the average electron energy, and possibly even specific details of the electron energy distribution [35]. The two latter properties are highly dependent on gas pressure and on the specific gas mixture. Thus, it is not surprising that there is almost an order-of-magnitude variation in reported values of electron quenching coefficients for rare gas halides. In this paper, we have used values of 1.4×10^{-7} s^{-1} cm^3 and 4.0×10^{-8} s^{-1} cm^3 for electron quenching of the B and C states of XeF. These values are twice those computed by Hazi, Rescigno, and Orel [54] for *superelastic* deexcitation of XeF by electrons, and are

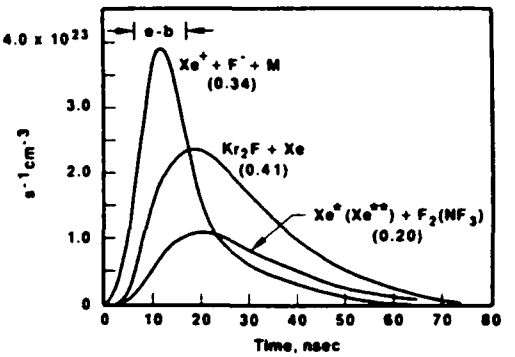

Fig. 15. Temporal variations of the primary XeF(B, C) formation processes for the conditions of Figs. 6–13. The fractional contribution of each process on a time integrated basis is also indicated.

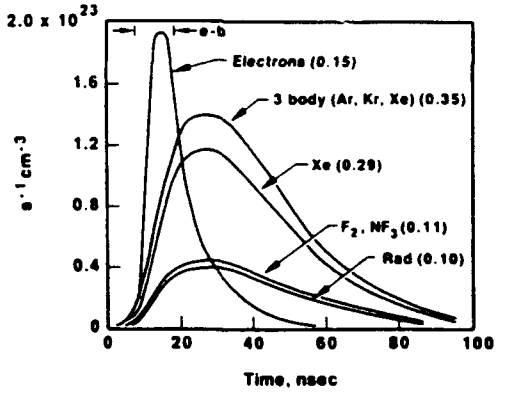

Fig. 16. Temporal variations of the primary XeF(B, C) loss processes for the conditions of Figs. 6-13. The fractional contribution of each process on a time integrated basis is also indicated.

TABLE IV
XeF Loss Processes

Reaction	Rate Coefficient[a]	Reference
XeF + 2Ar → products	7×10^{-34}	See Ref. 11
XeF + Xe + Ar → products	4×10^{-31}	12
XeF + Kr + Ar → products	$\sim 1.0 \times 10^{-32}$	this work
XeF + Xe → products	1.2×10^{-10}	12
XeF + F_2 → products	2.0×10^{-10}	11
XeF + NF_3 → products	2.0×10^{-11}	11
XeF(B) → XeF(X) + hν	7.7×10^{7}	11, 49
XeF(C) → XeF(A) + hν	1.0×10^{7}	11, 49
XeF(B) + e → products	1.4×10^{-7}	see text
XeF(C) + e → products	4.0×10^{-8}	see text

[a] The units for two- and three-body rate coefficients are s^{-1} cm^3 and s^{-1} cm^6, respectively, and for radiative transitions the units are s^{-1}.

in reasonable agreement with values of *total* quenching coefficients reported by others. Numerical experimentation shows that an increase in the B and C state electron quenching coefficients by as much as a factor of three over the values used reduces the peak XeF(C) population by only ~20 present. Nonetheless, electron quenching has a significant influence on the variation of the peak gain as the electron beam energy deposition (pump power) is increased. For energy deposition values up to approximately 50 J/l (5 MWcm^{-3} for our 10 ns excitation pulse) the peak gain is nearly proportional to pump energy/

power. However, as the electron beam pumping level is increased above 50 J/l, the increasing electron density and the resulting XeF(B, C) quenching by electrons limits the increase in the XeF(C) population. Indeed, our modeling shows that for the conditions of present interest the peak gain saturates for pumping levels of $\lesssim 100$ J/l (10 MWcm^{-3}). The computed variation of maximum XeF($C \rightarrow A$) gain with electron beam pump energy is found to be in good agreement with experimental observations [2].

4) Rate Coefficient Sensitivity: Figs. 15 and 16 show that no single process dominates either XeF formation or loss. For this reason our numerical experimentation with the various rate coefficients corresponding to the processes indicated in the figures shows that the maximum likely uncertainty in the computed XeF(C) population near the peak of the gain profile is ± 20 percent. Since the absorption is relatively small at the time the XeF(C) population reaches its maximum value (Fig. 10), the uncertainty in the computed net gain maximum is also estimated to be on the order of ± 20 percent.

E. Alternate Excitation Conditions

All of our work to date has focused on high current density e-beam excitation of short temporal duration. Such conditions result in the highest net gain on the XeF($C \rightarrow A$) transition, a particularly important consideration when efficient, broad-band, continuous tuning [2] is the primary objective. However, other excitation techniques such as *soft e* beam pumping for times ≥ 100 ns and discharge excitation have considerable potential.

1) Long Pulse E-Beam Excitation: Shortly after laser oscillation on the XeF($C \rightarrow A$) transition was first demonstrated, Campbell, Fisher, and Center [55] achieved laser oscillation, albeit at very low efficiency, using a low current density ($\lesssim 10$ A/cm^2) e beam having a duration of 1 μs. Either Ar at a pressure of two atm or Kr at 1 atm was used as the buffer gas, and both F_2 and NF_3 (individually) were used as a source of fluorine. Although laser oscillation was demonstrated, the measured net gain at 488 nm was very low, <0.1 percent cm^{-1}, resulting in an extraction energy density on the order of one mJ/l when a stable resonator was utilized.

We have computed the net gain at 480 nm for the *same* conditions used by Campbell *et al.* and find it to be ~ 0.1 percent cm^{-1}. More important, however, the computed magnitudes of the contributions to the net gain of both XeF(C) and transient absorption are both significantly larger than the *net* gain itself. Thus, relatively small changes in either the C state population or the absorption level will have a disproportionately large effect on the net gain. Accordingly, we recomputed the net gain at 480 nm for e-beam conditions generally similar to those of [55], i.e., two atm Ar buffer pressure, but with the Kr, Xe, NF_3, and F_2 pressures of Figs. 6–13. For these conditions, corresponding to an electron beam energy deposition of ~ 300 J/l (~ 300 kW $\cdot$ cm^{-3}) in 1 μs, the computed net gain at 480 nm increased from ~ 0.1 percent cm^{-1} to ~ 0.5 percent cm^{-1}. Although no attempt was made to optimize the mixture or the e-beam pumping level, it is clear that a net gain on the order of 0.5 percent cm^{-1} should be consistent with reasonably efficient energy extraction using a microsecond excitation pulse. Indeed, XeF($C \rightarrow A$) laser output energy density and intrinsic efficiency values of ~ 1 J/l and ~ 1 percent have been reported recently using a similar Ar, Kr, Xe, F_2, NF_3 mixture excited by a ~ 0.7 μs electron beam [56]. It should be pointed out, however, that the gain in the wings of the profile and at wavelengths for which discrete absorption occurs [2] will be considerably less than 0.5 percent cm^{-1}, a factor that is significant as regards wavelength tuning off the gain maximum.

2) Discharge Excitation: For some applications discharge excitation of the XeF($C \rightarrow A$) laser will have advantages over e-beam excitation. In the past discharge excitation of the $C \rightarrow A$ has suffered from the same problem as long pulse e-beam excitation, i.e., low gain and therefore unacceptably low extraction energy/efficiency [57], [58]. Injection control [59] improved the situation, but use of a stable optical cavity severely limited the portion of the active volume from which energy could be extracted. Very recently [60], injection control of a discharge excited $C \rightarrow A$ laser was accomplished injecting through a small hole in the large mirror of an unstable cavity. The latter served as a beam expending telescope [2] permitting use of the entire active volume. With this arrangement extraction energy density and intrinsic efficiency values of approximately 0.1 J/l and 0.1 percent, respectively, have been obtained, representing a significant improvement over prior results. In that work, the gas mixture found to be compatible with stable discharge operation was He buffered, and was essentially the same as that used for XeF($B \rightarrow X$) laser oscillation. Although we have not modeled the discharge excited $C \rightarrow A$ laser, it seems clear that the key issue is attainment of stable discharges in mixtures compatible with efficient XeF(C) formation and low transient absorption.

IV. Summary

Through kinetics optimization using multicomponent gas mixtures [1], [5], [34], the XeF($C \rightarrow A$) laser has emerged as one that is capable of extraction energy density and efficiency values comparable to those of the better developed rare gas halide $B \rightarrow X$ lasers when excited under generally similar conditions. Moreover, the $C \rightarrow A$ laser is the only excimer laser capable of wide-band, continuous wavelength tuning. Indeed, efficient (~ 1 percent) tuning over a 30 nm bandwidth has already been demonstrated [2] using "short pulse" e-beam excitation as described herein, and an efficient tuning range approaching 100 nm is a distinct possibility.

In this paper, we have analyzed the fundamental processes affecting formation and loss of both the XeF excimer and the primary transient species that absorb in the blue-green spectral region. Agreement and consistency with experimental observations [1], [2] is generally good for the high current density, short temporal duration

e-beam conditions examined. Additionally, low current density, "soft" *e*-beam pumping for a duration on the order of 1.0 μs appears promising [56]. Efficient energy extraction using discharge excitation is also on the horizon [60] if laser medium and discharge stability compatibility can be achieved.

Although the results of the present analysis/modeling indicate that XeF($C \rightarrow A$) laser kinetics are reasonably well understood, our investigation also reveals areas for which the fundamental data base is weak or incomplete. Examples of processes for which the data base of rate coefficients and reaction products could be significantly improved are as follows:

1) two- and three-body charge exchange involving Ar, Kr, and Xe homonuclear and heteronuclear molecular ions, particularly the latter;

2) formation and destruction of weakly bound (<0.5 eV) heteronuclear rare gas dimer ions and excited species;

3) halogen reactive quenching of higher excited states of the rare gases;

4) reactive quenching of rare gas excited states by halogen dissociation fragments;

5) rare gas diplacement reactions for rare gas halide diatomic and triatomic species;

6) electron quenching of rare gas halide diatomic and triatomic species.

Strengthening and expansion of the database for reactions of the type indicated are important for applications involving all UV rare gas-halide lasers, the XeF($C \rightarrow A$) laser, and other lasers such as the atomic xenon laser [61], particulary as attempts are made to scale laser systems to large sizes.

Acknowledgment

It is a pleasure to acknowledge numerous helpful and informative conversations with our colleagues and collaborators at Rice University, particularly F. K. Tittel, R. A. Sauerbrey, W. L. Wilson, Jr., and N. Hamada. The insightful comments of D. W. Setser of Kanasa State University concerning chemical reaction kinetics are very much appreciated.

References

[1] W. L. Nighan, F. K. Tittel, W. L. Wilson, Jr., N. Nishida, Y. Zhu, and R. Sauerbrey, "Synthesis of rare-gas halide mixtures resulting in efficient XeF(C → A) laser oscillation," *Appl. Phys. Lett.*, vol. 45, pp. 947-949, 1984.

[2] N. Hamada, R. Sauerbrey, W. L. Wilson, Jr., F. K. Tittel, and W. L. Nighan, "Performance characteristics of an injection-controlled electron-beam pumped XeF(C → A) laser system," *IEEE J. Quantum Electron.*, vol. 24, pp. 1571-1578, 1988.

[3] A. E. Mandl and H. A. Hyman, "XeF laser performance for F_2 and NF_3 fuels," *IEEE J. Quantum Electron.*, vol. QE-22, pp. 349-359, 1986.

[4] A. E. Mandl and L. Litzenberger, "XeF laser at high electron beam pump rate," *Appl. Phys. Lett.*, vol. 51, pp. 955-957, 1987.

[5] W. L. Nighan, R. A. Sauerbrey, Y. Zhu, F. K. Tittel, and W. L. Wilson, Jr., "Kinetically tailored properties of electron-beam excited XeF(C → A) and XeF(B → X) laser media using an Ar-Kr buffer mixture," *IEEE J. Quantum Electron.*, vol. QE-23, pp. 253-261, 1987.

[6] M. R. Flannery and T. P. Tang, "Ionic recombination of rare gas atomic ions X^+ and F^- in a dense gas X," *Appl. Phys. Lett.*, vol. 32, pp. 327-329, 1978.

[7] ——, "Ionic recombination of rare gas molecular ions X_2^+ with F^- in a dense gas X," *Appl. Phys. Lett.*, vol. 32, pp. 356-357, 1978.

[8] M. R. Flannery, "Ion-ion recombination in high pressure plasmas," in *Applied Atomic Collision Physics, Volume 3: Gas Lasers*, H. S. W. Massey, E. W. McDaniel and B. Bederson, Eds. New York: Academic, 1982, ch. 5.

[9] J. E. Velazco, J. H. Kolts, and D. W. Setser, "Rate constants and quenching mechanisms for the metastable states of argon, krypton and xenon," *J. Chem. Phys.*, vol. 69, pp. 4357-4373, 1978.

[10] ——, "Quenching rate constants for metastable argon, krypton and xenon atoms by fluorine containing molecules and branching ratios for XeF* and KrF* formation," *J. Chem. Phys.*, vol. 65, pp. 3468-3480, 1976.

[11] H. C. Brashears and D. W. Setser, "Transfer and quenching rate constants for XeF(B) and XeF(C) states in low vibrational levels," *J. Chem. Phys.*, vol. 76, pp. 4932-4946, 1982.

[12] R. Sauerbrey, W. Walter, F. K. Tittel, and W. L. Wilson, Jr., "Kinetic processes of electron beam generated XeF* and Xe_2F^* excimers," *J. Chem. Phys.*, vol. 76, pp. 735-747, 1983.

[13] D. K. Bohme, N. G. Adams, M. Mosesman, D. B. Dunkin, and E. E. Ferguson, "Flowing afterglow studies of the reactions of the rare-gas molecular ions He_2^+, Ne_2^+ and Ar_2^+ with molecules and rare gas atoms," *J. Chem. Phys.*, vol.52, pp. 5094-5100, 1970.

[14] R. J. Shul, R. Passarella, B. L. Upschulte, R. G. Keesee, and A. W. Castleman, Jr., "Thermal energy reactions involving Ar^+ monomer and dimer ions with N_2, H_2, Xe and Kr," *J. Chem. Phys.*, vol. 86, pp. 4446-4451, 1987.

[15] C. B. Collins and F. W. Lee, "Measurement of the rate coefficients for the biomolecular and trimolecular ion-molecule reactrons of Ar_2^+ with selected atomic and molecular species," *J. Chem. Phys.*, vol. 71, pp. 184-191, 1979.

[16] C. B. Collins, Z. Chen, V. T. Gylys, H. R. Jahani, J. M. Pouvesle, and J. Stevefelt, "The importance of three-body processes to reaction kinetics at atmospheric pressures—I: Archetype reactions of the species with N_2," *IEEE J. Quantum Electron.*, vol. QE-22, pp. 38-46, 1986.

[17] H. R. Jahani, V. T. Gylys, C. B. Collins, J. M. Pouvesle, and J. Stevefelt, "The importance of three-body processes to reaction kinetics at atmospheric pressures III: Reactions of He_2^+ with selected atomic and molecular reactents," *IEEE J. Quantum Electron.*, vol. 24, pp. 568-572, 1988.

[18] W. J. Wiegand, Jr., "High pressure ion kinetics," in *Applied Atomic Collision Physics; Volume 3: Gas Lasers*, H. S. W. Massey, E. W. McDaniel, and B. Bederson, Eds. New York: Academic, 1982, ch. 3 and references cited therein.

[19] P. Millet, A. Birot, H. Brunet, H. Dijols, J. Galy, and Y. Salamero, "Spectroscopic and kinetic analysis of the VUV emissions of argon and argon-xenon mixtures: I. Study of pure argon," *J. Phys. B: At. Mol. Phys.*, vol. 15, pp. 2935-2944, 1982.

[20] H. Brunet, A. Birot, H. Dijols, J. Galy, P. Millet, and Y. Salamero, "Spectroscopic and kinetic analysis of the VUV emissions of argon and argon-xenon mixtures: II. Energy transfer in Ar-Xe mixtures," *J. Phys. B: At. Mol. Phys.*, vol. 15, pp. 2945-2967, 1982.

[21] Y. Salamero, A. Birot, H. Brunet, H. Dijols, J. Galy, P. Millet, and J. P. Montagne, "Energy transfer kinetics of the VUV emissions for Kr-Xe mixtures," *J. Chem. Phys.*, vol. 74, pp. 288-296, 1981.

[22] P. J. Chantry, "Negative ion formation in gas lasers," in *Applied Atomic Collision Physics; Volume 3: Gas Lasers*, H. S. W. Massey, E. W. McDaniel and B. Bederson, Eds. New York: Academic, 1982, ch. 2.

[23] Y-J Shiu and M. A. Biondi, "Dissociative recombination in argon: Dependence of the total rate coefficient and excited state production on electron temperature," *Phys. Rev. A.*, vol. 17, pp. 868-872, 1978.

[24] Y-J Shiu, M. A. Biondi, and D. P. Siples, "Dissociative recombination in Xenon: Variation of the total rate coefficient and excited state production with electron temperature," *Phys. Rev. A*, vol. 15, pp. 494-498, 1977.

[25] Y-J Shiu and M. A. Biondi, "Dissociative recombination in Krypton: Dependence of the total rate coefficient and excited state production on electron temperature," *Phys. Rev. A.*, vol. 16, pp. 1817-1820, 1977.

[26] W. L. Nighan, "Plasma processes in electron-beam controlled rare gas halide lasers," *IEEE J. Quantum Electron.*, vol. QE-14, pp. 714-726, 1978.

[27] A. Mandl, D. Klimek, and J. H. Parks, "KrF laser kinetics studies," *J. Appl. Phys.*, vol. 55, pp. 3940-3949, 1984.
[28] T. T. Yang, J. A. Blauer, C. E. Turner, Jr., and D. A. Copeland, "Multiline model for the e-beam pumped XeF(B → X) laser," *AIAA J.*, vol. 23, pp. 741-748, 1985.
[29] F. Kannari, M. Obara, and T. Fujioka, "An advanced kinetic model of electron-beam-excited KrF lasers including the vibrational relaxation in KrF(B) and collisional mixing of KrF(B, C)," *J. Appl. Phys.*, vol. 57, pp. 4309-4322, 1985.
[30] H. H. Michels and J. A. Montgomery, "Electronic structure and stability of the Ar_3^+ cluster ion," *Chem. Phys. Lett.*, to be published.
[31] Y. Nachshon, F. K. Tittel, W. L. Wilson, Jr., and W. L. Nighan, "Efficient XeF(C → A) laser oscillation using electron beam excitation," *J. Appl. Phys.*, vol. 56, pp. 36-48, 1984.
[32] D. L. Turner and D. C. Conway, "Study of the $2Ar + Ar_2^+ = Ar + Ar_3^+$ reaction," *J. Chem. Phys.*, vol. 71, pp. 1899-1901, 1979.
[33] J. A. MacDonald, M. A. Biondi, and R. Johnson, "Electron temperature dependence of the dissociative recombination of Ne_2^+ ions with electrons," *J. Phys. B*, vol. 16, pp. 4273-4280, 1983.
[34] W. L. Nighan, Y. Nachshon, F. K. Tittel, and W. L. Wilson, Jr., "Optimization of electrically excited XeF(C → A) laser performance," *Appl. Phys. Lett.*, vol. 42, pp. 1006-1008, 1983.
[35] Z. Rosenberg, M. Lando, and M. Rokni, "Direct measurement of the electron density in electron-beam-irradiated Ar-F_2 gas mixtures by time resolved interferometry," *Phys. Rev. A.*, vol. 35, pp. 4151-4159, 1987.
[36] C. J. Elliott and A. E. Greene, "Electron energy distributions in e-beam generated Xe and Ar plasmas," *J. Appl. Phys.*, vol. 47, pp. 2946-2952, 1976.
[37] J. K. Ku and D. W. Setser, "Significant enhancement of XeCl(B, C) and XeF(B, C) formation rate constants in reactions of $Xe(5p^56p)$ atoms with halogen donors," *Appl. Phys. Lett.*, vol. 48, pp. 689-691, 1986.
[38] C. Duzy and H. A. Hyman, "Photoionization of excited rare gas atoms," *Phys. Rev. A*, vol. 22, pp. 1878-1883, 1980.
[39] R. S. F. Chang and D. W. Setser, "Radiative lifetimes and two-body deactivation rate constants for $Ar(3p^5,4p)$ and $Ar(3p^5,4p')$ states," *J. Chem. Phys.*, vol. 69, pp. 3885-3897, 1978.
[40] R. S. F. Chang, H. Horiguchi, and D. W. Setser, "Radiative lifetimes and two-body collisional deactivation rate constants in argon for $Kr(4p^55p)$ and $Kr(4p^55p')$ states," *J. Chem. Phys.*, vol. 73, pp. 778-780, 1980.
[41] G. Inoue, J. K. Ku, and D. W. Setser, "Laser induced fluorescence study of $Xe(5p^56p, 5p^56p', 5p^57p$ and $5p^56d)$ states in Ne and Ar: Radiative lifetimes and collisional deactivation rate constants," *J. Chem. Phys.*, vol. 81, pp. 5760-5774, 1984.
[42] J. K. Ku and D. W. Setser, "Collisional deactivation of $Xe(5p^56p)$ states in Xe and Ar," *J. Chem. Phys.* vol. 84, pp. 4304-4316, 1986.
[43] J. Xu and D. W. Setser, "Collisional deactivation studies of the Xe(6p) states in Kr and Ar," *J. Chem. Phys.*, to be published.
[44] D. B. Geohegan and J. G. Eden, "Absorption spectrum of $Kr_2F(4^2\Gamma)$ in the near ultraviolet and visible ($335 \leq \lambda \leq 600$ nm): Comparison with Kr_2^+ ($1(1/2)_u$) measurements," *J. Chem. Phys.*, vol. 89, pp. 3410-3427, 1988.
[45] H. H. Michels, R. H. Hobbs, and L. A. Wright, "Electronic structure of the noble gas dimer ions. II. Theoretical absorption spectrum for the $A^2\Sigma_{2u}^+ \rightarrow D^2\Sigma_{1/2g}^+$ system," *J. Chem. Phys.*, vol. 71, pp. 5053-5062, 1979.
[46] C. F. Bender and N. W. Winter, "Theoretical absorption spectra of $ArKr^+$," *Appl. Phys. Lett.*, vol. 33, pp. 24-31, 1978.
[47] N. E. Levinger, D. Ray, K. K. Murray, A. S. Mullin, C. P. Schulz, and W. C. Lineberger, "The visible photoabsorption spectrum of Ar_3^+," *J. Chem. Phys.*, vol. 89, pp. 71-74, 1988.
[48] A. Mandl, "Electron photodetachment cross section of the negative ion of fluorine," *Phys. Rev. A*, vol. 3, pp. 251-255, 1971.
[49] W. K. Bischel, D. J. Eckstrom, H. C. Walker, Jr., and R. A. Tilton, "Photolytically pumped XeF(C → A) laser studies," *J. Appl. Phys.*, vol. 52, pp. 4429-4434, 1981.
[50] W. R. Wadt and P. J. Hay, "Electronic States of Ar_2F and Kr_2F," *J. Chem. Phys.*, vol. 68, pp. 3850-3863, 1978.
[51] Y. Nachshon and F. K. Tittel, "A new blue-green XeF(C → A) excimer laser amplifier concept," *Appl. Phys.: B*, vol. 25, pp. 227-231, 1984.
[52] F. K. Tittel, M. Smayling, W. L. Wilson, Jr., and G. Marowsky, "Blue laser action by the rare gas halide trimer Kr_2F," *Appl. Phys. Lett.*, vol. 37, pp. 862-864, 1980.
[53] R. A. Sauerbrey, private communication.
[54] A. V. Hazi, T. N. Rescigno and A. E. Orel, "Theoretical study of the deexcitation of KrF and XeF excimers by low energy electrons," *Appl. Phys. Lett.*, vol. 35, pp. 477-479, 1979.
[55] J. D. Campbell, C. H. Fisher, and R. E. Center, "Observations of gain and laser oscillation in the blue-green during direct pumping of XeF by microsecond electron beam pulses," *Appl. Phys. Lett.*, vol. 37, pp. 349-350, 1980.
[56] A. E. Mandl and L. N. Litzenberger, "Efficient, long pulse XeF(C → A) laser at moderate electron-beam pump rates," *Appl. Phys. Lett.*, to be published.
[57] R. Burnham, "A discharge pumped laser on the C → A transition of XeF," *Appl. Phys. Lett.*, vol. 35, pp. 48-49, 1979.
[58] C. H. Fisher, R. E. Center, G. J. Mullaney, and J. P. McDaniel, "A 490 nm XeF electric discharge laser," *Appl. Phys. Lett.*, vol. 35, pp. 26-28, 1979.
[59] ——, "Multipass amplification and tuning of the blue-green XeF(C → A) laser," *Appl. Phys. Lett.*, vol. 35, pp. 901-903, 1979.
[60] H. Voges and G. Marowsky, "Injection control of a multipass amplification of a discharge excited XeF(C → A) laser," *IEEE J. Quantum Electron.*, vol. 24, pp. 827-832, 1988
[61] N. G. Basov, V. V. Baranov, A. Y. Chugunov, V. A. Danilychev, A. Y. Dudin, I. V. Kholin, N. N. Ustinovskii, and D. A. Zayarnyi," 60 J quasistationary electoionization laser on Xe atomic metastables," *IEEE J. Quantum Electron.*, vol. QE-21, pp. 1756-1760, 1985.

William L. Nighan (SM'85) was born in Philadelphia, PA, in 1938. He received the B.S. degree in engineering from the University of Dayton, Dayton, OH, in 1961 and the M.S. degree in engineering science from Northwestern University, Evanston, IL, in 1962.

Since 1962 he has been with United Technologies Research Center, East Hartford, CT where he is Manager, Applied Physics in the Electronics and Photonics Technologies Department. His primary research activities have been in areas of gas discharge physics, electric lasers, plasma displays, and applied atomic, molecular and chemical physics.

Mr. Nighan is a member of Sigma Xi, Tau Beta Pi, and the American Physical Society.

Michael C. Fowler was born in New York City in 1941. He received the B.S. degree in chemistry from Yale University, New Haven, CT, in 1963 and the Ph.D. degree in physical chemistry from the Massachusetts Institute of Technology, Cambridge, MA, in 1967.

Since 1969, he has been at the United Technologies Research Center where he is now a Senior Research Scientist in the Combustion and Environmental Science group. His research activities have included both experimental and analytical work in the fields of plasma physics, electric discharge laser physics, optics and problems associated with high power laser propagation and chemical methods of hydrogen storage.

Dr. Fowler is a member of Sigma Xi, Alpha Chi Sigma, the American Physical Society, the Optical Society of America, and the Society of Photo-Optical Instrumentation Engineers.